

Faltering Steps Into the Galaxy: The Boundary Regions of the Heliosphere

G.P. Zank

Center for Space Plasma and Aeronomic Research (CSPAR), Department of Space Science,
University of Alabama in Huntsville, Huntsville, Alabama 35805; email: garyp.zank@gmail.com

Annu. Rev. Astron. Astrophys. 2015. 53:449–500

First published online as a Review in Advance on
June 24, 2015

The *Annual Review of Astronomy and Astrophysics* is
online at astro.annualreviews.org

This article's doi:
[10.1146/annurev-astro-082214-122254](https://doi.org/10.1146/annurev-astro-082214-122254)

Copyright © 2015 by Annual Reviews.
All rights reserved

Keywords

solar wind, stellar winds, interstellar medium, plasma, neutral gas, pickup ions, cosmic rays, magnetic fields, *Voyager* Interstellar Mission, IBEX

Abstract

The interaction of the heliosphere with the local interstellar medium (LISM) results in a complicated series of boundary regions. The *Voyager 1* and 2 spacecraft are exploring these distant boundaries in situ, as is the Interstellar Boundary Explorer from 1 AU, which measures energetic neutral atoms created in the distant reaches of the heliosphere and LISM. Lyman- α absorption and backscatter measurements also probe the structure and physics of the interface of the heliosphere and LISM. We survey the suite of observations, the underlying theory, and the resulting models that describe the boundary regions of the solar wind and LISM.

1. INTRODUCTION

At a press conference held in Washington, DC, on 12 September 2013, the Principal Investigator of the *Voyager* Interstellar Mission, Dr. E.C. Stone, announced that the *Voyager 1* (V1) spacecraft had crossed the heliopause (HP) a year earlier in August 2012, entering the very local interstellar medium (VLISM). It is now widely, although not universally, accepted that V1 is in interstellar space (Burlaga et al. 2013b, Gurnett et al. 2013, Krimigis et al. 2013, Stone et al. 2013), offering an unprecedented opportunity to study in situ basic plasma physical processes of the interstellar medium (ISM). The presence of the V1 spacecraft in interstellar space presents an event of enormous historical import as humankind breaks out of its solar neighborhood, beginning another epoch of extraordinary discovery science. This review discusses the observations and theory of the interaction between the solar wind (SW) and the local interstellar medium (LISM) that led to the eventual crossing of the HP by V1 and, some years from now, *Voyager 2* (V2).

Many of the ideas discussed below find natural extension to the general interaction of stellar winds with the ISM. An “asterosphere” may be defined as the gas or plasma structural adaptation of a stellar wind to its local ISM. As described below, the mediation of the stellar wind by the ISM and vice versa will shape the boundary regions and physics. Almost every category of stellar object can generate an asterosphere, and the possible structures can be highly varied (see Cox et al. 2012). There are numerous techniques for investigating asterospheres across multiple wavelengths. The physics learned from the heliospherical example will be useful to the new field of asterospheric astrophysics.

1.1. Brief Overview

In the past two decades, great progress has been made in our understanding of the physical processes thought to describe the outer heliosphere. Fundamental to these advances has been the recognition that the ISM and heliosphere are coupled intimately through charge exchange of neutral hydrogen (H) and protons and that the physics of the outer heliosphere and VLISM cannot be understood independently of each other. As a result, this field truly lies at the crossroads of space physics and astrophysics.

The heliosphere is the region of space filled by the expanding solar corona; a region extending >120 AU in the direction of the Sun’s motion through the ISM and perhaps tens of thousands of astronomical units in the opposite or heliotail direction. Neutral interstellar H is the dominant (by mass) constituent of the SW beyond an ionization cavity of $\sim 6\text{--}10$ AU in the upwind direction (the direction antiparallel to the incident interstellar wind) and is coupled weakly to the SW plasma via resonant charge exchange. Charge exchange produces pickup ions (PUIs) that come to dominate the internal energy of the SW. The heliospheric-LISM plasma environment is composed of essentially three thermodynamically distinct regions: Region 3 represents the supersonic SW, with a relatively low temperature, large radial speeds, and low densities, bounded by the heliospheric termination shock (HTS). The outer heliosphere is the region of the SW dynamically influenced by physical processes associated with the LISM. In region 2, the transition of the supersonic SW to a subsonic flow through the HTS creates a region of heated subsonic SW, called the inner heliosheath (IHS). The IHS has much higher temperatures and densities, larger magnetic fields, and lower flow speeds than does the distant supersonic SW. The IHS is bounded by a contact or tangential discontinuity called the HP. The HP is the boundary that separates plasma of solar origin from plasma of interstellar origin (the ISM plasma being region 1). The VLISM possesses low plasma flow speed and temperature, but the density is higher than in regions 1 and 2. A bow shock (BS) may exist ahead of the heliosphere as a result of the relative motion of the Sun and

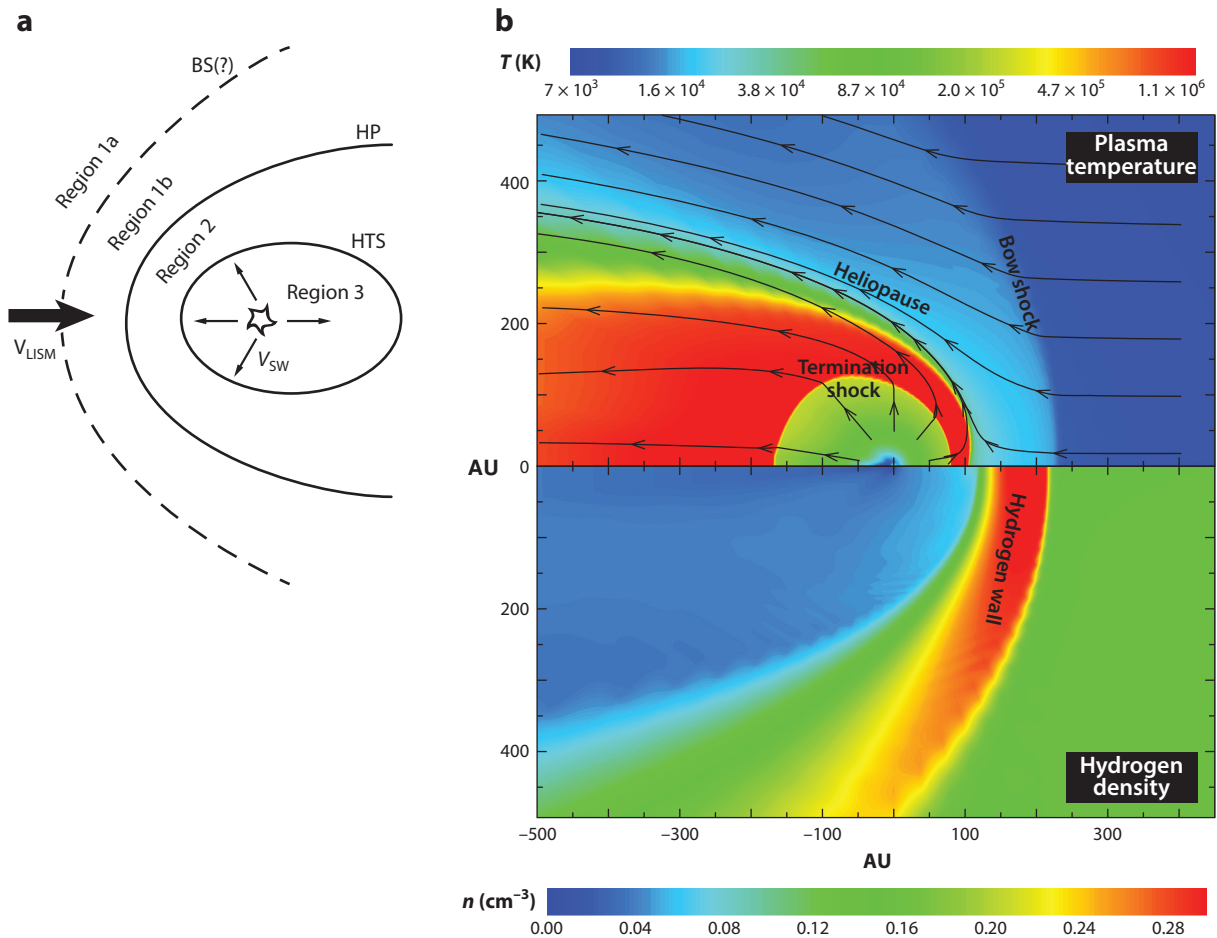


Figure 1

(a) Schematic of the SW-VLISM boundary regions that correspond to distinguishable thermodynamic regions and that act as neutral H sources with clearly distinct characteristics. Adapted from Zank et al. (2009) with permission. (b) A two-dimensional steady-state, two-shock heliospheric interaction with the local ISM: (top plot) the logarithmic temperature distribution of the SW and interstellar plasma, clearly identifying the three distinct regions and the overall topology and boundaries that can exist, and (bottom plot) the density distribution of neutral H. The heliospheric termination shock, heliopause, and bow shock are labeled, and the wall of neutral H is identified. The solid lines of the top plot show the plasma streamlines. Distances are measured in astronomical units. Abbreviations: BS, bow shock; H, hydrogen; HP, heliopause; HTS, heliospheric termination shock; SW, solar wind; VLISM, very local ISM.

ISM. The three regions are illustrated in **Figure 1a**, where region 3 corresponds to the supersonic SW, region 2 to the hot IHS, and the interstellar region is subdivided into region 1b between the HP and a possible BS/wave, sometimes called the outer heliosheath (OHS), and region 1a beyond a BS or bow wave.

Each of the thermodynamically distinct regions is the source of a distinct population of H atoms produced by charge exchange between the ambient plasma and neutrals entering the region (Zank et al. 1996b). These three distinct neutral H populations include the “splash” component produced in the fast or supersonic SW, i.e., fast neutrals that acquire high radially outward speeds ($\sim 400\text{--}750 \text{ km s}^{-1}$), very hot neutrals produced in the IHS with comparatively high speeds ($\sim 100 \text{ km s}^{-1}$), and decelerated heated atoms originating in the OHS. The charge-exchange mean

free path (mfp) in the VLISM (region 1) is approximately ~ 100 AU (assuming a charge-exchange cross section $\sigma_c = 5 \times 10^{-15} \text{ cm}^2$ and a total LISM number density of 0.2 cm^{-3}), in the IHS (region 2) $\sim 2,500$ AU for a number density of 0.005 cm^{-3} , and >200 AU in the supersonic SW beyond 10 AU (region 3). With the exception of the LISM region, the charge-exchange mfps are so large that they exceed the expected scale size of the boundary regions separating the heliosphere and LISM. The interaction of the SW with the LISM therefore requires the modeling of plasmas and nonequilibrated H atom gas. Despite the very large charge-exchange mfps in both the supersonic SW and the boundary regions, the structure of the global heliosphere is determined in large part by the nonequilibrated coupling of neutral interstellar H to supersonic and subsonic SW plasma (Zank 1999a, Zank et al. 2009, McComas et al. 2011). This makes the modeling of the SW interaction with the LISM very challenging. Nonetheless, despite these complications, the basic structure illustrated in **Figure 1a** emerges from simulations that include the basic physics of the plasma-H charge-exchange coupling. An illustrative simulation of a two-dimensional (2D) coupled model of the heliospheric interaction with the LISM is also shown in **Figure 1b**.

The coupling of plasma and neutral H occurs through the creation of PUIs via charge exchange between the charged and neutral gases. Over suitably large distances, the neutral H and protons are fully equilibrated, both possessing the same temperature and velocity. Charge exchange in a fully equilibrated partially ionized plasma has no essential dynamical effect, with charge exchange effectively doing no more than relabeling protons and H atoms. This scenario assumes that the dominant neutral gas component is H atoms; in the LISM, this is a reasonable assumption, although helium (He) atoms are approximately 9% of the neutral gas and the remaining heavy atom neutral gas is approximately 1%. However, in regions 2 and 3, the interstellar H drift speed is different from the plasma flow velocity ($\sim 20 \text{ km s}^{-1}$ for H versus $\sim 100\text{--}750 \text{ km s}^{-1}$ for the plasma). H originating from regions 3 and 2 that splashes back into the LISM also has flow speeds ranging from ~ 100 to 400 km s^{-1} , which is quite different from the $\sim 15\text{--}26 \text{ km s}^{-1}$ speed of the plasma in region 1. Thus, throughout the boundary regions and in the LISM within several hundred astronomical units of the HP, there is a relative drift between the background plasma and some H components. Depending on the specific environment, the neutral gas can be ionized by either solar photons (photoionization) or charged particles (charge-exchange, electron-impact ionization), and the new ions are accelerated almost instantaneously by the motional electric field of the plasma. The PUIs form a ring-beam distribution on the timescale of the inverse gyrofrequency that streams along the magnetic field. Newly created PUIs can therefore drive a host of plasma instabilities (e.g., Lee & Ip 1987; for a summary, see Zank 1999a). PUIs experience scattering and gradual isotropization by either ambient or self-generated low-frequency electromagnetic fluctuations in the plasma. Because the newly born ions are eventually isotropized, their bulk velocity is essentially that of the background plasma, i.e., they advect with the plasma flow and are then “picked up” by the flowing plasma. The isotropized PUIs form a distinct suprathermal population of energetic ions ($\sim 1\text{-keV}$ energies in the supersonic SW) in the plasma whose origin is either the ISM when considering regions 3 and 2 or the heliosphere when considering regions 2 and 1 (e.g., Holzer 1972, Lee & Ip 1987, Williams & Zank 1994; for an extensive review, see Zank 1999a).

Consider now the three specific regions discussed above. PUIs are created in these regions and mediate the plasma properties. Although PUIs mediate each region, the origin of the PUI population in each is different in important ways.

Coulomb collisions are necessary to equilibrate a background thermal plasma, such as the SW, and the PUI protons. For a background Maxwellian plasma comprised of thermal protons (denoted by subscript s) and electrons (subscript e) and PUIs (subscript p), the ordering $v_{ts} \ll v_p < v_{te}$ can be exploited (Zank et al. 2014), where $v_{ts/e}$ denotes the background proton/electron thermal speed, respectively, and v_p is the PUI speed. In the supersonic SW, Isenberg (1986) argued that a

multifluid model is necessary to describe a coupled SW-PUI plasma because neither proton nor electron collisions can equilibrate the PUI-mediated supersonic SW plasma (see Zank et al. 2014).

The IHS is complicated by the microphysics of the HTS. The supersonic SW decelerates upon crossing the quasi-perpendicular HTS. The flow velocity is directed away from the radial direction and is $\sim 100 \text{ km s}^{-1}$. The interplanetary magnetic field (IMF) remains approximately perpendicular to the plasma flow. Per V2 measurements, the downstream SW temperature is in the range of $\sim 120,000\text{--}180,000 \text{ K}$ (Richardson 2008, Richardson et al. 2008), which was much less than predicted by simple MHD models. Instead, the thermal energy in the IHS is dominated by PUIs. There are two primary sources of PUIs in the IHS. The first is interstellar neutrals that drift across the HP and charge exchange with hot SW plasma. These newly created ions are picked up in the IHS plasma in the same way that ions are picked up in the supersonic SW. The characteristic energy for PUIs created in this manner is $\sim 50 \text{ eV}$ or $\sim 6 \times 10^5 \text{ K}$, which is approximately five times hotter than the IHS SW protons. The second primary source is PUIs created in the supersonic SW and then convected across the HTS into the IHS. The PUIs convected to the HTS are either transmitted immediately across the HTS or reflected before transmission (Zank et al. 1996a). Zank et al. (1996a) predicted that PUI reflection is the primary dissipation mechanism at the quasi-perpendicular HTS and the thermal SW protons experience comparatively little heating across the HTS. The transmitted PUIs downstream of the HTS have temperatures $\sim 9.75 \times 10^6 \text{ K}$ ($\sim 0.84 \text{ keV}$), and the reflected protons have a temperature of $\sim 7.7 \times 10^7 \text{ K}$ ($\sim 6.6 \text{ keV}$) (Zank et al. 2010). PUIs that are transmitted, reflected, and injected dominate the thermal energy of the IHS, despite being only $\sim 20\%$ of the thermal subsonic SW number density. The IHS proton distribution function can be approximated by a three- (Burrows et al. 2010, Zank et al. 2010) or four-component distribution function (Zirnstein et al. 2014), with a relatively cool thermal SW Maxwellian distribution and two or three superimposed PUI distributions. In three important papers, Desai et al. (2012, 2014) and Zirnstein et al. (2014) exploited this decomposition of the IHS proton distribution function to great effect in modeling energetic neutral atom (ENA) spectra observed by the IBEX spacecraft at 1 AU. These authors also identified multiple proton distribution functions in the IHS and the VLISM. These multiple proton populations are identified as the various PUI populations described above and the thermal SW proton population (Zank et al. 2010).

Zank et al. (2014) showed that in the IHS neither proton nor electron collisions can equilibrate a PUI-thermal SW plasma in the subsonic SW or IHS on scales smaller than at least 10,000 AU. Thus, for the IHS, a multicomponent plasma description that discriminates between PUIs and the subsonic SW plasma is necessary.

The interstellar plasma upwind of the HP is also mediated by energetic PUIs. Zank et al. (1996b) previously noted that energetic neutral H created via charge exchange in the IHS and fast SW could “splash” back into the ISM where these atoms would experience a secondary charge exchange. The secondary charge exchange of hot and/or fast neutral H with cold ($\sim 6,300 \text{ K}$) (McComas et al. 2012a) LISM protons leads to the creation of a hot or suprathermal PUI population locally in region 1. The heating of the VLISM has been discussed in detail by Zank et al. (2013), who pointed out that this would result in an increase of the sound speed with a concomitant weakening or even elimination of the BS (instead yielding a bow wave). PUIs form a tenuous ($n_p \simeq 5 \times 10^{-5} \text{ cm}^{-3}$) (Zirnstein et al. 2014) suprathermal component in the VLISM. Zank et al. (2014) showed that neither proton nor electron collisions can equilibrate a PUI-thermal plasma in the LISM on scales smaller than at least 75 AU.

Given the above, let us now introduce an alternative definition of the VLISM. Holzer (1989) defined the LISM as the ISM within 100 pc of the Sun and the VLISM as the region within 0.01 pc of the Sun, i.e., within $\sim 2,000 \text{ AU}$. Because H atoms originating from the heliosphere that splash

back into the ISM have a charge-exchange mfp of approximately 50–100 AU and the equilibration length scale for PUIs and interstellar plasma is $> \sim 75$ AU, the ISM may be mediated by heliospheric processes within several 100 AU. The simulations of Zank et al. (2013) and Heerikhuisen et al. (2014) show that the creation of heliospheric PUIs modifies the interstellar temperature to at least approximately 700 AU of the Sun in the upwind direction. Thus, we advocate a definition of the VLISM that is the region of the ISM surrounding the Sun that is modified by the deposition of heliospheric material. A corresponding definition would be that the VLISM is the part of the ISM surrounding the Sun that is not equilibrated with either H or PUIs of heliospheric origin.

2. SUMMARY OF OBSERVATIONS

V1 crossed the HTS in December 2004 at a distance of 94 AU from the Sun, becoming the first spacecraft to enter the IHS (Burlaga et al. 2005, Decker et al. 2005, Gurnett & Kurth 2005, Stone et al. 2005). V2 crossed the HTS in August 2007 at a distance of 84 AU (Burlaga et al. 2008, Decker et al. 2008, Gurnett & Kurth 2008, Richardson et al. 2008, Stone et al. 2008), providing the first plasma measurements of the termination shock (TS) and heliosheath region. The Interstellar Boundary Explorer (IBEX) mission (McComas et al. 2004), launched on 19 October 2008, has augmented the in situ measurements of the *Voyager* Interstellar Mission by measuring ENAs in the energy range [0.1, 6] keV. Thus, the IBEX has introduced an exciting decade of new observations of the heliosheath-LISM interaction on a global scale and provided novel and unexpected insights into the SW-LISM interaction. The IBEX results have been complemented by the ion and neutral camera (INCA) on board Cassini (Krimigis et al. 2009), which measures ENA energies in excess of 6 keV.

Besides plasma and neutral particle measurements, the nature of the boundary regions has been elucidated globally by Lyman- α measurements, either through line-of-site absorption measurements toward nearby stars, or through measurements of solar Lyman- α backscattered by H atoms drifting through the heliosphere. The *Hubble Space Telescope Goddard High Resolution Spectrograph* made Lyman- α absorption measurements toward a variety of stars. The nonequibrated, heated, decelerated H between the HP and possible BS yields excess Lyman- α absorption compared with that due to interstellar H alone. The observation of the hydrogen wall (H wall) by Linsky & Wood (1996), and the interpretation by Gayley et al. (1997) was the first discovery of a heliospheric boundary region.

The earliest inferences of the properties of the ISM were derived from Lyman- α backscatter observations. In 1970, the OGO-5 spacecraft discovered the interstellar wind (the flow of neutral H and He atoms through the solar system) (Bertaux & Blamont 1971, Thomas & Krassa 1971). Since then, Lyman- α backscatter observations have been used to refine the characteristics of the interstellar flow (direction, velocity, temperature) (Bertaux et al. 1985, Lallement et al. 1993, Clarke et al. 1995).

2.1. In Situ Measurements: *Voyager 1* and 2 Observations

We present an overview of the V1 and V2 observations sorted according to region, i.e., the HTS, IHS, HP, and VLISM.

2.1.1. The heliospheric termination shock. V1 and V2 crossed the HTS and entered the heliosheath on 2004.96 (12/16/04) at heliographic coordinates of (34.3°, 173°) and on 2007.66 (8/30/07) at (−27.5°, 216°), respectively. Although V1 crossed the HTS well before V2, the actual crossing occurred during a data gap. V2 crossed during a period when data were being

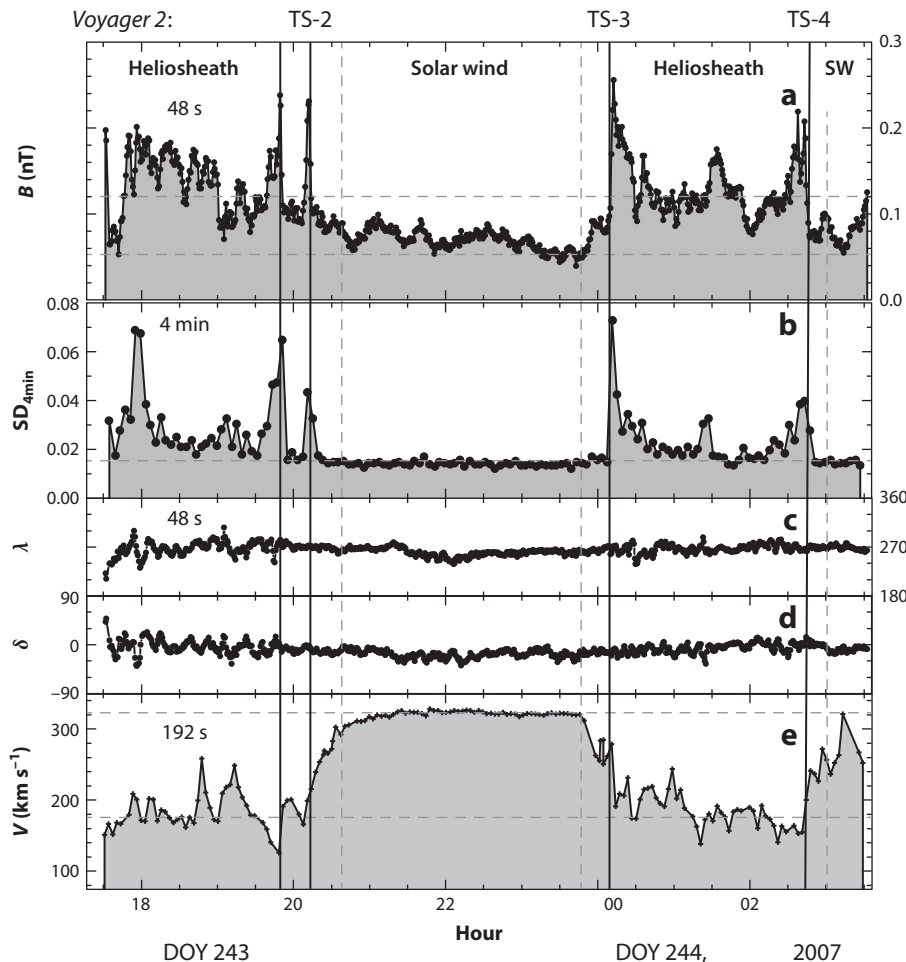


Figure 2

(a) Magnetic field strength B measured using 48-s averages, (b) standard deviation (SD), (c) azimuthal angle λ , (d) elevation angle δ , and (e) 192-s averages of the solar wind (SW) speed V ; all values plotted as a function of time measured in days from the beginning of 2007. Reprinted from Burlaga et al. (2008) with permission.

returned and the observations proved transformational. V2 crossed the HTS at least five times between 2007/242.14 and 2007/244.80, when V2 was at ~ 83.7 AU and 27.5° S (Burlaga et al. 2008). Additional crossings may have occurred in the data gaps. The crossing of V2 was ~ 10 AU closer in heliocentric distance than was the nominal V1 HTS crossing (~ 94 AU). The latitudinal asymmetry of the HTS may be due to the asymmetric interstellar magnetic field (ISMF) or temporal variability of the supersonic SW during the period between the crossings (Stone et al. 2008).

Shown in **Figure 2** are the five TS crossings. HTS crossing TS-1 occurred in a data gap between 2007/242.140 and 2007/242.715. V2 observed three crossings: TS-2 at 2007/243.842, TS-3 at 243.996, and TS-4 at 244.114. A fifth crossing (TS-5) occurred in a data gap between 2007/244.148 and 2007/244.799. The multiple crossings of the HTS by V2 suggest that the HTS was in continual motion, possibly moving back and forth across V2. Alternatively, or as well as, the HTS may have ripples sweeping along the shock front.

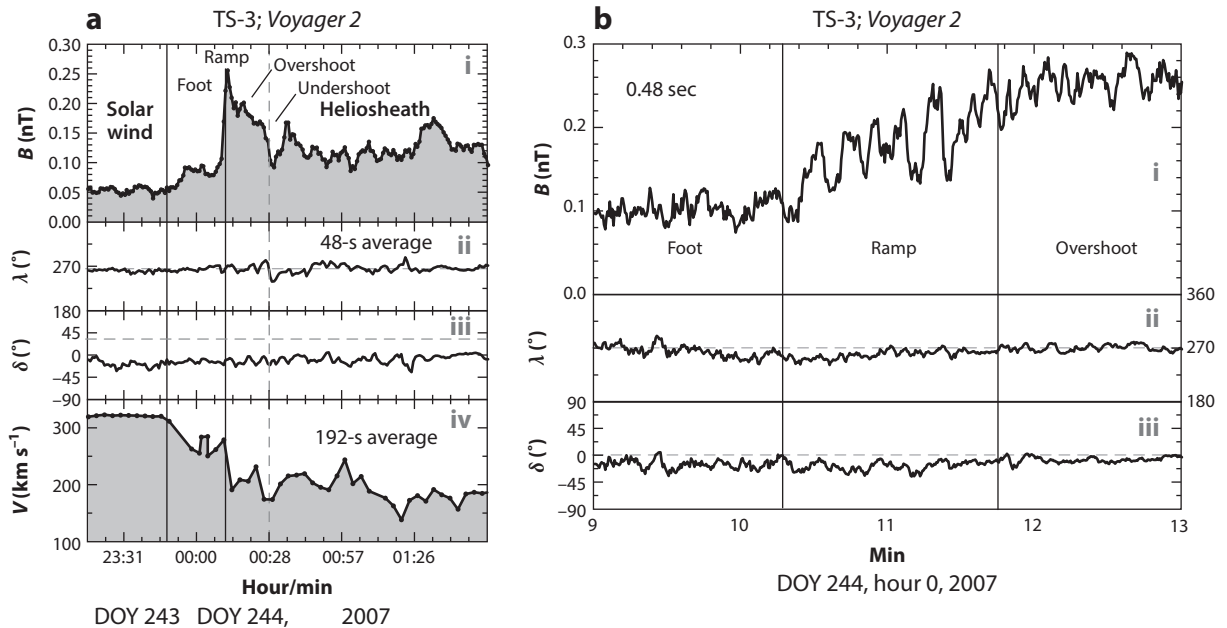


Figure 3

(a) (i) Magnetic field strength B measured using 48-s averages, (ii) its direction λ , (iii) elevation angle δ , and (iv) 192-s averages of the solar wind speed V across TS-3. Clearly visible are an extended foot, a ramp, the magnetic field overshoot, and trailing oscillations. (b) (i) The internal structure of the ramp of TS-3, based on observations of the magnetic field strength B ; (ii) azimuthal angle λ ; and (iii) elevation angle δ at 48-s intervals. Reprinted from Burlaga et al. (2008) with permission.

As illustrated in **Figure 2c**, there was little change in the direction of the magnetic field \mathbf{B} in the observed shock crossings TS-2, TS-3, and TS-4, indicating that the HTS on each crossing was highly perpendicular. In the SW upstream of TS-3, the Alfvén speed was $V_{A,u} \simeq 40 \text{ km s}^{-1}$ and the Alfvén Mach number of the SW was $M_{A,u} \simeq 8$. Burlaga et al. (2008) suggested that the HTS was supercritical with a magnetosonic Mach number of $>2-3$ based on estimates of the PUI pressure.

The structure of the HTS crossing TS-3 (**Figure 3a**) is remarkably consistent with the “classical” structure exhibited by quasi-perpendicular shocks. The structure of TS-3 is consistent with our current understanding of quasi-perpendicular shock structure (e.g., Goodrich 1985, Lembège et al. 2009) where dissipation is provided by ion reflection at the cross-shock potential. The TS-3 shock compression ratio, as measured by the ratio of the upstream to downstream B is 1.7 ± 0.1 , which is consistent with the corresponding density ratio of 1.4 ± 0.2 . Therefore, the HTS is comparatively weak.

Figure 3b shows that the HTS ramp possesses considerable fine structure, exhibiting quasi-periodic oscillations. Burlaga et al. (2008) attempted to estimate the scales of TS-3, including the fine structure. However, the TS-3 structure observed by V2 is a single spacecraft measurement that does not include the PUI component because V2 has no instrument for this energy range. As a result, determining shock speed and shock normal is exceedingly difficult. The different structures exhibited by the three observed crossings may be attributed to these being different periods of shock reformation (Burlaga et al. 2008, Lembège et al. 2009).

It was widely expected that the SW would undergo a transition from supersonic to subsonic flow at the HTS, with an accompanying heating of the SW plasma. However, the V2 plasma instrument

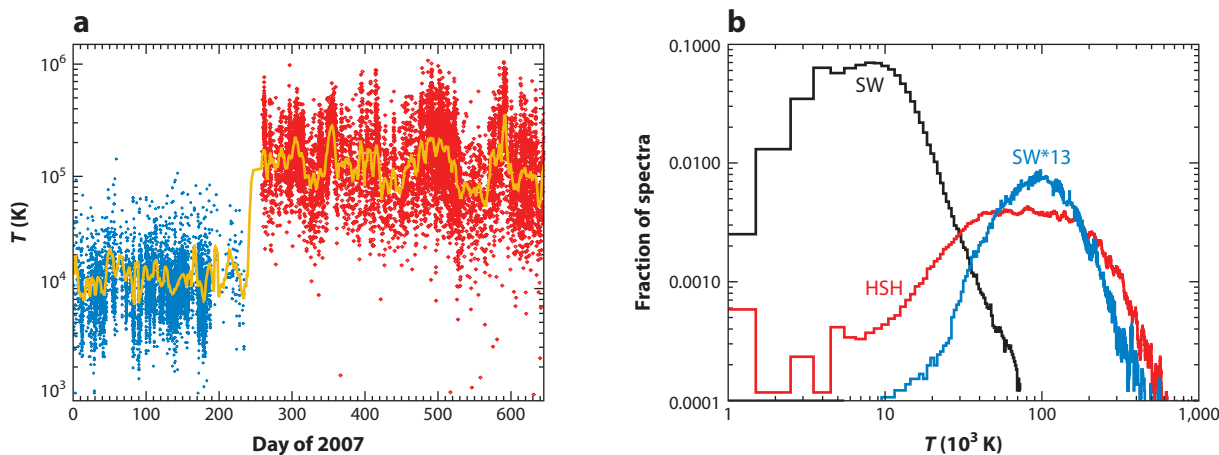


Figure 4

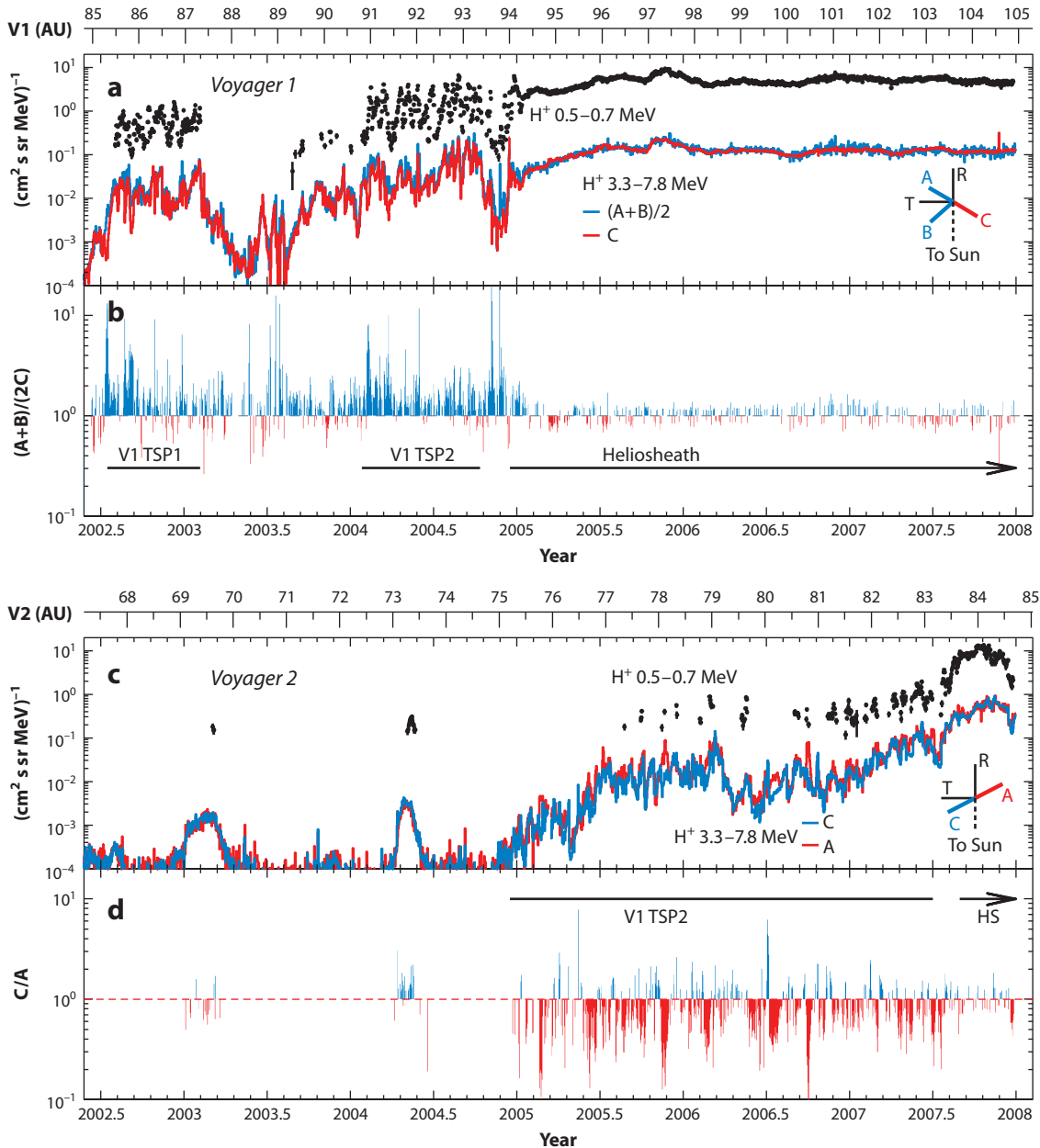
(a) Solar wind (SW) thermal proton temperature observed by *Voyager 2* across the heliospheric termination shock: (*points*) high-time-resolution data, (*lines*) daily averages. (b) Histograms of the temperature distributions in the SW and inner heliosheath (HSH): (*black*) SW distribution, (*red*) HSH distribution, and (*blue*) distribution of the SW temperature multiplied by 13, the ratio between the upstream SW and downstream HSH temperatures. No reflected SW protons can be identified from the distribution function. Adapted from Richardson et al. (2008) with permission.

during the 2007/242–244 TS crossing(s) measured both less SW heating than expected and a downstream flow speed that remained supersonic with respect to the heated SW sound speed. The observed temperature of less than $\sim 200,000$ K indicated that $\sim 80\%$ of incident SW ram energy had to be heating some particle population other than that of the SW, possibly PUIs, (**Figure 4**) (Richardson 2008, Richardson et al. 2008). In their investigation of the interaction of PUIs and SW ions with the HTS, Zank et al. (1996a) predicted that PUIs provide the HTS dissipation and heated downstream plasma. They concluded that “P[U]Is may therefore provide the primary dissipation mechanism for a perpendicular [H]TS with solar wind ions playing very much a secondary role” (Zank et al. 1996a, p. 472). Thus, SW ions were expected to be heated modestly.

Richardson et al. (2009) presented observations of quasi-periodic (110 days) oscillations in the IHS, possibly due to periodic variations of the TS normal direction. A surprise from the V1 HTS crossing was that the intensity of ACRs did not peak at the shock as anticipated (**Figure 5**) (Stone et al. 2005). Both V1 and V2 observed low-energy ions, called termination shock particles (TSPs), ahead of the HTS. The TSPs are thought to be accelerated at the HTS. V2 began observing upstream energetic ions at 75 AU from the Sun, roughly 10 AU closer than were observed at V1. Although there has been little variation in the intensity of TSPs observed by V1 in the heliosheath since mid-2005, the intensity of $1\text{--}1.5$ MeV nuc^{-1} He nuclei and $4\text{--}5$ MeV protons at V2 just after it crossed the HTS was three times larger than V1 observed when it crossed.

Figure 6 compares the proton and He energy spectra observed in the IHS at and close to the times of the V1 and V2 shock crossings. During the 2004 period, V1 and V2 were at 94.1 AU and 75.2 AU, respectively. During the 2007 period, V1 was at 103.8 AU and 34.3°N heliographic latitude, and V2 was at 83.7 AU and 27.5°S . Three components are apparent in the V2 spectra: TSPs convected from nearby shock regions (<6 MeV), ACRs that are modulated in the heliosheath ($8\text{--}150$ MeV), and galactic cosmic rays (GCRs) (>200 MeV). The ACR and GCR intensities increased from 2004 to 2007 as solar modulation decreased with declining solar activity. In 2007,

the V2 TSP intensity at 4–5 MeV was three times larger than that at V1 and the spectrum from 0.5 to 3 MeV was $\sim E^{-1.1\pm 0.1}$, which was harder than the V1 spectrum. The TSP spectra have breaks at ~ 3 MeV, with the V2 spectrum falling as $E^{-3.1\pm 0.1}$ from 5 to 30 MeV. **Figure 6** shows three He components. In the 2004 period, the ACR component was observable down to ~ 10 MeV nuc^{-1} . By the 2007 period, the intensity of 12–22 MeV nuc^{-1} ACR He at V1 increased by a factor of 21 ± 4 as the spectrum approached the expected power law source spectrum. The intensity at V2 increased by a factor of 20 ± 3 .



Stone et al. (2008) concluded that the similarity of the changes at V1 in the heliosheath and V2 upstream between the V1 and V2 shock crossings indicated a common temporal change due to decreasing solar modulation. As a result, the V2 intensity of 12–22 MeV nuc^{-1} He just after the shock was 8.4 ± 1.8 times the intensity at V1 just after its crossing. This intensity was, however, a factor of 2.5 ± 0.4 smaller than the concurrent V1 intensity in the heliosheath, which has been interpreted as indicating that V2 did not observe the expected ACR source spectrum near the shock. Other acceleration mechanisms may operate in the IHS, and the HTS and IHS observations may be due to a superposition of different acceleration mechanisms for ACRs (e.g., Fisk & Gloeckler 2006, Lazarian & Opher 2009, Drake et al. 2010).

Because V1 was relatively deep into the IHS at the time V2 crossed the HTS, the ACR gradients in the heliosheath could be determined (see **Figure 7**) (Stone et al. 2008). The V2 and V1 He intensity ratios at 12–22 MeV nuc^{-1} (Stone et al. 2008) correspond to a radial gradient of 4.5% AU^{-1} in the IHS, which could possibly be smaller if longitudinal or latitudinal gradients were present.

V1 and V2 measured high intensities of nonthermal ions and electrons on both sides of the HTS (Krimigis et al. 2003; McDonald et al. 2003; Decker et al. 2005, 2006; Stone et al. 2005). The plasma and magnetic field data from V2 discussed above indicate that nonthermal ion distributions likely play an important role in mediating dynamical processes at the HTS and in the heliosheath. Decker et al. (2008) found that intensities of low-energy ions measured at V2 have a nonthermal partial ion pressure in the heliosheath that is comparable to (or exceeds) both the thermal plasma pressures and the scalar magnetic field pressures (illustrated in **Figure 8**). They concluded that ions with >0.028 MeV dominate the nonthermal ion distribution that determines the TS structure and whose acceleration extracts a large fraction of bulk flow kinetic energy from the incident SW.

The low-energy charged particle (LECP) instrument revealed that, during the 40 days before the V2 HTS crossing, the intensities of energetic ions increased exponentially, and their spectra showed clear evidence of unfolding at low energies (**Figure 8**) (Decker et al. 2005). Simultaneously, the plasma data exhibited a broad velocity precursor (Richardson et al. 2008), with the SW speed decreasing from ~ 380 km s^{-1} far upstream to ~ 300 km s^{-1} at the HTS, both gradually and in two abrupt steps. The abrupt changes appear to be associated with magnetic structures (Burlaga et al. 2008, 2009b), which are possibly merged interaction regions or compressive features associated with the shock precursor. Florinski et al. (2009) used plasma and energetic particle conservation laws (Drury & Völk 1981, Axford et al. 1982, Donohue & Zank 1993, Zank et al. 1993) to show that the speed decrease in the SW after the second MIR-like structure was due to energetic ions with energies of a few megaelectron volts mediating the upstream plasma flow. These particles

Figure 5

Daily-averaged intensities and streaming of energetic TSPs that are accelerated at nearby regions of the shock: (*insets*) the telescope viewing directions projected into the R-T plane ($-R$ is the coordinate directed toward the Sun, and T is the coordinate in the azimuthal direction). (a) The proton intensities (H) at 3.3–7.8 MeV observed by V1 particle telescopes (A + B)/2 and C are highly variable upstream of the shock owing to variations in the connectivity along the interplanetary magnetic field line. Energetic ions are convected into the IHS, resulting in reduced variations. Similar properties are apparent in the intensity of 0.5- to 0.7-MeV protons. (b) The streaming index (A+B)/2C shows that the upstream ions at V1 were strongly beamed in the $-T$ direction, with intensities in the oppositely directed detectors differing by up to a factor of 10. The intensities are more nearly isotropic in the IHS. (c) Same as panel a, except only telescopes A and C are used for V2. (d) Same as panel b except only telescopes A and C are used for V2. The upstream beaming was mainly in the $+T$ direction, opposite to that observed by V1 and consistent with an east-west shock asymmetry resulting from a local interplanetary magnetic field. Reprinted from Stone et al. (2008) with permission. Abbreviations: IHS, inner heliosheath; TSP, termination shock particle; V1, *Voyager 1*; V2, *Voyager 2*.

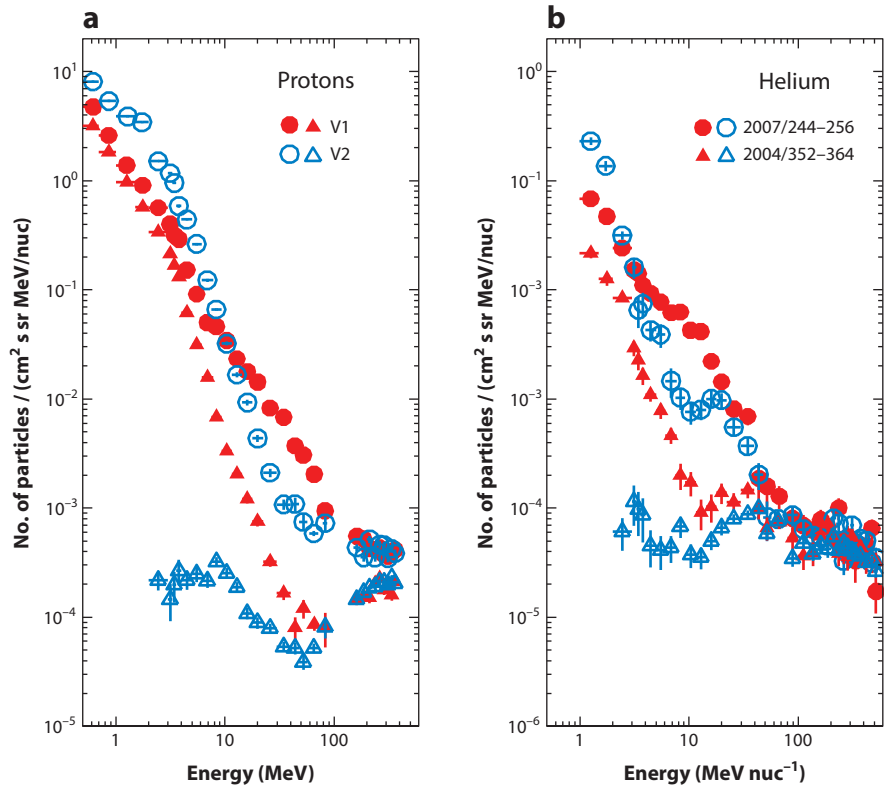


Figure 6

(a) Proton and (b) helium spectra observed in the heliosheath at and close to the (red) *Voyager 1* (V1) and (blue) *Voyager 2* (V2) crossing times: (triangles) observations made at the time of the V1 heliospheric termination shock (HTS) crossing, (circles) observations made at the time of the V2 HTS crossing, (red triangles and blue circles) HTS-accelerated spectra at the time of each crossing. Reprinted from Stone et al. (2008) with permission.

propagate diffusively upstream from the HTS, producing a shock precursor that has a characteristic length scale of ~ 0.35 AU for a steady-state shock.

Both the V1 and V2 plasma wave analyzers (PLS) detected upstream plasma oscillations ahead of the TS (Gurnett & Kurth 2005, 2008). The plasma wave oscillations, also known as Langmuir waves, are purely electrostatic oscillations that occur at the characteristic electron plasma frequency, proportional to the electron number density as $\sqrt{n_e}$. V1 detected oscillations approximately 10 months before the HTS crossing, whereas V2 detected Langmuir waves just 30 days before the five crossings of the HTS. Three intense bursts of broadband electric field noise from 31 August to 1 September 2007 were observed. Such events are extremely rare and exhibit the intense broadband electrostatic wave spectrums that were expected at the HTS. Two events coincided with the V2 crossing times of TS-3 and TS-4, but no shock crossing coincided with the third event. The electric field spectrum at TS-3 has a shape that is very similar to those observed at planetary BSs, after suitable normalization (Gurnett & Kurth 2008). Therefore, the basic processes for driving electrostatic oscillations in foreshocks are likely common to both planetary BSs and the HTS.

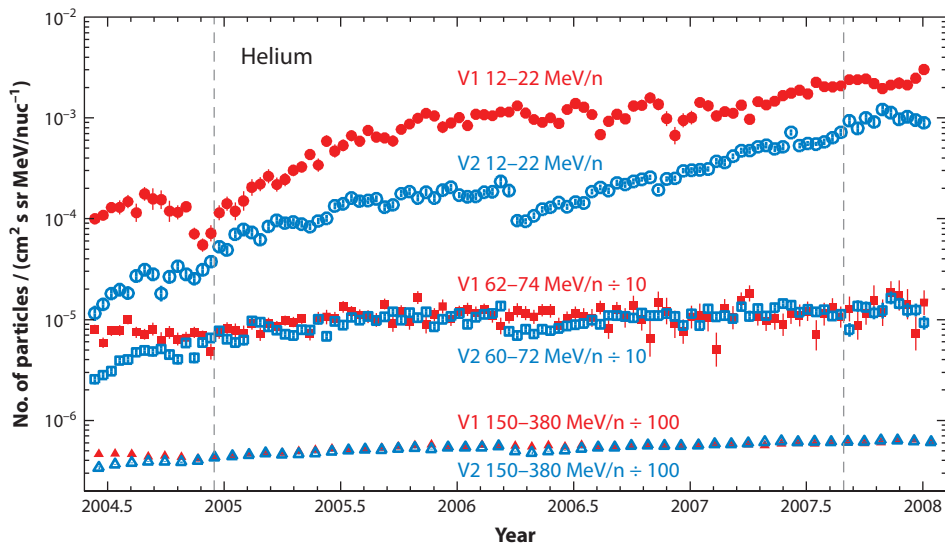


Figure 7

Temporal changes in the intensities of helium nuclei in three energy bands, and electrons: (vertical dotted lines) times of the *Voyager 1* (V1) shock crossing (2004.96) and the *Voyager 2* (V2) crossing (2007.66), after which both spacecraft were in the heliosheath. Anomalous cosmic rays dominate the two lowest energy bands plotted, and galactic cosmic rays dominate the highest energy band. Reprinted from Stone et al. (2008) with permission.

2.1.2. The inner heliosheath. The *Voyager* spacecraft observed the IHS in situ since 2004 (V1) and 2007 (V2), and V1 exited in August 2012. V1 is at $\sim 35^\circ\text{N}$ heliolatitude, almost directly above the nose of the heliosphere, and V2 is near 30°S heliolatitude and also $\sim 30^\circ$ from the nose in heliolongitude. Although traveling in the same upwind direction, V1 and V2 are more than 140 AU apart. Some IHS characteristics, such as energetic ion intensities, are surprisingly similar at V1 and V2, but others, such as the plasma speeds, are dramatically different.

Burlaga et al. (2006) and Burlaga & Ness (2009) presented observations of linear waves, “compressible” turbulence, and structures in the IHS. Virtually no supporting theoretical analysis exists yet. Burlaga et al. (2006) investigated a relatively short period in the post-HTS region, when V1 was in a sector of positive polarity for 125 days. Throughout the sector, the distribution functions of each of the hourly averaged \mathbf{B} component fluctuations were essentially Gaussian with similar widths, indicating that the fluctuations were nearly isotropic relative to the mean magnetic field. The distribution of hourly averages of the magnetic field B was Gaussian. The Gaussian distribution of B in the heliosheath (in contrast to the lognormal distributions of B in the supersonic SW) suggests that some process tends to equilibrate the plasma in the heliosheath, driving it toward a Boltzmann-Gibbs distribution. The magnetic fields of the supersonic SW were transmitted through the HTS into the IHS. The HTS may have isotropized the fluctuations in the components of \mathbf{B} , removing the skewness and kurtosis of the distribution of B (Burlaga et al. 2006). This hypothesis has not been tested and quantified.

The nature of the IHS “compressible” turbulence was further confirmed by V2 observations presented by Burlaga & Ness (2009), who compared turbulence in a region of constant magnetic field direction (“unipolar region”) with that observed in a post-HTS region. Daily and 48-s averages of B were lognormal in the post-HTS region and Gaussian in the unipolar region. The lognormal distribution in the V2 post-HTS region contrasted with the V1 observations of

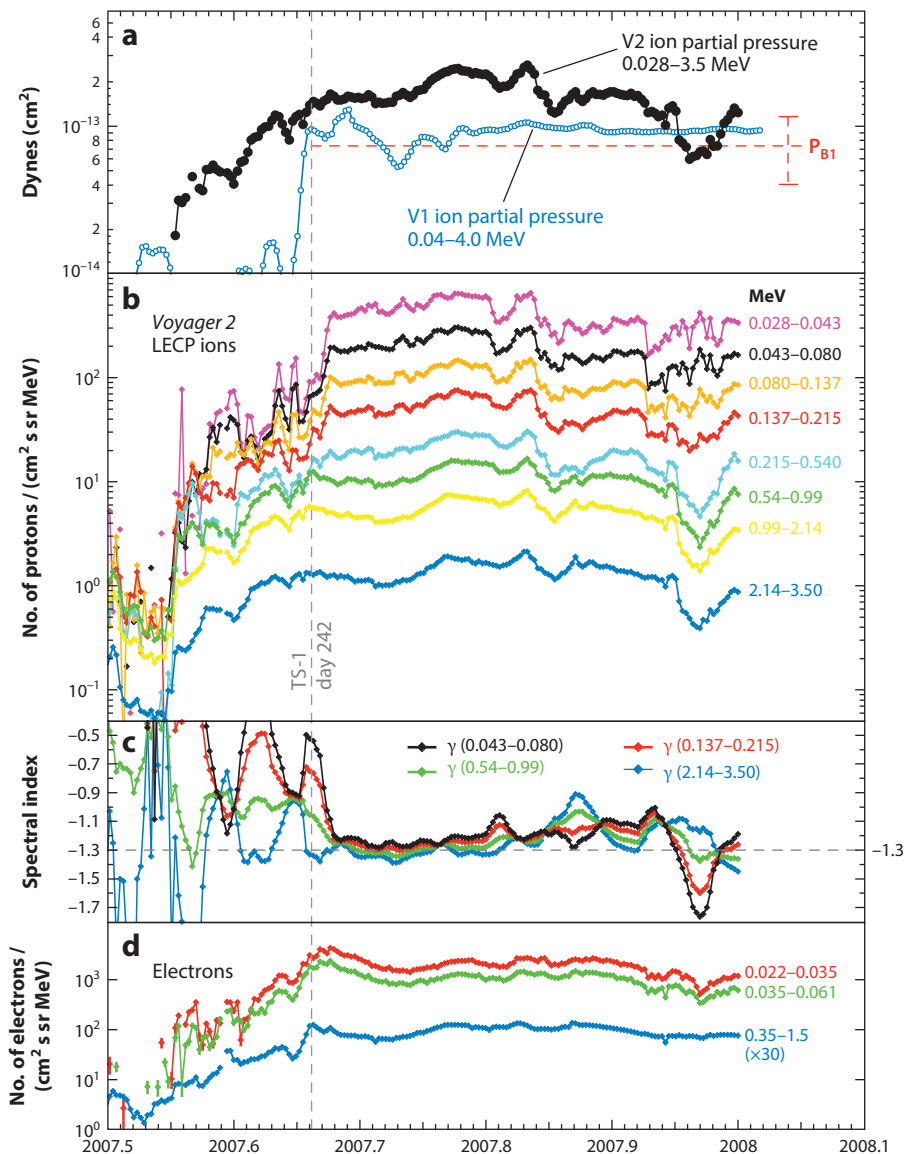


Figure 8

(a) Ion (proton) pressure computed (*black trace*) in the energy range 0.028–3.5 MeV for V2 and (*blue trace*) in the range 0.040–4.0 MeV at the end of the V1 HTS crossing for V1. Both exceed the magnetic field pressure $P_{B1} = B_1^2/8\pi$ (*horizontal dashed red line*) calculated using the V1 mean heliosheath field intensity $B_1 = 0.123 \pm 0.035$ nT during 2005/001–110. The upper and lower bounds of the vertical error bar are P_{B1} evaluated at $B_1 = 0.158$ and 0.088 nT. (b) Intensities in the eight V2 ion channels calculated using proton energy passbands and efficiencies. (c) Differential spectral index $\gamma(E)$ evaluated at logarithmic mean of energy passband for channels indicated. (d) Electron intensities in the energy range 0.022–1.5 MeV. Ordinate of the blue trace is multiplied by 30. Electron intensities that peak at or near the HTS are nearly isotropic in the solar wind and heliosheath, and at ≈ 0.03 MeV (≈ 0.7 MeV), they are higher (lower) than the intensities of ions at the same energy by a factor ≈ 4 (≈ 3). Reprinted from Decker et al. (2008) with permission. Abbreviations: HTS, heliospheric termination shock; LECP, low-energy charged particle; TS, termination shock; V1, *Voyager 1*; V2, *Voyager 2*.

Gaussian distributions. Burlaga & Ness (2009) suggested that the lognormal distribution observed in the post-HTS region may be a remnant of the lognormal distribution observed typically in the SW, owing in part to the unusual nature of the HTS. Both V1 and V2 observed Gaussian distributions of daily and 48-s averages of B in the unipolar region. Burlaga & Ness (2009) speculated that either (a) the Gaussian distribution in the unipolar region evolved from a lognormal distribution in the post-HTS region as the plasma propagated away from the HTS or (b) that the unipolar region may be a different kind of flow than the rest of the post-HTS region. They concluded that these hypotheses cannot be tested observationally but should be explored by theories and models.

The distribution of B observed by V1 during 2009 was lognormal, in contrast to the Gaussian distributions observed by V1 in the heliosheath prior to 2009. The large-scale fluctuations of daily averages of B observed by V1 during 2009 possess a power law spectrum with slope -1.7 ± 0.3 in the range 2.9×10^{-6} – 3.6×10^{-7} Hz (i.e., periods from 4 to 32 days). Time series of the magnitude and direction of \mathbf{B} show that the fluctuations are highly compressive. The turbulence includes “kinetic-scale” features (~ 10 – 100 gyroradii), such as isolated magnetic holes and humps, as well as trains of magnetic holes and humps (Burlaga et al. 2006) and “microscale” features (> 100 proton gyroradii) on fluidlike scales. The small-scale fluctuations (both kinetic-scale and microscale fluctuations) may be related to either mirror-mode disturbances generated by temperature anisotropies at the TS (Liu et al. 2007) or PUI-related nonlinear structures (Avinash & Zank 2007, Avinash et al. 2009). Therefore, small-scale fluctuations are a mixture of coherent structures and random structures, which vary significantly from day to day.

Gutynska et al. (2010) investigated correlations between the magnetic field data and density fluctuations in the IHS. They investigated two IHS regions: a post-HTS region, which exhibited many current sheet crossings, and a unipolar magnetic field region. They found the following:

1. Correlated strong magnetic field and density changes lie in the frequency range 1×10^{-4} to 4×10^{-3} Hz in both regions.
2. The cross-correlation coefficient of these quantities is quite high, ~ 0.6 in both regions, but slightly larger in the unipolar region located farther from the HTS.
3. Typical periods of the fluctuations range from 50 min to 220 min.
4. The cross-correlation coefficient increases with the period of the dominant wave in the frequency spectrum.
5. The larger cross-correlation coefficients observed in the unipolar region are consistent with long-period fluctuations.

Similar to the findings of Burlaga et al. (2006, 2009b), Gutynska et al. (2010) concluded that heliosheath fluctuations are generated at the HTS. However, they also believed that waves of higher frequencies are damped and lower frequency waves predominate at larger distances from the HTS.

Many of the differences between V1 and V2 observations may result from the different lengths of time spent within the sector zone. V1 remained mostly within the sector zone, in the presence of the HCS, whereas V2 was in unipolar zones below the HCS for much of the time (Burlaga & Ness 2011, Richardson et al. 2013). The polarity pattern of the magnetic field of the heliosheath observed by V1 evolved after the HTS crossing (Burlaga & Ness 2010). After crossing the HTS, V1 observed a “two-sector pattern” (i.e., both positive and negative magnetic polarities with nearly equal probability), as the sector pattern from the supersonic SW was advected into the heliosheath (Burlaga et al. 2005). The two-sector pattern persisted from 2005 to 2006.2, at which time V1 appeared to enter a region of negative polarity (corresponding to the polarity of magnetic fields from the northern polar coronal hole), as the maximum latitudinal extent of the HCS dropped below that of V1. If V1 were not in the heliosheath, it would continue to observe negative polarities associated with flows from the northern polar coronal hole. For this reason, in the absence of other

effects, one would expect V1 to observe negative polarities through 2010 as the HCS continued to move equatorward while solar activity decreased to a historically quiet solar minimum. However, V1 observed brief intervals of positive magnetic polarity during 2006–2008. Burlaga & Ness (2010) attributed these anomalous positive polarities to the northward convection of the HCS in the heliosheath (Burlaga et al. 2009a,b), because models predict a northward flow in the northern part of the heliosheath traversed by V1 (Washimi & Tanaka 2001; Pogorelov et al. 2004, 2006, 2008; Zank et al. 2009).

Burlaga et al. (2009a,b) did not report a large B gradient in the IHS. They ascribed this lack of large gradient to a balance between (a) an increase in B with radial distance from the Sun, as predicted by stationary models of the IHS, and (b) a decrease in B due to decreasing solar activity. The flow velocities inferred at V1 and observed at V2 are very different. V2 has measured the shocked SW in the heliosphere since it crossed the HTS in August 2007. The plasma instrument on V1 does not work, but the Compton-Getting effect (Gleeson & Axford 1968) has been used to derive plasma speeds V_R and V_T in the R and T directions from LECP observations (Decker et al. 2005, 2010) for the heliosheath region traversed by V1: R is radially outward, T is in the plane of the solar equator and positive in the direction of solar rotation, and N completes the right-handed system. In 2011, the *Voyagers* researchers initiated a series of spacecraft rolls that allowed the LECP instrument to occasionally determine V_N (Decker et al. 2012; see also Stone & Cummings 2012). The LECP results (**Figure 9**) showed that the radial flow was approximately 80 km h^{-1} after the V1 HTS crossing and then decreased steadily to zero in early 2010 (Krimigis et al. 2011). The radial speed remained near zero through August 2012, just prior to the crossing of the HP. According to measurements, the T component of the velocity was steady, -40 km s^{-1} , until 2011, when its magnitude decreased to approximately 20 km s^{-1} . The N component was northward and was roughly equal to the R component, also approaching zero in 2010 (Decker et al. 2012, Stone & Cummings 2012).

Comparison of the velocities shows very different flow characteristics in the V1 and V2 directions (Richardson & Wang 2012, Richardson & Decker 2014). Compared with V1, V2 has observed faster flow speeds throughout the heliosheath with the flow direction turning toward the heliotail (Richardson et al. 2009). Unlike the V1 data in which V_R decreases nearly monotonically across the heliosheath, approaching zero near the HP, the V2 data show a very slow decrease [$\sim 8 \text{ km (s} \cdot \text{year)}^{-1}$] in V_R (Richardson & Decker 2014).

The nonradial components of velocity are expected to increase as the flow turns and moves toward the polar regions and tailward (Zank et al. 1996b; Pauls & Zank 1997; Pogorelov et al. 2004, 2006; Washimi et al. 2007, 2011). This was not observed at V1, V_T remained almost constant from the HTS to the stagnation region, and V_N decreased as V_R decreased. At V2, both V_T and V_N increased across the heliosheath (Richardson & Decker 2014). Curiously, V_T and V_N are correlated after mid-2011, increasing and decreasing in unison for several months at a time (Richardson & Decker 2014).

The density decreased by a factor of two in 2008, after which it recovered in 2011 (Richardson & Wang 2012). After recovering, the average density has remained fairly constant with a value of 0.0018 cm^{-3} in 2013, comparable to the density of 0.0021 cm^{-3} observed in 2007 in the post-HTS region. In the six months after the HTS crossing, the temperature decreased by a factor of three but has not varied greatly since 2009, and in 2013, it averaged 28.8 km s^{-1} , corresponding to a temperature of $50,000 \text{ K}$. The early decreases shortly after the HTS crossing by V2 were interpreted (Richardson et al. 2009) as being due to solar-cycle effects.

The average value of $|\mathbf{V}|$ has not changed greatly as V2 traversed the heliosheath, ranging from 125 to 175 km s^{-1} : Changes typically last several months and have an average value of $\sim 146 \text{ km s}^{-1}$. Increases in V_T and V_N compensate for the modest decrease in V_R . A constant V is inconsistent

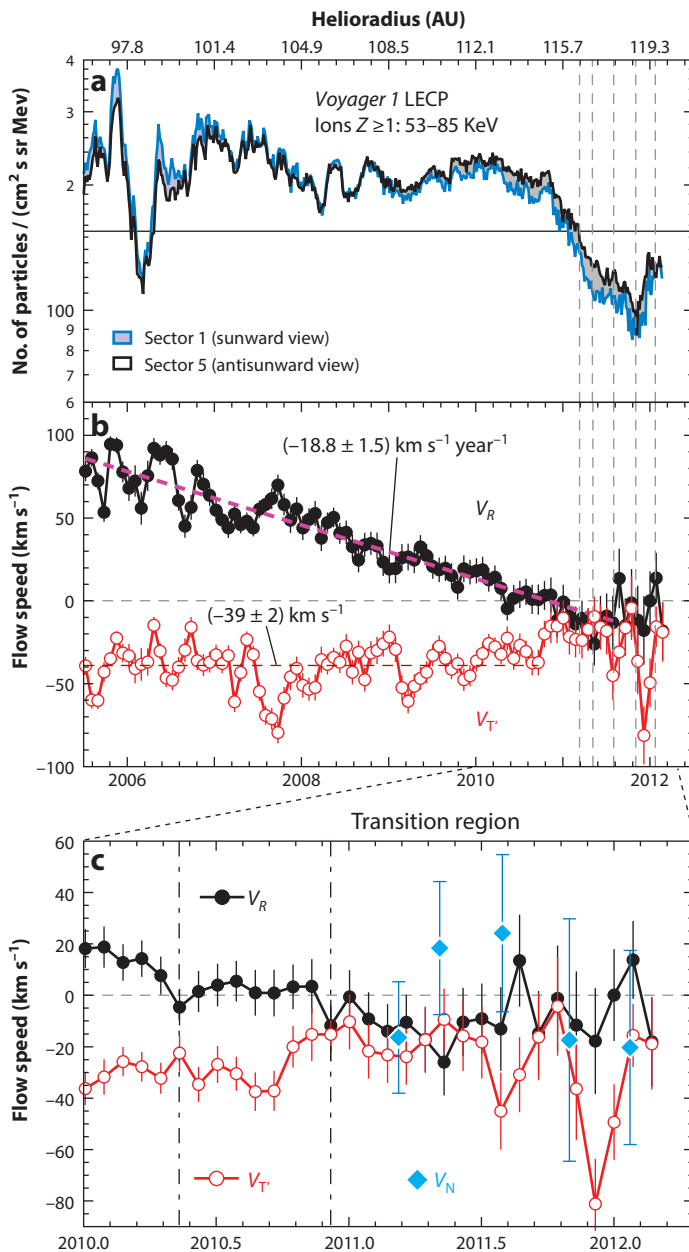


Figure 9

(a) Intensity of 53–85 keV protons: (blue and black curves) intensities in sectors 1 and 5 of particles arriving from the sunward and antisunward directions, respectively. The heliocentric distance of *Voyager 1* is shown on the top axis: (dashed vertical lines) roll periods. (b) Plasma flow velocity components V_R and V_T as 26-day averages. (c) Expanded view of the middle panel including the five roll cycles of V_N (diamonds): (first dot-dash vertical line) onset at $\sim 2010/133$ of a 208-day (2.05 AU) period of zero V_R ; (second dot-dash vertical line) at $\sim 2010/341$ marks the end of the steady zero- V_R flow and the transition to variable and often negative $-V_R$ flow. Reprinted from Decker et al. (2012) with permission. Abbreviation: LECP, low-energy charged particle.

with models and is very different from V1 observations that show a decrease in V from $\sim 100 \text{ km s}^{-1}$ in 2005 to near zero in 2010. After the HTS crossing in 2007, the average RN angle is -9° , which increased to an average of -27° in 2013. The RN angles are not as large as the RT angles: RN is -27° in 2013, and the corrected RT values are 58° , i.e., the IHS plasma flow observed by V2 is turning faster in the T than in the N direction, with a flow angle of $\sim 60^\circ$ from radial in the RT plane and 30° from radial in the RN plane.

Because the difference in the flows observed by V1 and V2 resulted from different measurement techniques (plasma data were used for V2 and a Compton-Getting analysis on the low-energy particle data for V1), Richardson & Decker (2014) compared the two measurement techniques using V2 plasma science instrument PLS and LECP data. The Compton-Getting analysis assumes that the ion composition is known and that the observed anisotropies arise from the convective flow. Where PLS and LECP speeds can both be reliably determined, the values are comparable. Both the V2 LECP and PLS observe much higher values of V_R than the LECP observed at V1 and a very slow decrease in V_R across the IHS. Both the PLS and LECP observe an increase in V_T across the heliosheath, which is again very different than the constant low-speed V_T observed by V1. Where the LECP and PLS disagree, the LECP values are larger than the PLS values. Thus, similar problems with the Compton-Getting technique at V1 would also give larger values of V_T and V_R instead of the lower values that were observed. Richardson & Decker (2014) therefore concluded that the data are consistent with the flow speeds in the V1 and V2 directions being very different, and the differences cannot be ascribed to instrumental effects.

For a radial flow, such as the supersonic SW upstream of the HTS where the magnetic field is in the T direction, the magnetic flux $V_R B R$ is constant assuming no sources or losses of magnetic flux. Richardson et al. (2013) found that the magnetic flux is constant at V2 but not at V1. At V1, the magnetic flux decreases by almost an order of magnitude as V1 approaches the HP. Changes at the solar source or nonradial transport do not appear to account for the changes. As discussed above, V1 was in the sector zone, so significant reconnection may have occurred to remove the flux. However, although a magnetic reconnection signature was observed near a sector boundary in the heliosheath in the V1 magnetic field data (Burlaga et al. 2006), it was unique in the V1 data, suggesting that reconnection is not important in the IHS. Therefore, why the magnetic flux decreased as V1 traversed the IHS remains unclear, although time dependence may be responsible.

Observations of energetic particles by LECP instruments on V1 and V2 have revealed the large contribution that PUIs and ACRs make to the total pressure in the IHS (Decker et al. 2008, 2010, 2015; Gloeckler & Fisk 2010; Krimigis et al. 2011, 2013; Fisk & Gloeckler 2014). The importance of the energetic particle pressure is illustrated in **Figure 10**. Evolution of the low-energy ion intensities in the 80–140-keV range and other channels from the V1 and V2 LECP were remarkably similar, on average, until the V1 HP crossing. The partial pressures in **Figure 10b** also evolved similarly, showing approximately the same magnitude and decay rate during 2012.0–2013.0. The lowest pressure measured by V2 was $\sim 5.5 \times 10^{-14} \text{ dyne cm}^{-2}$ during ~ 2013.0 – 2013.15 , which is a sevenfold drop from the post-HTS maximum of $3.5 \times 10^{-13} \text{ dyne cm}^{-2}$ in 2007.8 and a threefold drop from the peak pressure in 2011. Because the suprathermal ion partial pressure is $\sim 15\%$ of the total pressure in the heated IHS (Roelof et al. 2010), the IHS, similar to the supersonic wind in the distant heliosphere, is in a high-plasma beta state. Finally, despite the propagation of numerous shocks through the IHS, no reports of plasma frequency oscillations associated with these shocks have been reported.

2.1.3. Heliopause crossing and the very local interstellar medium. The speeds inferred from the LECP measurements at V1 decreased across the heliosheath reaching zero in April 2010 at $\sim 113.5 \text{ AU}$. This led to the suggestion that V1 was in a boundary layer in front of the HP (Krimigis

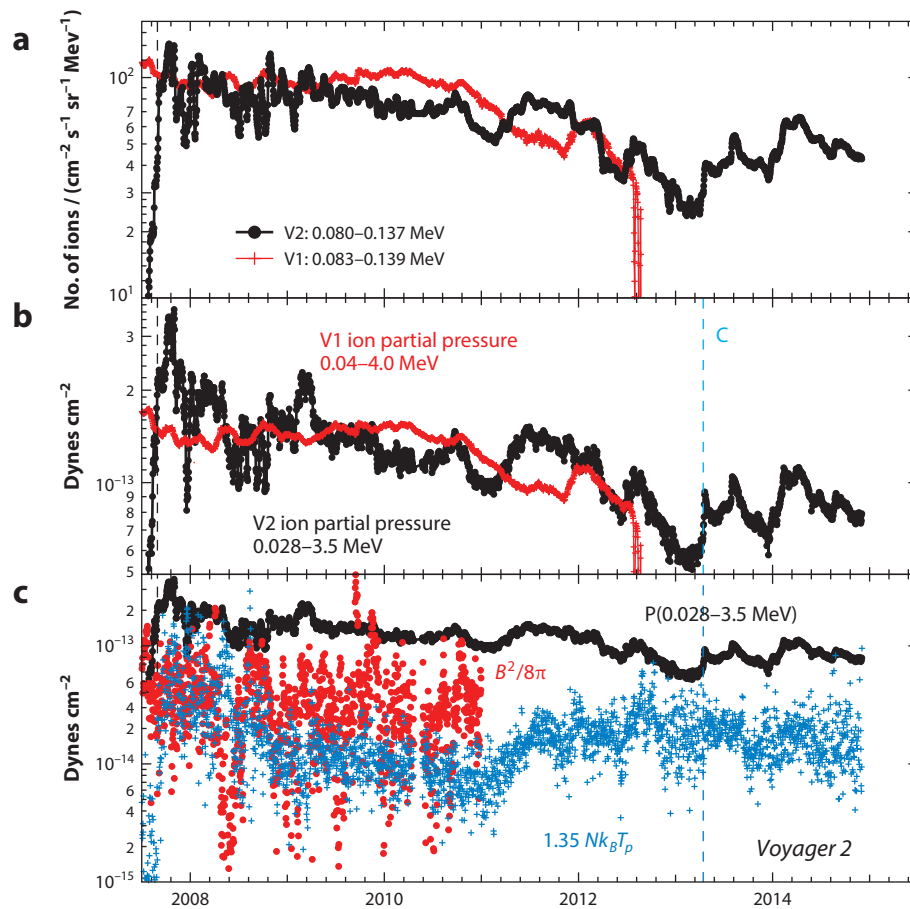


Figure 10

(a) Daily intensities of ions ~ 80 – 140 keV at *Voyager 1* (V1) and *Voyager 2* (V2) in 2007.5–2014.4, i.e., the ~ 7 years V2 has been in the inner heliosheath (IHS). (b) Partial pressure of suprathermal ions (assumed to be protons) at V1 (0.04–4.0 MeV) and V2 (0.03–3.5 MeV). Line C indicates where $+T$ directed ion streaming at V2 abruptly stopped and ion intensities increased. (c) Partial ion pressure at V2 from panel b, magnetic field pressure $B^2/8\pi$ measured by the V2 magnetometer, and plasma thermal proton pressure $Nk_B T_p$ (reprinted from Decker et al. 2015 with permission); the electron temperature is neglected because it is an order of magnitude smaller than T_p in the IHS (Richardson et al. 2008). N indicates the plasma density, and k_B is Boltzmann’s constant.

et al. 2011, Decker et al. 2012). Krimigis et al. (2011) combined the Cassini/INCA ENA imaging results and the in situ V1 ion spectrum to predict that V1 would cross the HP at 121 AU (see figure 2 in Krimigis et al. 2011). These observations presaged a period of surprising observations by V1 that were thought initially to correspond to a crossing of the HP with the discovery of a “particle boundary” (Stone et al. 2013, Webber & McDonald 2013). Because the magnetic field direction did not change significantly on crossing the boundary, the view that the HP was crossed was revised with the term heliocliff, introduced to distinguish the “particle” boundary from the HP. The boundary was thought to be the beginning of a transition layer ahead of the HP (Burlaga et al. 2013b, Krimigis et al. 2013, Stone et al. 2013, Webber & McDonald 2013). However, the fortuitous observation of Langmuir or plasma waves (Gurnett et al. 2013) established that the

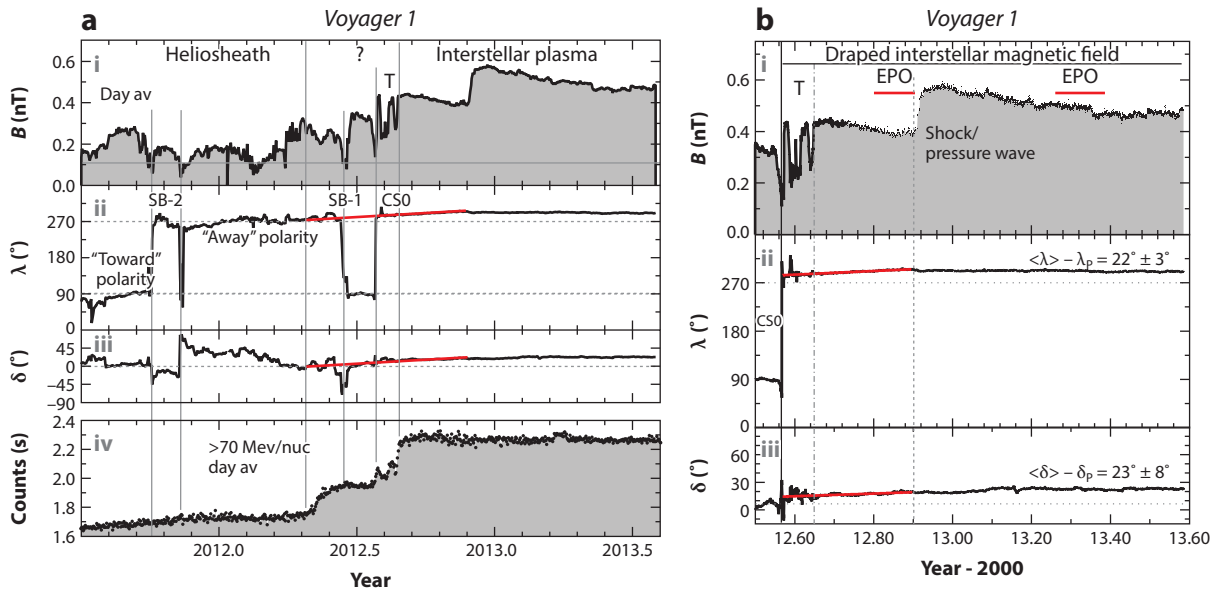


Figure 11

(a) The transition from the inner heliosheath to very local ISM, showing sector structure and magnetic fields: (i) the magnetic field strength, (ii) the azimuthal angle λ , (iii) the elevation angle δ , and (iv) the counting rate of >75 MeV nuc^{-1} cosmic rays. Reprinted from Burlaga & Ness (2014) with permission. (b) Interstellar magnetic fields following the crossing of a current sheet CS0, which may be the heliopause, by *Voyager 1*, showing detail over a shorter period: (i) the magnetic field strength, (ii) the azimuthal angle λ , and (iii) the elevation angle δ . A region containing both interstellar and heliosheath magnetic fields in flux tubes on interstellar magnetic field lines is labeled “T.” A high electron number density was observed during intervals indicated by the red horizontal lines. Reprinted from Burlaga et al. 2013a with permission. Abbreviation: EPO, electron plasma oscillation; SB, sector boundary.

plasma density after the heliocliff was comparable to that expected in the ISM. Although most researchers currently agree that the boundary was the HP and that V1 is now in the ISM (Burlaga et al. 2013b, Gurnett et al. 2013, Webber & McDonald 2013), this view is not universally shared. For example, Fisk & Gloeckler (2013, 2014) and Gloeckler & Fisk (2015) have suggested that V1 is still inside the HP.

The V1 magnetic field observations from 2011.5 to 2013.6 are shown in **Figure 11**. The magnetic field intensity exhibits a complex series of transitions. Prior to a current sheet (CS0) crossing, the IHS magnetic field was directed along the Parker spiral direction ($\lambda = 90^\circ$) pointing toward the Sun. Immediately after crossing CS0, V1 observed magnetic fields pointing away from the Sun ($\lambda = 270^\circ$). The difference in azimuthal angle increased following the crossing of CS0, reaching a plateau after ~ 2013.2 with a difference of $22^\circ \pm 3^\circ$. The difference in elevation angle is $23^\circ \pm 8^\circ$. The sustained difference between the observed magnetic field direction and the Parker spiral magnetic field direction and the absence of sectors following the CS0 crossing around 27 July 2012 and continuing to 2013.6 (shown in **Figure 11**) suggests that V1 was observing ISMFs throughout the interval (Burlaga et al. 2013a, 2014). The direction of the magnetic field is close to the $-T$ direction, i.e., west to east when looking from *Voyager* to the Sun.

As discussed above, the initial small difference between the ISMF direction and the heliosheath magnetic field direction observed by V1 was somewhat unexpected. However, simulations by Pogorelov et al. (2009a) predicted that the angle between the draped ISMF and the IHS fields should be $\delta \simeq 25^\circ$ and $\lambda \simeq 290^\circ$, i.e., a difference in azimuthal angle from the HP crossing to

the more distant ISM of $\simeq 20^\circ$, when angles are plotted instead of the components of \mathbf{B} . Burlaga & Ness (2014) concluded that the simulations of Pogorelov et al. (2009a) are consistent with the observations shown in **Figure 11**, within the uncertainties of the observations. The simulations of Borovikov & Pogorelov (2014) based on the exact fitting of the HP do not support the idea of Opher & Drake (2013) that the ISMF vector becomes nearly parallel to the solar equatorial plane regardless of its direction in the unperturbed LISM.

The magnitude $|\mathbf{B}|$ is larger in the ISM than that observed in the IHS before CS0, except in the region labeled T. In this region, Burlaga et al. (2013a) identified five boundaries at which the strength of B changed abruptly in association with changes in the energetic particles and cosmic rays (Krimigis et al. 2013, Stone et al. 2013). The magnetic field direction did not change significantly ($< 2^\circ$) across any of the five boundaries (Burlaga et al. 2013a). Burlaga & Ness (2014) suggested that the five boundaries separated interstellar magnetic flux tubes that alternately contained IHS plasma and VLISM plasma. Burlaga & Ness (2014) also suggested that IHS and VLISM magnetic field lines may have reconnected beyond the location of V1, allowing heliosheath plasma and energetic particles to be observed by V1 in region T. Various researchers have suggested magnetic reconnection of IHS and VLISM magnetic fields in region T in various configurations (Avinash et al. 2014, Strumik et al. 2013, Swisdak et al. 2013, Washimi et al. 2014) and including a form of flux transfer events (Schwadron & McComas 2013).

The observation by the V1 plasma wave instrument of electron plasma oscillations (EPOs) from 2013/99 to 2013/142 at a frequency of 2.6 kHz provided the most convincing evidence that V1 had crossed the HP (Gurnett et al. 2013). The plasma frequency corresponded to a very high electron number density of 0.08 cm^{-3} (see **Figure 11b**). An earlier EPO event at 2.2 kHz occurred in October–November 2012 (see **Figure 11b**) (Gurnett et al. 2013). The frequency spectra are illustrated in **Figure 12**. Because such densities are characteristic of interstellar plasma and are at least 50 times larger than expected for heliosheath plasma (Zank et al. 2013), it was concluded that V1 had entered the VLISM. However, the increase in density from 0.05 cm^{-3} to 0.08 cm^{-3} (**Figure 12**) may also describe an HP with a density ramp similar to that inferred from V1 radio wave observations (Gurnett et al. 1993): In this case, the radio waves (not plasma oscillations) were thought to be generated by a shock as it entered the interstellar plasma just beyond the HP. Simulations by Zank et al. (2013) showed that the HP is smoothed by interstellar neutral H and therefore possesses a gradient.

A large smooth jump in B on 2012/333 is evident in **Figure 11**, following the interval containing EPOs (2012 day 297 to 2012 day 332). The structure resembles a shock with $B_2/B_1 = 1.4$ (Burlaga et al. 2013b), with a small but significant change in λ . The structure is highly perpendicular with an obliquity of $\sim 85^\circ$, implying that the compression ratio is ~ 1.4 . An interstellar temperature of $20,000^\circ \text{ K}$ just beyond the HP, as suggested by the simulations of Zank et al. (2013), yields an upstream Alfvén speed of $V_{A1} = 38 \text{ km s}^{-1}$ and a sound speed of $V_{S1} = 17 \text{ km s}^{-1}$, which gives a magnetoacoustic speed of 40 km s^{-1} . Thus, if the structure is an interstellar shock, it was moving faster than 40 km s^{-1} , which is consistent with the speed of shocks transmitted through the HP (Zank & Müller 2003, Washimi et al. 2011). By analogy with shocks observed at 1 AU, Burlaga et al. (2013b) suggested that the observed interstellar shock is a subcritical, laminar, quasi-perpendicular shock (for a related discussion about shock classification in the context of PUIs, see Zank et al. 1996a). However, the shock seems to be much broader than those observed at 1 AU. Further theoretical studies are needed to understand the nature of such shocks, or pressure waves, in the magnetized PUI-mediated interstellar plasma.

On 28 July 2012, the intensity of protons from inside the heliosphere with energies $0.5 \leq E \leq 60 \text{ MeV}$ abruptly decreased and recovered 5 days later. A second decrease on 13 August 2012 lasted 8 days and was followed 4 days later by a permanent decrease on 25 August 2012. This

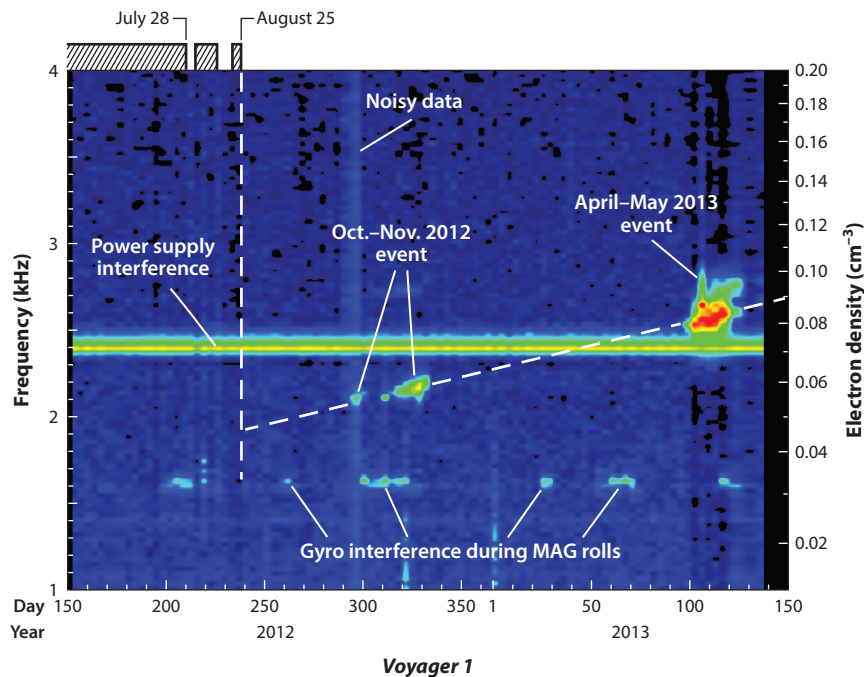


Figure 12

One-year composite of wideband plasma wave analyzers spectrograms showing a strong (April–May 2013) and a much weaker (October–November 2012) electron plasma oscillation event, corresponding to an electron density of 0.08 and 0.06 cm^{-3} , respectively. The dashed white line suggests an upward trend in the plasma frequency, hence plasma density, similar to the density ramp required to explain the upward-drifting 2–3-kHz heliospheric radio emissions observed prior to the crossing of the heliospheric termination shock. Adapted from Gurnett et al. (1993, 2013) with permission. Abbreviation: MAG, magnetometer.

was the first indication that V1 had entered the VLISM, although confirmation came much later as discussed above. Enhanced electron intensities are closely aligned with the five magnetic field boundaries in region T of **Figure 11**, whereas the heavier ions with larger gyroradii have broader intensity transitions. The abrupt depletion of ACRs is matched by an increase in the intensity of GCRs of the same energy.

As shown in **Figure 11a (iv)**, the HP transition occurs over a broad region that is especially evident in the two-step increase in the counting rate of cosmic rays $>70 \text{ MeV nuc}^{-1}$. The first step begins within an away sector in which **B** points toward the Sun along the Parker field direction, and it ends at the boundary of that sector. This step increase is followed by a brief plateau in the cosmic ray counting rate when V1 observed a short sector in which **B** points toward the Sun. The second step increase in the cosmic ray counting rate begins at the time V1 crosses CS0, and it ends when V1 crosses region T and enters the ISM (Burlaga & Ness 2014). The structure of the cosmic ray counting rate is not understood.

Swisdak et al. (2013) and Strumik et al. (2013) suggested that magnetic bubbles may exist in the region observed prior to the crossing of CS0, but Burlaga & Ness (2014) found no clear evidence for nested magnetic bubbles. Burlaga & Ness (2014) showed that the two preceding sector boundaries SB-2 and SB-1 are nearly parallel to CS0 and that the away polarity sector within these boundaries has an unusual jump in elevation angle δ extending from near 0° to almost 90° , declining to 0° prior to the onset of the first step increase in the cosmic ray counting rate. The magnetic field

strength varies within the sector between SB-1 and SB-2, and there are large dips in B at the sector boundaries as well as at the jump in δ between the boundaries. Such decreases in B are often observed at sector boundaries, but they are occasionally observed at structures called D-sheets (Burlaga 1968, Burlaga & Ness 1968), which are often associated with magnetic reconnection. This may indicate that some form of reconnection occurred, although not necessarily leading to the formation of magnetic bubbles (Avinash et al. 2014, Washimi et al. 2014).

The disappearance of most heliospheric ions after the HP crossing enabled observation of lower-energy GCRs than was previously possible (Webber & McDonald 2013). **Figure 13** shows

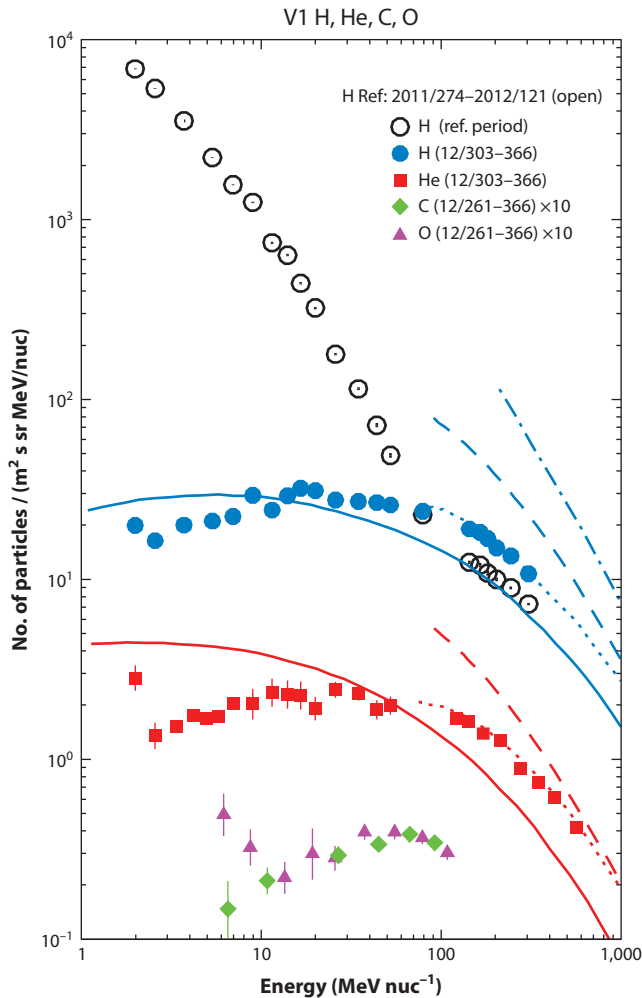


Figure 13

Differential energy spectra of H, He, C, and O from *Voyager 1* (V1). Two spectra are shown for H: one for a reference period 2011/274 to 2012/121 prior to the heliopause crossing; another for the period 2012/303 to 366 in the very local ISM. The C and O spectra are for the period 2012/261 to 366. Several model spectra for the local interstellar galactic cosmic ray H and He spectra are shown: (solid lines) model by Ip & Axford (1985), (dotted lines) leaky-box model of Webber & Higbie (2009), (dashed lines) diffusion-convection model of Moskalenko et al. (2002), and (dot-dash line) H from Fisk & Gloeckler (2012). Reprinted from Stone et al. (2013) with permission. Abbreviations: C, carbon; H, hydrogen; He, helium; O, oxygen.

the energy spectra for the period 2012/303 to 366 for H and He from 3 MeV to several hundred megaelectron volts per nucleon together with an energy spectrum of H from a period before the HP crossing (Stone et al. 2013). At energies below ~ 100 MeV nuc^{-1} during this time, the reference spectrum is dominated by TSPs. After the HP crossing, the TSPs were replaced by hitherto unobserved low-energy GCRs. Scherer et al. (2011), Herbst et al. (2012), and Strauss et al. (2013) have suggested that the adiabatic flow and/or bow wave/shock ahead of the HP may modulate the GCR intensity immediately outside the heliosphere, implying that the V1-measured low-energy GCR intensity may be lower than the galactic intensity. GCR H and He spectra have the same shape from ~ 3 to 346 MeV nuc^{-1} . The leaky-box model of Ip & Axford (1985) appears to possess approximately the right peak intensity for H, but the energy of the peak is lower than observed. This is interesting because, as noted by Ip & Axford (1985), the total cosmic ray pressure should be ~ 0.4 eV cm^{-3} , which implies that low-energy cosmic rays do not contribute significantly to the pressure balance at the boundary of the heliosphere. For He, both the predicted peak intensity and the energy of the peak are somewhat displaced from the observations. The leaky-box model spectra of Webber & Higbie (2009) are in good agreement with the observed H and He spectra for energies > 70 MeV nuc^{-1} .

We conclude this section with the V1 observations of fluctuating magnetic fields in the VLISM (Burlaga et al. 2014). The mean standard deviation of the transverse microscale components of the IHS and VLISM fluctuations is 0.005 nT, which is at the limit of measurement. The mean standard deviation for the compressive microscale fluctuating components in the IHS is 0.010 nT, which is 6% of the mean magnetic field. By contrast, for the compressive components of the fluctuations in the ISMF, the mean standard deviation is below instrument limits (< 0.005 nT) and $< 1\%$ of the mean magnetic field. The microscale magnetic field fluctuations are distinctly different than those in the IHS. The compressive component and the transverse components of the ISMF fluctuations are very small compared with the mean magnetic field (0.48 nT). The observed quiescent VLISM magnetic field fluctuations have important implications for theories that explain the IBEX ribbon. Interpreting the V1 magnetic field data as the upper limit on magnetic fluctuations in the VLISM is compatible with estimates of the ISM turbulence intensity. Certainly, the rapid disappearance and large anisotropies of ACRs past the “helioclip” suggest that the scattering rates in the VLISM must be extremely low, consistent with the picture of very weak turbulence that emerges from the data presented by Burlaga et al. (2014).

2.2. Global Observations: IBEX Measurements

The IBEX uses measurements of ENAs (McComas et al. 2009b) to image the interaction of the heliosphere with the VLSIM. IBEX measures ENAs in eight energy bins from ~ 0.1 to 2 keV with IBEX-Lo (Fuselier et al. 2009b) and five energy bins from ~ 0.5 to 5 keV with IBEX-Hi (Funsten et al. 2009a). The data are collected into sets of all-sky maps every 6 months. Excellent summaries of the first 5 years of the IBEX operations and results can be found in McComas et al. (2012b; 2014a,b).

Illustrated in **Figure 14** are sky maps for the five IBEX-Hi energy steps, produced by combining all 10 maps produced in IBEX’s first 5 years of observations (McComas et al. 2014b). These sky maps currently represent the “best” average ENA flux measurements observed at ~ 1 AU, in the heliospheric reference frame, and the IBEX data have been corrected in both energy and angle for the Compton-Getting effect (McComas et al. 2010, 2012b). The most unexpected of all of the IBEX discoveries was that of the ribbon (illustrated in **Figure 14**), which was completely unanticipated by all theories and models. The ribbon is a narrow ($\sim 20^\circ$ wide from 0.7 to 2.7 keV) (Fuselier et al. 2009a), clearly defined enhancement in ENA flux, up to approximately two to

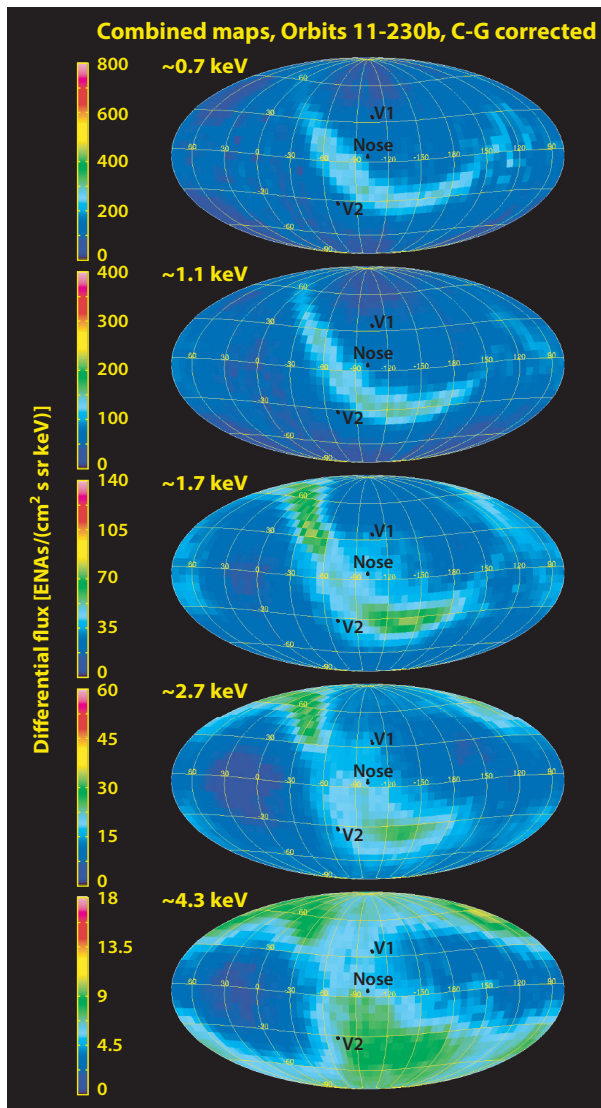


Figure 14

ENA fluxes from combined maps 1–10 in the heliospheric reference frame. Points indicate locations in the sky maps of the direction of interstellar inflow (*center*) and *Voyager 1* (V1) and *Voyager 2* (V2). The Interstellar Boundary Explorer sky maps are plotted using a Mollweide projection in ecliptic coordinates, with the differential ENA flux shown in false color in units of $(\text{cm}^2 \text{ s sr keV})^{-1}$. Reprinted from McComas et al. (2014a) with permission. Abbreviations: C-G, Compton-Getting; ENA, energetic neutral atom.

three times that of the surrounding globally distributed flux (McComas et al. 2009a), is extremely circular (Funsten et al. 2009b, 2013), and appears to be ordered by the external magnetic field in the VLISM (McComas et al. 2009a, Schwadron et al. 2009). The dominant energies of the ribbon ENAs as a function of ecliptic latitude very closely follow the latitude-dependent energy distribution of the out-flowing SW over the past, protracted solar minimum (McComas et al. 2012b, 2013), suggesting that the source of the ribbon is related to the supersonic SW. A bright

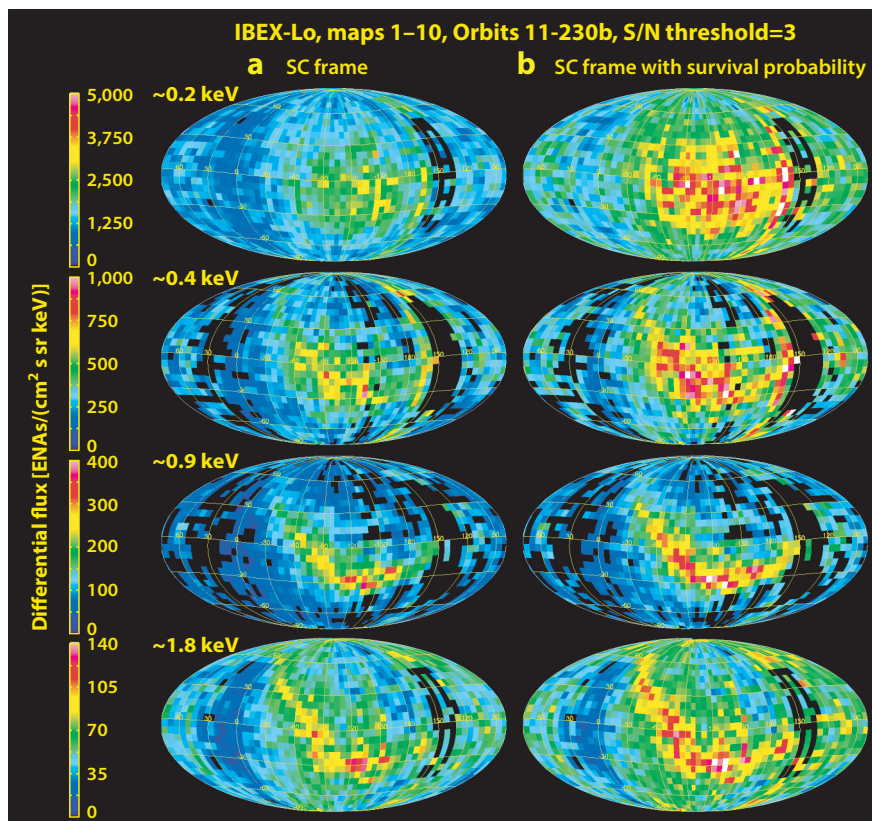


Figure 15

IBEX-Lo maps combining 5 years of observations in the spacecraft frame: (a) uncorrected and (b) corrected for survival probability. From top to bottom, the energy pass bands are centered around 0.2, 0.4, 0.8, and 1.8 keV. Pixels with a signal-to-noise ratio <3 have been suppressed (black). Reprinted from McComas et al. (2014a) with permission. Abbreviations: IBEX, Interstellar Boundary Explorer; SC, spacecraft; S/N, signal to noise.

region of higher energy ENAs in the northern portion of the ribbon (Funsten et al. 2009b, McComas et al. 2009a) is also present and has been called the “knot.”

IBEX-Lo maps from all 5 years for energies from ~0.2 to 1.8 keV are shown in **Figure 15**: The figure includes corrections for the survival probability of outer heliospheric ENAs reaching 1 AU. Although the IBEX-Lo data have lower statistical significance than those of IBEX-Hi, the two higher-energy maps provide independent observations that validate the IBEX-Hi observations of the ribbon at these overlapping energies (McComas et al. 2009a). At the two lower energies, IBEX-Lo provides the only measurements of heliospheric ENAs. The ribbon does not appear to extend to the lowest energies (~0.2 keV).

The large-scale structure of the ribbon has remained generally stable, but ENA fluxes from both the ribbon and the global background have decreased since the first observations in 2009 (McComas et al. 2012b). The decrease is observed at all energies and in all regions except the heliotail direction, but it is largest in the ribbon and most pronounced at 1.1 keV. The SW mass, momentum, and energy flux show a similar decline over similar periods, indicating a correlation with the steady decline in SW dynamic pressure observed at 1 AU during the unusually long and

deep solar minimum between solar cycles 23 and 24 (McComas et al. 2013). The transport time for ENAs would imply a shift in the temporal response of the ribbon and knot (McComas et al. 2010) to changing SW conditions. Variability in the polar regions, unrelated to the ribbon, which does not cross the poles, has been found on 6- to 12-month scales (Reisenfeld et al. 2012). The IBEX ribbon is visible in spectral maps, with a spectral index of $\sim 2-2.5$, which is somewhat greater than those observed in surrounding regions that typically have spectral indexes ≤ 2 . Spectral slopes at all latitudes have indexes typically no greater than ~ 1.5 (Livadiotis & McComas 2013). Many of the IBEX energy spectra, especially those at high latitudes, are not well fit by a single power law distribution and tend to possess spectral structure (McComas et al. 2009a; Dayeh et al. 2012; Desai et al. 2012, 2014).

Away from the nose, the spectral index shows larger values, typically > 2.5 , in two broad regions at low to mid latitudes. At least one of these features is associated with the possible discovery of the heliotail (Schwadron et al. 2011). McComas et al. (2013) associated these two regions with the port and starboard “lobes” of a large heliotail structure that is centered in nearly the downwind direction. Virtually no detailed modeling has addressed the IBEX ENA observations that may be related to the structure and heliotail, and the relationship of the lobes to the ISMF.

Regarding IBEX observations, at least one interpretation of the data has elicited considerable controversy. Interstellar He atoms, unlike H, experience very little charge exchange with SW ions; therefore, the He flow velocity vector is the best indicator of the actual relative motion between the Sun and LISM. The precise direction of the He flow serves as a reference for measurements of other species, and inferred differences can be used to derive the detailed coupling between the interstellar and solar plasmas (e.g., Izmodenov et al. 1999, Lallement et al. 2005). As such, the He flow parameters can be used to estimate the pristine LISM plasma and neutral H parameters (McComas et al. 2012a). However, the inferred IBEX He direction and velocity (Bzowski et al. 2012, Möbius et al. 2012) are different from earlier estimates of the He flow derived from optical measurements of the He 58.4-nm resonance line or from Gas/Ulysses (Witte 2004, Katushkina et al. 2014) in situ measurements. Frisch et al. (2013) interpreted the different He velocity and directions as a temporal variation of the interstellar wind direction, an interpretation that has been challenged vigorously (Lallement & Bertaux 2014). Given the large collisional mfp ($\sim 1,000$ AU) for VLISM He-proton or He-He scattering, it is difficult to account for He flow variations on decade-long timescales.

Kubiak et al. (2014) presented IBEX 2010 observations of the full He signal that appear to be a superposition of pristine neutral interstellar He gas and an additional population of neutral He that they call the “Warm Breeze.” The Warm Breeze is approximately two times slower and 2.5 times warmer than the primary interstellar He population, its density upwind of the heliosphere is $\sim 7\%$ that of interstellar He, and the inflow direction differs by $\sim 19^\circ$ from the inflow direction of interstellar gas. Despite the earlier assumptions that He was relatively unaffected by the heliospheric boundaries, understanding He (and the behavior of other heavy interstellar atoms) is becoming one of the more challenging modeling problems in understanding the heliospheric-LISM interaction.

3. MODELING THE SOLAR WIND-LOCAL INTERSTELLAR MEDIUM INTERACTION

Extensive reviews of the modeling of the interaction of the heliosphere with the LISM provide far more detail about the current status than can be presented here (see, e.g., Zank 1999a, Izmodenov et al. 2009, Zank et al. 2009). Instead, we focus on a few basic aspects.

3.1. Modeling Neutral Hydrogen

Interstellar neutral gas, primarily H, is coupled via charge exchange to the SW and VLISM plasma. Interstellar neutral gas flows into the heliosphere relatively unimpeded and can penetrate to within several astronomical units of the Sun. He and other heavy elements have little dynamical influence on the SW-LISM interaction but provide important direct information about LISM conditions (Möbius et al. 2004, 2012; Witte 2004; Bzowski et al. 2012), such as the interstellar flow speed, direction, and temperature.

Although several interactions among H atoms, protons, and electrons are possible (Zank 1999a), we mainly consider charge exchange. The distribution of neutral H, both LISM and heliospheric, may be calculated directly from the Boltzmann equation:

$$\frac{\partial f_H}{\partial t} + \mathbf{v} \cdot \nabla f_H + \left(\frac{\mathbf{F}}{m} \cdot \nabla_{\mathbf{v}} \right) f_H = -f_H \int f_p(\mathbf{x}, \mathbf{v}_p, t) V_{rel,p} \sigma_{ex}(V_{rel,p}) d^3 \mathbf{v}_p + f_p(\mathbf{x}, \mathbf{v}, t) \int f_H(\mathbf{x}, \mathbf{v}_H, t) V_{rel,H} \sigma_{ex}(V_{rel,H}) d^3 \mathbf{v}_H, \quad (1)$$

where $f_H(\mathbf{x}, \mathbf{v}, t)$ and $f_p(\mathbf{x}, \mathbf{v}, t)$ are the neutral H and plasma particle distribution functions, respectively, expressed in terms of position \mathbf{x} , velocity \mathbf{v} , and time t . \mathbf{F} is the force acting on a particle of mass m , typically gravity and radiation pressure. The right-hand-side terms describe the production and loss of particles at $(\mathbf{x}, \mathbf{v}, t)$. Because the partially ionized LISM is assumed to be equilibrated, the boundary data at “infinity” is considered a Maxwellian distribution parameterized by the bulk LISM density, velocity, and temperature.

The mfp for charge-exchange collisions can be very large in the heliospheric boundary regions and in the supersonic SW. Thus, ideally, the interstellar neutral distribution should be calculated kinetically because the Knudsen number $Kn \simeq 1$ for neutral H throughout large regions of the heliosphere. Otherwise, it is necessary to recognize that a single set of gas dynamical equations cannot adequately describe the different neutral H populations created through charge exchange. A multiple set of gas dynamics equations corresponding to various neutral particle populations that are created in different thermodynamical regions of the heliosphere and LISM can be a good approximation to the fully kinetic description, subject to certain caveats (Zank et al. 2001, Heerikhuisen et al. 2006, Müller et al. 2008). The multifluid description gives rise to very tight, accurate coupling, so that both steady-state problems and fully dynamic problems can be solved (Zank & Müller 2003, Florinski et al. 2005, Borovikov et al. 2008, Borovikov & Pogorelov 2014). A kinetic treatment of neutral H (Baranov & Malama 1993; Izmodenov et al. 1999, 2005; Müller et al. 2000; Heerikhuisen et al. 2006; Izmodenov & Alexashov 2006) returns the complete distribution function for an assumed plasma distribution function.

The three or four thermodynamically distinct boundary regions act as a source of neutral H atoms whose distribution reflects that of the plasma distribution in the region. This is illustrated by an example of a reduced neutral H distribution function derived from a three-dimensional (3D) MHD-kinetic H model (**Figure 16**) that shows a radial velocity distribution function at 300 AU for three LISM models (Zank et al. 2013). The one-dimensional (1D) distribution functions very nicely illustrate the basic physics of the heliosphere-LISM interaction. Overplotted on **Figure 16** is the assumed neutral H Maxwellian distribution at 1,000 AU. Because the LISM plasma has been heated by secondary charge exchange, the neutral H core distribution is broadened. The hot neutrals created in the IHS form an extended tail to the original Maxwellian-like core from $\sim 70 \text{ km s}^{-1}$ to $\sim 300 \text{ km s}^{-1}$. The fast neutrals created by charge exchange with the supersonic SW manifest themselves as the broad bump at the fast end of the distribution, from $\sim 300 \text{ km s}^{-1}$ to $\sim 470 \text{ km s}^{-1}$.

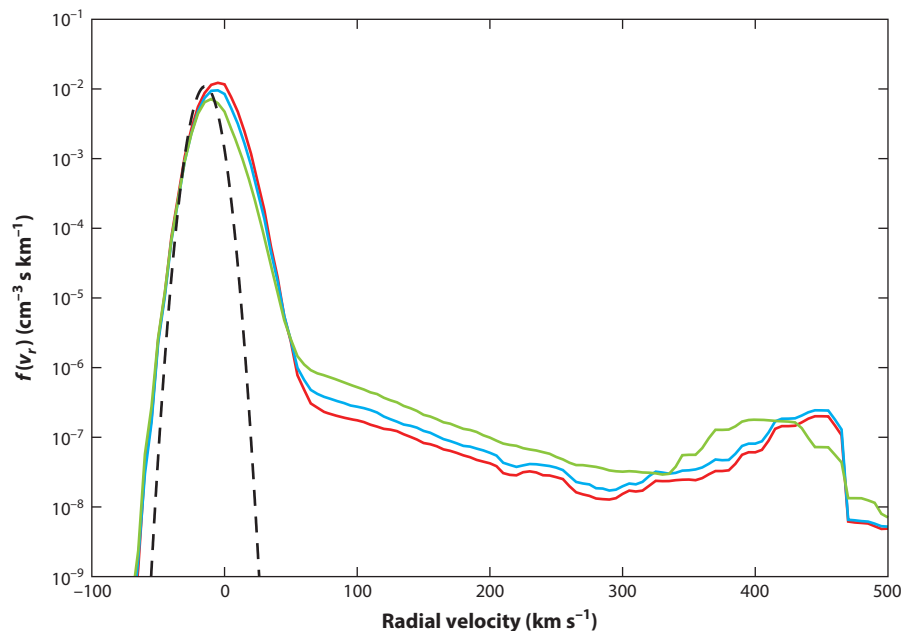


Figure 16

One-dimensional radial velocity distribution function for neutral hydrogen (H) at 300 AU along the α -Cen sightline: reduced distribution functions for a heliosphere–local ISM interaction with (*red curve*) a bow shock, (*blue curve*) a smooth bow wavelike transition, and (*green curve*) no bow shock. The black dashed line corresponds to the Maxwellian distribution assumed at 1,000 AU as the boundary condition distribution for a kinetic neutral H model. The distribution functions for all three cases are very similar. Reprinted from Zank et al. (2013) with permission.

3.2. The Plasma Description

The most detailed current models of the supersonic SW, IHS, VLISM, and, indeed, the ISM as a whole use an MHD fluid to describe the plasma and a neutral gas to describe neutral H. Observations by V1, V2, IBEX, and Cassini INCA are beginning to reveal that the VLISM is a much more complicated plasma than can be described by simple MHD models. Instead, the VLISM is a multicomponent, nonequibrated plasma, as determined from equilibration timescales (Zank et al. 2014).

3.2.1. Multifluid model. In deriving a multifluid model that includes PUIs and ACRs self-consistently, Zank et al. (2014) assumed that the distribution functions for the background thermal protons and electrons are each Maxwellian, which ensures the absence of any heat flux or stress tensor terms for the thermal plasma. PUIs initially form an unstable distribution that excites Alfvénic fluctuations. The self-generated fluctuations and in situ turbulence serve to scatter PUIs in pitch angle. The PUIs are governed by the Fokker-Planck transport equation with a collisional term, which, for simplicity, Zank et al. (2014) assumed is an isotropic pitch-angle μ scattering operator. The transport equation has to be transformed into a frame that ensures there is no change in PUI momentum and energy due to scattering. By taking moments, we can derive the evolution equations for the macroscopic PUI variables. The zeroth moment yields the continuity equation for PUIs, and the first moment provides the conservation of momentum equation with

an undefined pressure tensor. To close the momentum equation, Zank et al. (2014) evaluated the PUI distribution function f by solving the PUI transport equation. In doing so, Zank et al. (2014) assumed (a) the PUI distribution is gyrotropic and (b) scattering of PUIs is sufficiently rapid to ensure that the PUI distribution is nearly isotropic. The PUI collisionless pressure tensor may then be expressed as the sum of an isotropic scalar pressure P_p and the stress tensor (Zank et al. 2014). The stress tensor is a generalization of the “classical” form but for a collisionless charged gas of PUIs experiencing pitch-angle scattering by turbulent magnetic fluctuations.

The collisionless PUI heat flux $\mathbf{q}(\mathbf{x}, t)$ can be expressed as

$$q_i(\mathbf{x}, t) = -\frac{2\pi}{3} \int c'^2 \kappa_{ij} \frac{\partial f_0}{\partial x_j} c'^2 dc' = -\frac{1}{2} K_{ij} \frac{\partial P_p}{\partial x_j}, \quad (2)$$

where the spatial diffusion coefficient κ_{ij} is introduced together with a PUI speed-averaged form K_{ij} . The collisionless heat flux for PUIs is therefore described in terms of the PUI pressure gradient, and consequently, the averaged spatial diffusion introduces a PUI diffusion time and length scale into the multifluid system. The transport equation for the PUI pressure is

$$\frac{\partial P_p}{\partial t} + \mathbf{U}_p \cdot \nabla P_p + \frac{5}{3} P_p \nabla \cdot \mathbf{U}_p = \frac{1}{3} (\nabla \cdot \mathbf{K} \cdot \nabla P_p), \quad (3)$$

where \mathbf{U}_p is the PUI bulk velocity (Zank et al. 2014). Equation 3 illustrates that the PUI heat flux yields a spatial diffusion term in the PUI equation of state. The PUI system of equations is properly closed and correct to the second order.

The corresponding set of ACR equations is derived in almost identical fashion. These equations, together with Maxwell’s equations, describe the full thermal electron-thermal proton-PUI-ACR multifluid system (Zank et al. 2014) and are substantially different from the usual multifluid equations based on a Maxwellian closure as well as the MHD description. The full set of multifluid equations is given by Zank et al. (2014).

3.2.2. Single-fluidlike reduction. For some problems, the full multifluid model is far too complicated to solve. By making the key assumption that $\mathbf{U}_p \simeq \mathbf{u}_s$ (and $\mathbf{U}_A \simeq \mathbf{u}_s$, the ACR bulk flow speed; \mathbf{u}_s , the thermal proton velocity), Zank et al. (2014) reduced the multifluid plasma system to an MHD-like set of model equations. The assumption that $\mathbf{U}_p \simeq \mathbf{u}_s$ is reasonable because (a) the bulk flow velocity of a plasma is always dominated by the protons and (b) the pick-up process forces newly created PUIs to comove with the background plasma flow. Because the PUIs and ACRs are not thermally equilibrated with the background plasma ($T_e \neq T_p \neq T_A$), we need to distinguish the P_s , P_p , and ACR pressure P_A equations. Upon defining appropriate macroscopic variables, and exploiting the smallness of the mass ratio $m_e/m_p \ll 1$, Zank et al. (2014) combined the thermal proton and electron equations as a single thermal plasma pressure equation and obtained a reduced single-fluid set of model equations:

$$\frac{\partial \rho}{\partial t} + \nabla \cdot (\rho \mathbf{U}) = 0, \quad (4)$$

$$\rho \left(\frac{\partial \mathbf{U}}{\partial t} + \mathbf{U} \cdot \nabla \mathbf{U} \right) = -\nabla (P + P_p + P_A) + \mathbf{J} \times \mathbf{B} - \nabla \cdot \mathbf{\Pi}, \quad (5)$$

$$\frac{\partial P}{\partial t} + \mathbf{U} \cdot \nabla P + \gamma P \nabla \cdot \mathbf{U} = 0, \quad (6)$$

$$\frac{\partial P_p}{\partial t} + \mathbf{U} \cdot \nabla P_p + \gamma_p P_p \nabla \cdot \mathbf{U} = \frac{1}{3} \nabla \cdot (\mathbf{K}_p \cdot \nabla P_p), \quad (7)$$

$$\frac{\partial P_A}{\partial t} + \mathbf{U} \cdot \nabla P_A + \gamma_A P_A \nabla \cdot \mathbf{U} = \frac{1}{3} \nabla \cdot (\mathbf{K}_A \cdot \nabla P_A), \quad (8)$$

$$\mathbf{E} = -\mathbf{U} \times \mathbf{B}, \quad \frac{\partial \mathbf{B}}{\partial t} = -\nabla \times \mathbf{E}, \quad \mu_0 \mathbf{J} = \nabla \times \mathbf{B}, \quad \nabla \cdot \mathbf{B} = 0, \quad (9)$$

where ρ denotes the total density, \mathbf{U} the bulk flow velocity, γ the appropriate adiabatic index, Π the stress tensor, \mathbf{J} the current density, and \mathbf{B} and \mathbf{E} the magnetic and electric fields, respectively. The single-fluid description (Equations 4–9) (Zank et al. 2014) differs from the standard MHD model in that separate equations for the PUI and ACR pressure (Equations 7 and 8) are required. The PUIs and ACRs introduce distinct collisionless heat conduction and viscosity terms into the system, which in turn introduces length scales into the system that are absent in MHD.

3.2.3. The magnetohydrodynamic model. To recover the standard form of the MHD equations used in all models to describe the interaction of the SW with the LISM, we set the heat conduction spatial diffusion tensor $\mathbf{K} = 0$ in the system of Equations 4–9 and introduce the total thermodynamic pressure $P_{\text{total}} = P + P_p$. This then yields the standard MHD model, with source terms to describe charge exchange with neutral H (dropping the subscript “total” on P_{total}):

$$\frac{\partial \rho}{\partial t} + \nabla \cdot \rho \mathbf{U} = Q_\rho, \quad (10)$$

$$\rho \frac{\partial \mathbf{U}}{\partial t} + \rho \mathbf{U} \cdot \nabla \mathbf{U} + (\gamma - 1) \nabla e + (\nabla \times \mathbf{B}) \times \mathbf{B} = \mathbf{Q}_m, \quad (11)$$

$$\frac{\partial}{\partial t} \left(\frac{1}{2} \rho U^2 + e + \frac{B^2}{8\pi} \right) + \nabla \cdot \left[\left(\frac{1}{2} \rho U^2 + \gamma e \right) \mathbf{U} + \frac{1}{4\pi} \mathbf{B} \times (\mathbf{U} \times \mathbf{B}) \right] = Q_e, \quad (12)$$

$$\frac{\partial \mathbf{B}}{\partial t} - \nabla \times (\mathbf{U} \times \mathbf{B}) = 0, \quad \nabla \cdot \mathbf{B} = 0, \quad (13)$$

and equation of state $e = \alpha n k_B T / (\gamma - 1) = P / (\gamma - 1)$. The choice of $\alpha = 2$ (or greater if indirectly incorporating the contribution of cosmic rays and dust) corresponds to a plasma population comprising electrons and protons. The source terms Q_ρ , \mathbf{Q}_m , and Q_e serve to couple the neutral H and proton populations. Certain other subtleties in the formulation of an MHD model in the presence of neutral H need to be recognized (see Florinski & Zank 2003) in the context of nonideal MHD. Subject even to the assumption of an isotropic SW, the formulation (Equations 10–13) is inherently 3D thanks to the solar magnetic field and the current sheet. Representative recent papers from different groups that use this system with various treatments of the neutral H gas include Grygorczuk et al. (2011), Heerikhuisen et al. (2014), Izmodenov et al. (2009), Opher (2012), Pogorelov et al. (2009a), Ratkiewicz et al. (2008), Washimi et al. (2011), and Zank et al. (2013).

In the above, by setting $\mathbf{K} = 0$, we have implicitly assumed that the PUIs are fully coupled to the thermal plasma. If, however, $\mathbf{K} \neq 0$, then PUIs introduce a form of heat conduction into the system and the PUI coupling to the background thermal plasma and their pressure contribution is not as large. Fisk & Gloeckler (2014) have emphasized this point, although not formulated as above.

Although PUIs have been assumed into the MHD description by setting $\mathbf{K} = 0$, the expected superposition of the thermal proton and PUI distributions can be approximately incorporated in the MHD description (Equations 10–13), provided the effects of heat conduction and the stress tensor are neglected. Heerikhuisen et al. (2008) and Prested et al. (2008) suggested a simple way

to incorporate a PUI population as part of a single distribution: Assume a generalized Lorentzian, or κ , distribution (see, e.g., Heerikhuisen et al. 2008, Livadiotis & McComas 2009). The κ distribution function possesses a Maxwellian core as well as a power law tail that scales as $v^{-2(\kappa+1)}$ and reduces to a Maxwellian in the limit of large κ . Although the core and tail features agree qualitatively with observations, a limitation of the κ formalism is that it does not allow for the relative abundances of core and tail to be adjusted for a particular choice of κ . Obviously, the observed flat-topped PUI population is absent in the κ approximation.

The MHD equations for the plasma do not change if a κ distribution for the protons is assumed. Closure at the second moment is possible because the distribution is isotropic. Thus, the heat flux and the off-diagonal components of the stress tensor are identically zero. The only difference from conventional fluid dynamics is that the collision integrals do not vanish as they would for a Maxwellian distribution. However, collisional frequencies are so low for the SW that these collisional terms may be neglected and the distribution function treated as “frozen” into the plasma. Even though the SW is effectively collisionless, an MHD approach remains warranted because the plasma has fluid properties perpendicular to the magnetic field while various wave phenomena help isotropize the distribution. For these reasons, Heerikhuisen et al. (2008) solved the regular MHD equations to determine the bulk plasma quantities, but in the IHS, they interpreted the bulk plasma quantities as having come from a κ distribution. Heerikhuisen et al. (2008) assumed $\kappa = 1.63$ for the SW plasma, consistent with LECP observations (Decker et al. 2005). It has been necessary to assume a κ distribution to match the intensities of the ENA observations made by the IBEX mission (Heerikhuisen et al. 2010, 2014; Zirnstein et al. 2014). The inclusion of the PUI pressure through a κ distribution, as compared with a Maxwellian distribution, also modifies the locations of the TS, HP, and BS. However, as discussed above, the “slippage” of the PUIs as expressed through heat conduction and the stress tensor means that the coupling of PUIs and thermal plasma will not be as strong as suggested by the κ -distribution approach.

3.3. Modeling the Large-Scale Heliospheric–Local Interstellar Medium Interaction

A lengthy discussion of the possible different ISMF and IMF configurations and their impact on determining the global heliospheric topology is given by Pogorelov et al. (2004) and Zank et al. (2009). Here we focus on recent simulations that summarize much of our recent understanding of the large-scale heliosphere. The most important aspect that has emerged in the past decade is that MHD-only models that neglect the backreaction of neutrals at either a multifluid or kinetic level cannot adequately describe global heliospheric structure; thus, MHD-only models are an incorrect formulation. In particular, for both gas dynamic and MHD models, the HTS or HP heliocentric distance can be 1.5 times or more larger when neutral H is neglected, even for identical SW and LISM conditions (Pauls et al. 1995, Zank 1999a).

IMFs and ISMFs are important for determining the global structure of the heliospheric boundaries. ISMF strength and orientation affect the shape and position of the HP relative to the Sun and interstellar plasma velocity vector, originally discussed by Fahr et al. (1988), Linde et al. (1998), Pogorelov & Matsuda (1998), and Ratkiewicz et al. (1998). The IMF, by virtue of the current sheet, introduces a corresponding asymmetry inside the IHS that affects the shape and position of the HP (Washimi & Tanaka 1996, Linde et al. 1998, Zank 1999a). The asymmetry in the HP position affects the shape of the HTS, and the different distances at which the V1 and V2 HTS crossings occurred suggest an asymmetry in the global HTS location (Stone et al. 2008). Using SOHO (Solar & Heliospheric Observatory) and interplanetary glow observations, Lallement et al. (2005) found a north-south (NS) asymmetric H gas flow in the region between the HP and the

outer BS/wave. They argued that this asymmetry was caused by charge-exchange collisions of neutral particles with protons whose averaged orientation was controlled by the local ISMF and concluded that the magnetic field should be aligned with the so-called hydrogen deflection plane (HDP), forming an oblique angle to the LISM flow direction. Analysis of the source location of the kilometric radio emissions observed at V1 and V2 (Gurnett & Kurth 2008) also suggested a similar obliquely oriented ISMF. As shown by Pogorelov et al. (2008, 2009a,b), the orientation of the B - V plane containing the unperturbed ISMF and LISM velocity vectors and the constraint to fit the IBEX ribbon allow the orientation and strength of the ISMF to be reasonably well determined.

Using an ideal steady 3D MHD-only simulation with an obliquely oriented ISMF lying in the HDP, Opher et al. (2006) found a large NS HTS asymmetry. This simulation neglected the self-consistent inclusion of neutral interstellar H. However, using a 3D MHD simulation that included the effects of neutral particles, Pogorelov et al. (2007) found that the asymmetry is significantly reduced when neutral H is coupled to the plasma.

Using ideal MHD and neutral multifluid formulations in a series of papers, Pogorelov et al. (2004, 2006, 2009a, 2012, 2013) and Borovikov & Pogorelov (2014) considered the fully 3D MHD interaction of the heliosphere with the LISM. Pogorelov et al. (2009a, 2012, 2013) and Borovikov & Pogorelov (2014) included the 11-year solar cycle and 25-day rotation period of the Sun and also included momentum and energy transfer between the ionized and neutral components. They assumed that the ISMF vector belongs to the HDP (Lallement et al. 2005), which is inclined at an angle of $\sim 60^\circ$ toward the ecliptic plane of the Sun. The latitudinal extent of the boundary between the slow and fast SW regions, as well as the angle between the Sun's rotation and magnetic-dipole axes, are assumed to be periodic functions of time, whereas the polarity of the IMF changes sign every 11 years at the solar maximum. This work yielded a number of important results, predicting many phenomena subsequently observed by V1 and V2. Pogorelov et al. (2009a) and Borovikov & Pogorelov (2014) found that δ increases to $\sim 35^\circ$ across the HP and continues increasing to $\sim 42^\circ$ and that λ increases to $\sim 285^\circ$. These values are both qualitatively and quantitatively in reasonable accord with V1 observations (Burlaga & Ness 2014).

The behavior of the HCS behind the HTS was investigated by Pogorelov et al. (2009a). The HCS exhibits the well-known wavy structure (Ness & Wilcox 1965, Jokipii & Thomas 1981). The "peak-to-peak" separation distance decreases behind the shock, becoming ~ 1 AU. Compared with the latitudinal extent in the supersonic SW, that of the HCS is also inhibited beyond the HTS. Time-dependent simulations also show that the magnetic flux is not conserved in the IHS, both because the longitudinal velocity component is comparable with the radial component, as observed by V1, and because of velocities related to the temporal HCS (Pogorelov et al. 2012).

Before V2 crossed the HTS, the temporal density and speed of the supersonic SW plasma was highly variable with many shock waves present in the outer heliosphere. This suggests rapid and large-amplitude time-varying changes in the HTS position. Thus, one possible explanation for the apparent NS asymmetry of the HTS is temporal variability of the SW (Washimi et al. 2007; Zank et al. 2009; Pogorelov et al. 2009a, 2011, 2012). Using a 3D MHD-neutral model similar to that of Pogorelov et al. (2009a), Washimi et al. (2011) developed a temporal model that simultaneously satisfies both V1- and V2-observed crossing times and locations of the HTS. Daily values of SW speed and density observed by V2 were used at every simulation step to reproduce short-term dynamical effects. The temporal HTS positions R_{TS} along both the Sun-V1 and the Sun-V2 lines are shown in **Figure 17**. The amplitude of the HTS excursions can be as much as 12–13 AU. Washimi et al. (2011) compared their simulation with observations of TSPs. The TSP (0.5–0.7 MeV proton) intensity at V2 (Stone et al. 2008) was first observed as V2 approached the HTS in late 2004. At that time, the simulated HTS is moving toward V2 and is within 11 AU. After

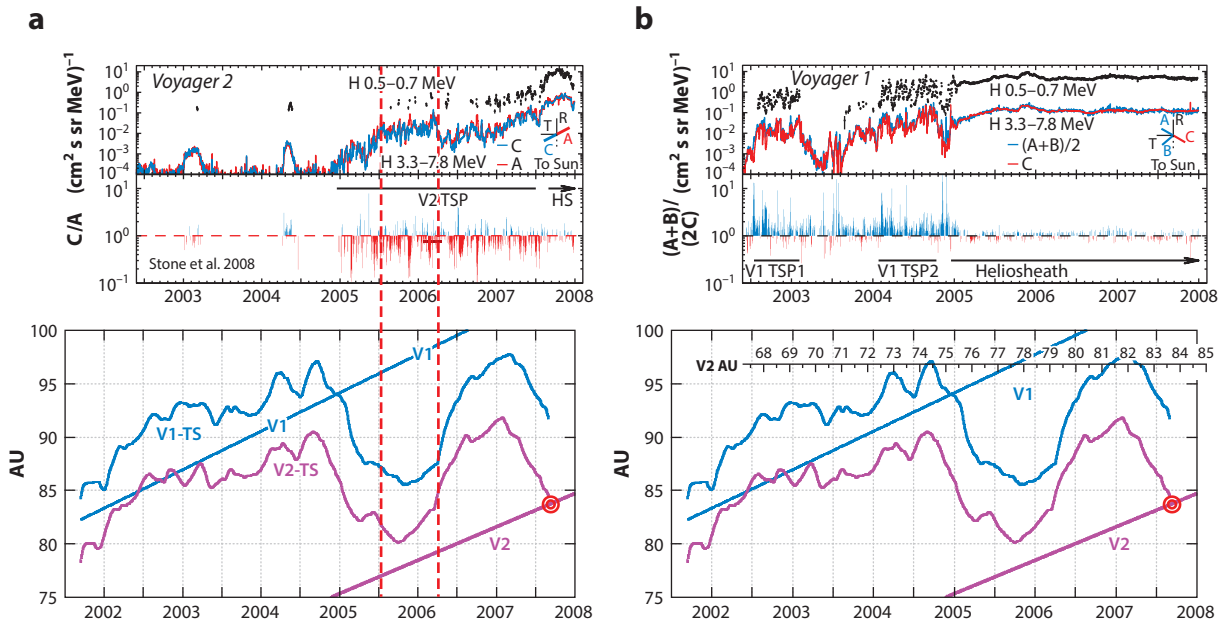


Figure 17

Comparison of the computed heliospheric termination shock position and the observations of 0.5- to 0.7-MeV proton intensities (Stone et al. 2008) along the (a) Sun-V2 and (b) Sun-V1 lines. The two vertical dotted red lines denote the period when the proton intensity was a maximum 1.5 years prior to the V2 crossing time. Reprinted from Washimi et al. (2011) with permission. Abbreviations: TS, termination shock; TSP, termination shock particle; V1, *Voyager 1*; V2, *Voyager 2*.

the first observations of TSPs by V2 in late 2004, the intensity continued to increase as the distance between V2 and the TS continued to decrease (**Figure 17**) until their separation was no more than 3 AU in late 2005. The reduction in HTS distance was probably due to an overshoot driven by a returning magnetosonic pulse (below). After this, the distance to the HTS began to increase again, as it was driven rapidly outward by a collision with the 2006 March interplanetary shock (Richardson et al. 2006). The high-intensity period of the TSP observations during 2005.5–2006.2 (see **Figure 17**) therefore corresponds to when V2 was continuously approaching the HTS, to within 3 AU. The observed TSP events appear to be consistent with the temporal HTS position profile.

The space-time plots of **Figure 18** depict physical quantities for the period 2001 September 10 to late 2009 along the Sun-V2 line (Washimi et al. 2011). The highly variable shock location R_{TS} is clearly identified by the abrupt changes in all physical quantities at 75–92 AU (V2). The HTS position moves out radially after a SW high-ram-pressure structure collision. Large-amplitude pulses in the ram pressure, thermal pressure, temperature, density, and magnetic pressure are generated downstream of the HTS (Story & Zank 1997, Zank & Müller 2003, Washimi et al. 2007), and each pulse propagates into the IHS. The speed of the pulse in the heliosheath near the HTS is almost the same as that of the ram-pressure pulse in interplanetary space. Because the speed of these pulses is almost equal to the magnetosonic speed, they may be identified as magnetosonic pulses (Story & Zank 1997). These pulses are partially reflected near the HP, back toward the TS, with which they then collide, causing a substantial decrease in R_{TS} . Some of these pulses are reflected again after the collision with the HTS, indicating that magnetosonic pulses can survive a long time once generated in the heliosheath.

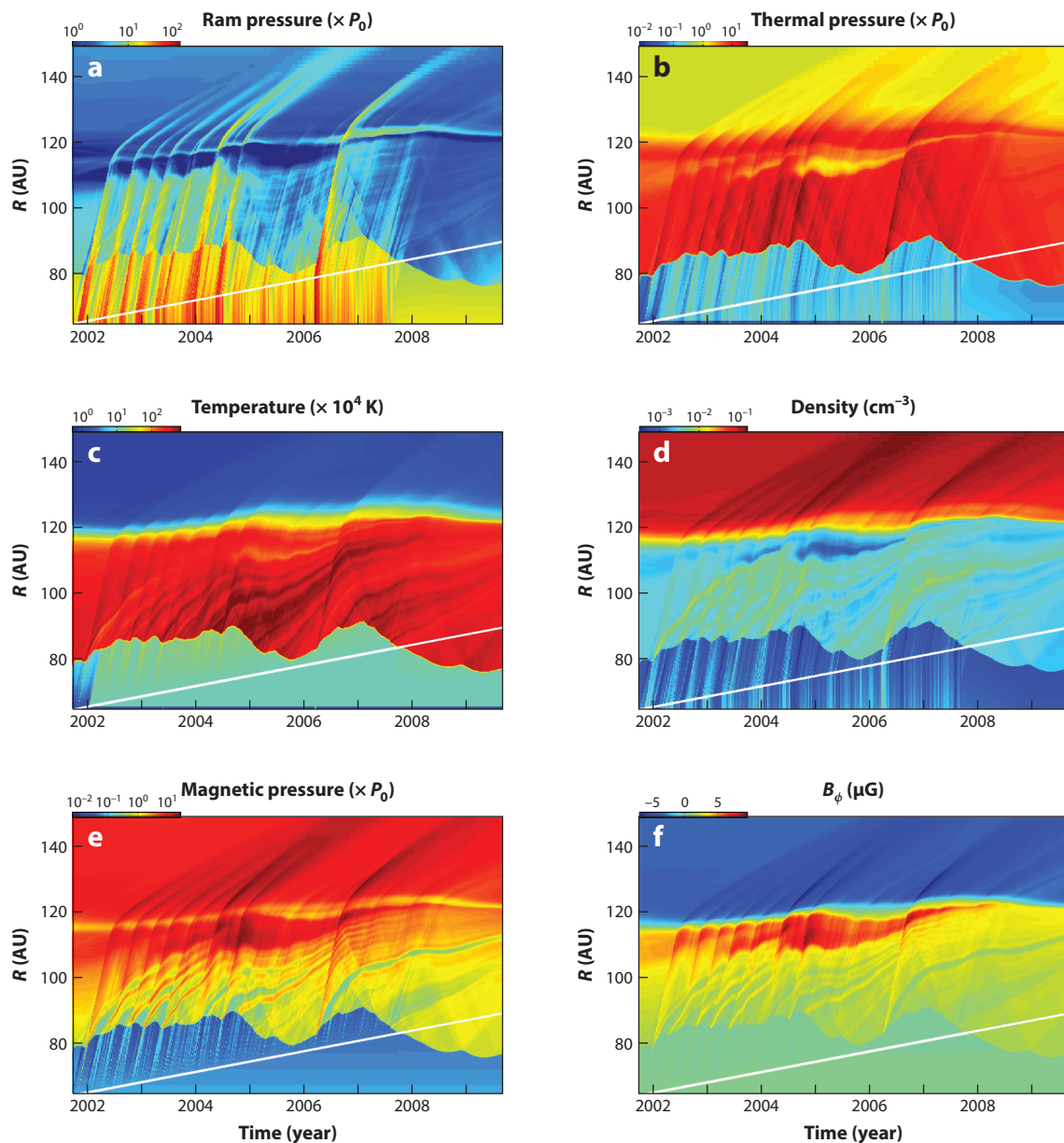


Figure 18

Space-time plots of (a) ram pressure, (b) thermal pressure, (c) temperature, (d) density, (e) magnetic pressure, and (f) magnetic field perpendicular to the meridional plane along the Sun-V2 direction. The magnetic field (f) corresponds to the toroidal magnetic field both in the heliosheath and in interplanetary space. The pressure constant P_0 is 1.38×10^{-14} Pa. The solid, straight white line denotes the V2 trajectory. The V2-observed solar-wind density and radial speed are assigned at the V2 position; hence, quantities below the V2 trajectory in interplanetary space have no meaning in this simulation. After the V2 crossing, the net inner boundary is shifted from the V2 position to a position 75 AU from the Sun, and a standard set of solar-wind quantities is assigned. Reprinted from Washimi et al. (2011) with permission. Abbreviation: V2, *Voyager 2*.

Washimi et al. (2011) showed that a series of magnetosonic pulses were generated by the Halloween events colliding with the HTS in mid-2004, which then propagated outward to the HP. The pulses were partially reflected back toward the HTS and partially transmitted into the VLISM. The reflected pulses collided with the HTS, driving it inward, which resulted in the V1-HTS crossing. Shown in **Figure 18**, the 2006 March high-ram-pressure pulse (Richardson et al. 2006) collided with the HTS, generating a large-amplitude magnetosonic pulse that was eventually partially reflected near the HP. After ~ 1.2 years from the generation of the pulse, the reflected pulse collided with the HTS, causing a substantial decrease in R_{TS} , which resulted in the V2-HTS crossing as was forecast by Washimi et al. (2007).

The time-varying HP surface along the Sun-V2 lines is identified by the temperature decrease associated with the color change from cyan to blue in **Figure 18**. A sharp increase in density is found in the IHS at approximately 118–120 AU in **Figure 18d**. This density-increase surface corresponds to a rapid decrease of temperature in **Figure 18c** and also to the magnetic-intensity minimum in **Figure 18e**. Along this line, the current should be the strongest; hence, this thin and strong current region can be identified as the current sheet. Just below this line, a region of maximum toroidal magnetic field intensity (**Figure 18f**) is present. These structures suggest that a plasma sheet is present with a width of a few astronomical units between the sharp density increase and the HP. At the lower side of the current sheet, the magnetic field will reach maximum strength (Washimi & Tanaka 1996; Pogorelov et al. 2004, 2006; Washimi et al. 2007, 2011). This magnetic field maximum or magnetic wall is located at 105–115 AU in **Figure 18f**. The thermal pressure in **Figure 18b** is reduced on the magnetic wall so that the sum of thermal and magnetic pressures is constant along the radial direction. **Figure 18c** shows that the temperature in the IHS is high but drops abruptly at the inner boundary of the plasma sheet and beyond. The simulations of Washimi et al. (2011) indicate that the heliosheath possesses a fine, layered structure with a magnetic wall, a plasma sheet, and a current sheet in the outer region of the IHS.

Washimi et al. (2012) showed that all electron flux enhancements, except for one, can be associated with times when a magnetosonic pulse, generated by the collision of an interplanetary shock with the HTS or by its subsequent reflection at the plasma sheet near the HP, passed V1. Thus, enhancements in electron flux appear to correspond directly or indirectly to IHS magnetosonic pulses driven by interplanetary shocks. By utilizing a timing related to their results, Washimi et al. (2012) inferred correctly “that V1 is possibly located near the HP within 4–8 AU at the present time.”

The time- and solar-cycle-dependent simulations described above (Pogorelov et al. 2009a, 2011, 2012; Washimi et al. 2007, 2011) all illustrate that the radial component of the SW velocity in the IHS along different trajectories can become negative for long periods, sometimes in excess of 1 year. The regions of negative velocity are relatively small in space-time diagrams, but the extent of the region can be 20 AU for a properly chosen time (in particular, see Pogorelov et al. 2009a, Washimi et al. 2011). V1 may have traversed such a region (Krimigis et al. 2011, Decker et al. 2012). On the basis of the simulations of Pogorelov et al. (2009a), Pogorelov et al. (2012) found that the latitudinal component of the IHS SW velocity tended toward zero and the longitudinal component dominated, qualitatively consistent with observations. In part, the complicated flow behavior stems from the formation of time-dependent magnetic barriers that separate IHS plasma regions that originate in the slow and fast wind (Pogorelov et al. 2012).

Observations derived from the IBEX-Lo instrument have provided a detailed, but disputed (Bertaux & Lallement 2015), parameterization of the LISM properties (Bochsler et al. 2012, Bzowski et al. 2012, Lee et al. 2012, Möbius et al. 2012, Saul et al. 2012). In particular, IBEX measurements revised earlier values of the interstellar flow vector derived from Ulysses

observations (Witte 2004), suggesting a value of 23.2 km s^{-1} rather than the previous value of 26 km s^{-1} . McComas et al. (2012a) resolved a small discrepancy between the inferred LISM parameters (i.e., the parameterized plasma velocity and temperature) and combined them with estimates of the density and magnetic field strength and orientation to conclude that the interaction of the SW with the LISM may be subfast magnetosonic and a BS may not be present.

Some original models had considered the possibility of a one-shock model (i.e., an HTS that bounds the supersonic SW and no BS). Included among these models are Parker's original gas dynamic model (Parker 1961) and the one-shock models of Zank et al. (1996b) that incorporated neutral H self-consistently. However, the general earlier consensus (circa 2000) was that the interaction of the SW with the LISM was of a two-shock character (i.e., the HTS and a BS existed owing to the supersonic relative motion of the Sun with respect to the LISM) (Baranov & Malama 1993; Pauls & Zank 1996, 1997; Baranov et al. 1971; Pauls et al. 1995; Zank et al. 1996b; Williams et al. 1997), even for an exceptionally strong LISM magnetic field (Florinski et al. 2004).

The nonlocal character of the charge-exchange process in the immediate interstellar neighborhood of the HP mediates the interstellar plasma. The creation of either fast or hot neutral H in the supersonic SW or IHS, respectively, leads to their propagation into the VLISM, where they experience secondary charge exchange (Zank et al. 1996b). This process may be responsible for the formation of the IBEX ribbon (McComas et al. 2009a, Chalov et al. 2010, Heerikhuisen et al. 2010). Secondary charge exchange in the LISM is dynamically important because it acts to heat the interstellar plasma (Zank et al. 1996b) to the extent that even a nominally superfast magnetosonic (as measured at a large distance) relative heliosphere-LISM flow can become subfast magnetosonic close to the HP and the BS may appear to be smoothed or even absent (Pogorelov et al. 2006, 2008, 2009c). Furthermore, even if a weak BS exists, charge exchange may be the primary dissipation mechanism, with the overall shock transition smoothed over the charge-exchange length scale, giving an adiabaticlike interaction region that is essentially "BS free."

Zank et al. (2013) investigated the nature of the VLISM plasma for different parameters as well as its implications for the BS and H wall. Many models, beginning with that of Gayley et al. (1997) and the observations of Linsky & Wood (1996), have used Lyman- α observations toward nearby stars to constrain models of heliospheric structure. Zank et al. (2013) used an MHD-kinetic neutral H model with a plasma κ distribution (Heerikhuisen et al. 2006, 2007; Pogorelov et al. 2008, 2011) and VLISM parameters that are consistent with IBEX ribbon observations and the HDP constraint. Three models with fixed LISM flow speed, plasma and neutral H density and temperature and varying LISM magnetic field strength (2, 3, and $4 \mu\text{G}$) were considered. This choice of parameters yields an interstellar plasma flow that is either (a) super-Alfvénic and superfast-magnetosonic, (b) barely super-Alfvénic and superfast-magnetosonic, or (c) sub-Alfvénic and subfast-magnetosonic. In the absence of VLISM H mediation, each of these cases should correspond respectively to (a) the existence of a relatively weak but well-defined fast-mode BS; (b) the existence of a very weak fast-mode BS, and (c) the absence of a BS ahead of the heliospheric obstacle, assuming a purely MHD interpretation of the interaction.

The simulations of Zank et al. (2013) show that model 1 ($|\mathbf{B}| = 2 \mu\text{G}$) very clearly possesses a BS-like transition, although comparatively weak, whereas model 2 ($|\mathbf{B}| = 3 \mu\text{G}$) possesses an extended smooth transition from superfast magnetosonic to subfast magnetosonic speeds, and model 3 ($|\mathbf{B}| = 4 \mu\text{G}$) has no BS. The plasma temperature exhibits a temperature gradient extending from the HP into the LISM beyond the BS/wave structure (Zank et al. 1996b). Hot neutral H created in the hot IHS propagates into the VLISM where it eventually charge-exchanges, producing hot protons, and thus forming an extended temperature gradient. Such nonclassical transport of heat across the HP (a tangential discontinuity), mediated by neutral H and charge

exchange, is quite unlike standard MHD. As a result of the temperature gradient, there is a gradual change in the sound (and hence magnetosonic) speed, increasing as it approaches the BS and HP region. This effect can be sufficiently strong that the magnetosonic speed increase can eliminate the formation of a BS, even for superfast magnetosonic far upstream conditions. In model 1, the LISM plasma is superfast magnetosonic (and super-Alfvénic) until the bow wave or mediated shock, where it transitions to a subfast magnetosonic flow. The far upstream flow for model 2 is just barely superfast magnetosonic and, like model 1, the fast Mach number M_f decreases slowly as it approaches the heliosphere. As seen from the density profile, the transition extends from ~ 650 AU to ~ 400 AU and $M = 1$ at ~ 700 AU. Although model 1 possesses a BS, it is weakened by the increasing sound speed, and structurally mediated by neutral H.

To illuminate why the transition is partially smoothed or even shock free and decelerates a superfast magnetosonic flow to a subfast state in the presence of a neutral H-mediated VLISM, Zank et al. (2013) showed that the 1D MHD equations for the VLISM i.e., with momentum and energy source terms $Q_{m,e}$, admit the critical point $Q_e = \frac{\gamma}{\gamma-1} U Q_m$ and fast magnetosonic Mach number $M_f = 1$. The source terms Q_m and Q_e are nonzero only because of the secondary charge exchange of fast and hot heliospheric neutral H. The critical point ensures that the VLISM flow incident on the heliosphere can be a smooth decelerating flow, or at least act to partially smooth the BS.

Charge exchange of fast and hot neutral H, therefore, provides part of the dissipation mechanism for the weak BS in the $2 \mu\text{G}$ case since it possesses a critical point within the transition. The structure may therefore be viewed as a neutral H-mediated shock wave. By contrast, the barely superfast magnetosonic flow of model 2 can be decelerated completely by fast and hot neutral H experiencing charge exchange in the LISM. The transition occurs over ~ 200 AU, which is approximately two to three times the charge-exchange mfp in the LISM, which is consistent with the transition length scale if neutral H were the primary dissipation mechanism. Since the decelerated transition occurs smoothly from a superfast to a subfast magnetosonic state, mediated by fast and hot neutral H, and we can describe the transition as BS free or as a bow wave. The nonlinear feedback of LISM and heliosphere can therefore have a profound influence on the heliospheric-VLISM interface. Scherer & Fichtner (2014) suggested that the inclusion of heavy LISM ions (specifically He^+) may offset the increased sound speed that is a consequence of secondary neutral H heating.

A powerful diagnostic tool for constraining the structure of the global heliosphere is the absorption of stellar Lyman- α light by interstellar neutral H observed by the *Hubble Space Telescope* (Linsky & Wood 1996, Gayley et al. 1997). The absorption signatures in stellar Lyman- α are mediated by the neutral H created in the SW-LISM boundaries, and the extent of this mediation can provide constraints on theoretical models of the global heliosphere (Wood et al. 2000, 2005b, 2007a,b; Zank et al. 2013) as well as different stars (Müller et al. 2001; Wood et al. 2001, 2002, 2005a).

Using 3D MHD-kinetic models, Zank et al. (2013) synthesized Lyman- α absorption profiles for models 1, 2, and 3 along four sightlines and compared with those observed. They concluded that the highly subfast magnetosonic LISM case with $|\mathbf{B}| = 4 \mu\text{G}$ cannot account consistently for the observed Lyman- α absorption along different sightlines. In addition, a marginally superfast magnetosonic LISM can account consistently for the observed absorption along all the sightlines considered here. A weaker conclusion is that the $3\text{-}\mu\text{G}$ model may be marginally better than the two-shock $2\text{-}\mu\text{G}$ model, particularly if weighted by the α -Cen observations. The analysis by Zank et al. (2013) showed that the Lyman- α absorption data are consistent with a very slightly superfast magnetosonic LISM wind, regardless of the complex physics involved in such a marginal $M \sim 1$ shock transition.

Ben-Jaffel et al. (2013) presented a sensitivity study of the VLISM plasma constrained by several distinct and complementary observations of the LISM, SW, and inner heliosphere. Assuming IBEX He flow parameters for the LISM, Ben-Jaffel et al. (2013) fit V1 and V2 in situ plasma measurements and IBEX ENA ribbon data to derive an ISMF strength of $\sim 2.7 \pm 0.2 \mu\text{G}$ in a direction pointing away from galactic coordinates $(28, 52) \pm 3^\circ$. When using Ulysses parameters for the LISM He flow, Ben-Jaffel & Ratkiewicz (2012) reported the same direction but with a strength of $2.2 \pm 0.1 \mu\text{G}$. These results are based on the heliospheric model of Ratkiewicz et al. (2008) (see also Grygorczuk et al. 2011, Strumik et al. 2011), which assumes a constant flux of H, unlike the various models described above that incorporate the detailed spatial distribution of H using either kinetic or multifluid descriptions. Ben-Jaffel et al. (2013) found that using the Ulysses He flow yields a solution that is in the expected HDP, whereas the IBEX He flow yields a solution that is $\sim 20^\circ$ away from the corresponding HDP plane. That these results are based on an MHD model that omits virtually all the basic physical processes of the interaction of the H interactions with the interstellar plasma and the boundary regions raises questions about the accuracy of the conclusions of Ben-Jaffel et al. (2013). It is notable that the simulations of Heerikhuisen et al. (2014), Zank et al. (2013), and Borovikov & Pogorelov (2014) used the HDP and the IBEX ribbon orientation as constraints while satisfying the IBEX He flow. The profound differences in the completeness of the global heliospheric models of Heerikhuisen et al. (2014), Zank et al. (2013), and Borovikov & Pogorelov (2014) compared with those of Ratkiewicz et al. (2008), Grygorczuk et al. (2011), and Strumik et al. (2011) may invalidate the conclusions of Ben-Jaffel et al. (2013). By completely neglecting the heating of the VLISM by hot secondary H created in the IHS and supersonic SW, the VLISM temperatures modeled by Ben-Jaffel et al. (2013) are incorrect and conclusions about the existence of a fast interstellar BS cannot be drawn on the basis of incomplete heliospheric global models.

3.4. Plasma Distributions in the Inner Heliosheath and Very Local Interstellar Medium

The TS-3 crossing of the HTS revealed an almost classical perpendicular shock structure (Burlaga et al. 2008, Richardson et al. 2008), except that the observed average downstream proton plasma temperature was an order of magnitude smaller than predicted by the MHD Rankine-Hugoniot conditions (Zank et al. 2009). The transmitted SW proton distribution is a broadened/heated Maxwellian (with a somewhat flattened peak), and there is no evidence of reflected SW ions being transmitted downstream (Richardson 2010). Richardson et al. (2008) and Richardson (2009) concluded that PUIs experienced preferential heating at the HTS and thus PUIs provide both the primary shock dissipation mechanism and the bulk of the hot plasma downstream of the TS, as predicted by Zank et al. (1996a). Thus, V2 observations support the basic model of Zank et al. (1996a) for the microstructure of the HTS. However, both the observed SW proton distribution and a shock dissipation mechanism based on PUIs indicate that the downstream proton distribution function is a (possibly complicated) function of the physics of the HTS. Zank et al. (2010) developed a basic model of a quasi-perpendicular HTS, mediated by PUIs, to derive the complete downstream proton distribution function in the IHS, determine the partitioning of energy between SW protons and PUIs, and infer the implications of the constructed IHS proton distribution function for the ENA spectral flux observed by IBEX.

Zank et al. (2010) introduced a three-distribution approximation of the IHS plasma, including core SW protons, transmitted (without reflection) PUIs, and reflected (and then transmitted) PUIs. The reflected PUI population resulted from the reflection of some upstream PUIs at the cross-shock electrostatic potential of the quasi-perpendicular HTS. Reflected PUIs are the primary

dissipation mechanism at the HTS (Zank et al. 1996a, Burrows et al. 2010). The post-HTS PUI distribution is likely highly complex (e.g., Chalov & Fahr 2000; Wu et al. 2009). Yet, as a first approximation, Zank et al. (2010) assumed that the SW proton distribution is a Maxwellian, and because the number of PUIs reflected is comparatively small, they made the simplifying assumption that the nonreflected PUI distribution can be approximated by the filled-shell distribution. The downstream temperatures for the transmitted and reflected PUIs can be computed (Zank et al. 2010), allowing for the partitioning of downstream thermal energy into transmitted SW protons, transmitted PUIs, and reflected and then transmitted PUIs. Zank et al. (2010) found that the smoothed form of the constructed heliosheath proton distribution resembles a κ distribution. As a result, a significant number of protons reside in the wings of the distribution function, quite unlike the Maxwellian distribution. There are several noteworthy points about the constructed IHS proton distribution functions: (a) the narrowness of the transmitted SW proton distribution, (b) the broadening of the distribution function by the transmitted PUIs out to approximately $5 v_{th}$ (where v_{th} is the thermal velocity corresponding to a Maxwellian distribution with temperature T , in this case, the total downstream plasma temperature), and (c) the downstream reflected PUIs considerably extend the outermost wings of the total proton distribution function. The filled-shell assumption for the transmitted PUIs probably overestimates the hardness of the spectrum, and the spectrum is likely to be intermediate to the two cases considered. The close correspondence between the constructed distributions and the κ distribution with index 1.63 is useful in allowing for simplified simulations based on a κ distribution. Zank et al. (2010) predicted that the constructed heliosheath proton distribution, under both assumptions for the transmitted PUIs, possesses some structure that may manifest itself in ENA spectra observed at 1 AU by IBEX. They also predicted that the microphysics of the HTS may play a key role in determining the form of the total downstream or heliosheath proton distribution.

In a first study, Desai et al. (2012) found that the fluxes, energy spectra, and energy dependence of the spectral indexes of ~ 0.5 – 6 -keV ENAs measured by IBEX-Hi along the V1 and V2 lines of sight were consistent within a factor of ~ 2 with the model results of Zank et al. (2010). The observed ENA spectra do not exhibit sharp cutoffs at approximately twice the SW speed as is typically found for shell-like PUI distributions in the heliosphere. Desai et al. (2012) concluded that the ENAs measured by IBEX-Hi are generated by at least two types of ion populations whose relative contributions depend on the ENA energy: transmitted PUIs in the ~ 0.5 - to 5 -keV energy range and reflected PUIs above ~ 5 -keV energy. Desai et al. (2012) concluded that the ~ 0.5 - to 5 -keV PUI distribution is probably a superposition of Maxwellian or κ distributions and partially filled-shell distributions in velocity space.

The theory by Zank et al. (2010) does not well describe the observed lower-energy ENAs (below ~ 0.5 keV), and most existing models underestimate the ENA fluxes between ~ 0.05 and 0.5 keV by an order of magnitude or more (Fuselier et al. 2012). The empirical model of Gloeckler & Fisk (2010) also requires IHS turbulence amplitudes substantially larger than those measured by V2 to generate a suprathermal PUI tail $\propto E^{-1.5}$ (Desai et al. 2014). An important assumption in Zank et al. (2010) was to keep the relative density and temperature for each population constant throughout the IHS during postprocessing. Zirnstein et al. (2014) improved upon this process: They simulated the extinction of SW protons and transmitted and reflected PUIs by charge exchange by neutral H. They introduced a new “injected” PUI population, which increases in density for every charge exchange. This extinction process alters the distribution of energy in the IHS, which is different from assuming that the relative energy densities of the core SW protons as well as the transmitted and reflected PUIs remain constant. Although the MHD-kinetic simulations may approximate the total energy and density of SW-LISM protons and PUIs, the partitioning of the energy is essential for understanding the role that PUIs play in the heliosphere and its effect on H ENA flux.

ENAs are created everywhere in the SW-LISM interaction region. Yet, ENAs produced in the IHS easily propagate into the VLISM before charge exchange occurs, creating a population of PUIs there. However, because ENAs produced in the OHS do not easily charge exchange in the IHS, they permeate the inner heliosphere and can be detected at 1 AU.

Zirnstein et al. (2014) extended the IHS concept of partitioning energy into various proton populations to the VLISM. The VLISM plasma consists mostly of protons, initially $\sim 6,300$ K in the pristine LISM (Bzowski et al. 2012, McComas et al. 2012a, Möbius et al. 2012), that are partially heated by charge exchange near the H wall and by crossing a bow wave (McComas et al. 2012a, Zank et al. 2013). However, the increase in thermal energy of the VLISM plasma near the HP is also due to energetic PUIs, which are created from charge exchange between LISM protons and ENAs from the IHS (Zank et al. 1996b). Most PUIs are in close proximity to the HP and drop off exponentially at larger distances owing to the mfp of their parent ENAs and to advection with the LISM flow toward the HP (Zirnstein et al. 2014). As with the IHS, Zirnstein et al. (2014) determined the VLISM PUI properties by partitioning the total energy from the plasma-neutral results between LISM protons and PUIs. Because ENAs from IHS protons may propagate into the VLISM and charge exchange to become PUIs, Zirnstein et al. (2014) treated the postprocessed VLISM plasma as a five-component distribution: They included protons from the core (and compressed) VLISM plasma as well as PUIs created by charge exchange from IHS ENAs.

Figure 19a shows various sources of the H spectrum in the V1 and V2 direction based on the extended model of Zirnstein et al. (2014) with a comparison to the corrected IBEX data (Desai et al. 2014). Below ~ 0.5 keV, the flux is dominated by ENAs from injected PUIs, whereas ENAs from transmitted and reflected PUIs dominate above 0.5 keV. Although a small fraction of ENAs from core SW protons are visible at 1 AU, most exit the HP and become PUIs in the VLISM, producing significant flux near ~ 0.1 keV.

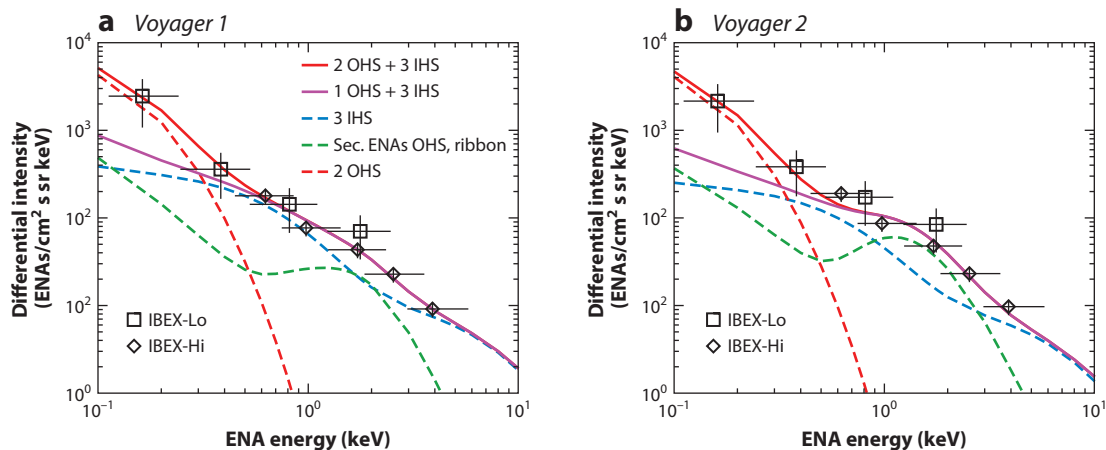


Figure 19

IBEX-Hi and IBEX-Lo ENA spectra compared with the simulations of Zirnstein et al. (2014): (*dashed green*) ENAs from a secondary VLISM population, forming the ribbon; (*dashed blue*) three IHS populations with Maxwellian distributions; (*dashed red*) ENAs from a hot, pickup-ion VLISM population; (*solid purple*) superposition of all three IHS, the secondary ENAs from the ribbon, and a single completely thermalized VLISM population (not visible); (*solid red*) superposition of all three IHS, the secondary ENAs from the ribbon, and the two proton VLISM populations. Reprinted from Desai et al. (2014) with permission. Abbreviations: ENA, energetic neutral atom; IBEX, Interstellar Boundary Explorer; IHS, inner heliosheath; OHS, outer heliosheath; VLISM, very local interstellar medium.

Zirnstein et al. (2014) predicted that a significant part of the ENA flux seen at 1 AU comes from the VLISM. ENAs created from SW PUIs in the VLISM dominate the flux below ~ 0.2 keV, whereas secondary-injected, -transmitted, and -reflected PUIs contribute a significant flux up to kiloelectron volt energies, comparable to the flux from the IHS. Opher et al. (2013) suggested that the low-energy flux from IBEX-Lo may originate from a suprathermal ion population in the OHS, where they used a κ distribution to model the VLISM plasma source for ENAs. However, the detailed model of Zirnstein et al. (2014) exploited the properties of PUIs that contribute to heating the VLISM plasma, thereby establishing that not only the low- but also the high-energy flux is a result of the coupling between the IHS and OHS plasmas through charge exchange. PUIs from the IHS are the source of multiple PUI species in the VLISM. The simulation results of Zirnstein et al. (2014) compare favorably with IBEX data, but their results are low compared with IBEX at high energies because OHS PUIs created from supersonic SW ENAs or time-dependent SW boundary conditions were not included. Nonetheless, these results suggest strong coupling between the IHS and OHS plasmas through ENA charge exchange, where OHS PUIs may dominate the globally distributed ENA flux visible at 1 AU up to ~ 10 keV. The results from the theoretical models of Zank et al. (2010) and Zirnstein et al. (2014) and the observational results of Desai et al. (2012, 2014) confirm that the IHS and VLISM are multicomponent nonequibrated plasmas and that simplified single-fluid MHD plasma descriptions need to be revised. The multifluid model introduced by Zank et al. (2014) is the first rigorous attempt to extend basic models to incorporate the physics of nonthermal PUI distributions.

3.4.1. Modeling the interstellar boundary explorer ribbon. An unexpected feature present in the IBEX ENA maps was a ribbon that encircles the sky, passing closer to the heliospheric nose direction in the south and west than in the north and east (McComas et al. 2009a). The ribbon is a nearly threefold enhancement in ENA flux compared with adjacent parts of the sky. The shape and magnitude of the energy spectrum are primarily ordered by ecliptic latitude rather than its location inside or outside of the ribbon (Funsten et al. 2009b). This suggests that ENAs inside the ribbon come from the same population of parent ions. Using results from Pogorelov et al. (2009a), the IBEX team discovered the relationship between the ribbon and the region just outside the HP where the ISMF is perpendicular to radial vectors from the Sun (Funsten et al. 2009b, McComas et al. 2009a, Schwadron et al. 2009). Several possible explanations for this correlation have been given, including the only one to date that explains the orientation, structure, and intensity of the IBEX ribbon (Heerikhuisen et al. 2010).

The average velocity of ions in the SW and IHS is antisunward, so the majority of ENAs propagate away from the Sun into the VLISM. In the VLISM, some of these ENAs charge exchange and create PUIs. The PUIs initially form a ring-beam distribution, with a velocity component along the magnetic field. Possibly, over time, the ring-beam distribution will be isotropized by wave-particle interactions (Lee & Ip 1987, Williams & Zank 1994). However, the ring-distributed PUIs may charge exchange with interstellar H, so creating new “secondary” ENAs [Izmodenov et al. (2009) modeled this process for an isotropic PUI distribution]. If “reneutralization” occurs more rapidly than the timescale on which PUIs scatter to a full shell, then the secondary ENA will be directed to some random vector on a partial shell. Furthermore, in locations where the VLISM magnetic field $\mathbf{B}_{VLISM} \cdot \mathbf{r} \simeq 0$, the plane of the ring intersects the Sun and leads to an increased ENA flux from these locations. Heerikhuisen et al. (2010) demonstrated that this mechanism could explain the link between the ribbon and the orientation of the ISMF.

The implementation of the secondary ENA model yields a very accurate correspondence between the observed and simulated ribbons (illustrated in **Figure 20**). The mechanism suggests that the ISMF is directed close to the ecliptic coordinates (224, 41) used in the model by Heerikhuisen

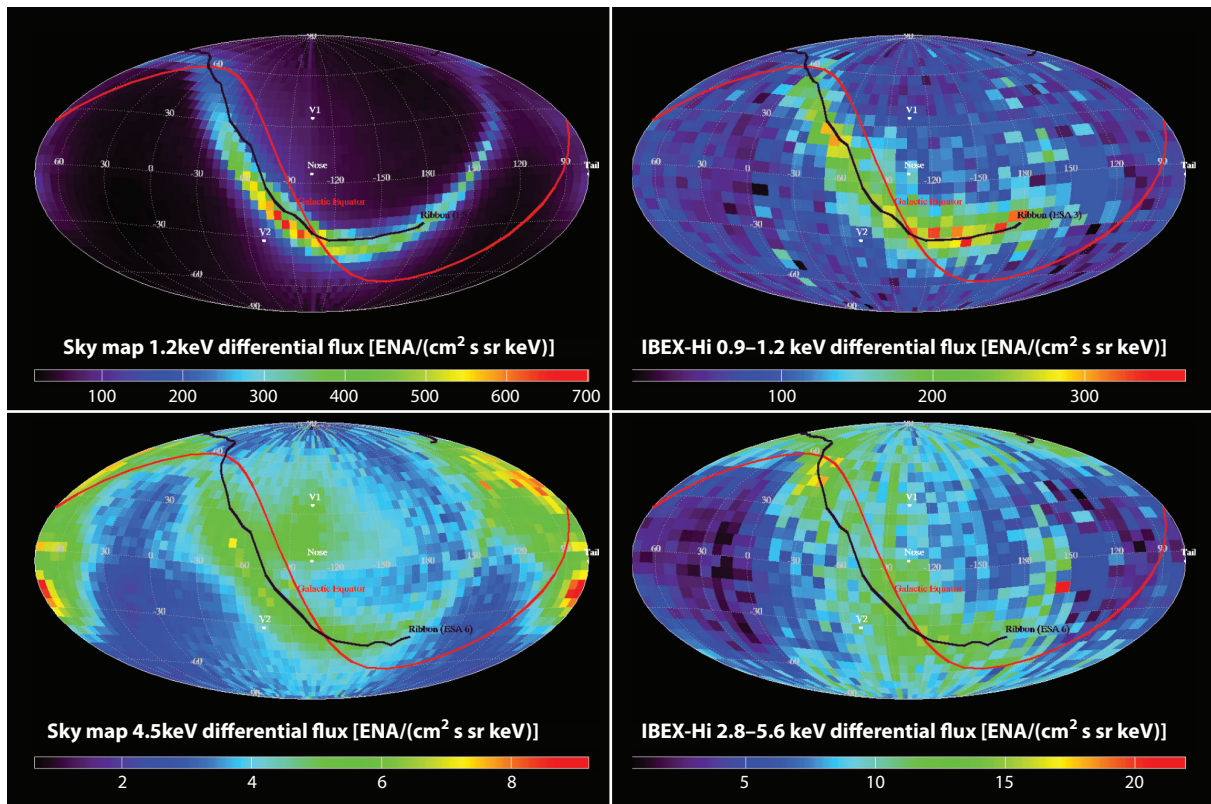


Figure 20

All-sky maps of (*left*) simulated and (*right*) observed ENA fluxes at (*top*) 1.1 keV and (*bottom*) 4.5 keV. The simulation uses a $\kappa = 1.63$ spectral index for inner heliosheath protons, and all pickup ions are described as partial-shell distributions for a time long enough to ensure reneutralization before they isotropize. The red curve indicates the galactic plane, and a best fit to the observed ribbon is shown as a black line. The ribbon shifts down slightly at high energies. Units of ENA flux are $(\text{cm}^2 \text{ s sr keV})^{-1}$. Reprinted from Heerikhuisen et al. (2010) with permission. Abbreviations: ENA, energetic neutral atom; IBEX, Interstellar Boundary Explorer; V1, *Voyager 1*; V2, *Voyager 2*.

et al. (2010) and close to the value (221, 39) corresponding to the center of the ribbon derived from observations by Funsten et al. (2009b) (see also Heerikhuisen & Pogorelov 2011). The formation of the ribbon is a natural consequence of a multicomponent, nonequibrated VLISM plasma model (Zank et al. 2014, Zirnststein et al. 2014).

Heerikhuisen et al. (2014) extended the results of Zank et al. (2013), particularly in modeling the ENAs. Of interest is the remarkably circular shape of the IBEX ribbon, already recognized in the first IBEX papers (Funsten et al. 2009b). Funsten et al. (2013) analyzed the IBEX data from all-sky maps at five energies and concluded that the observed ribbon is very circular (eccentricity ~ 0.3) with its center at ecliptic J2000 coordinates $(219.2 \pm 1.3, 39.9 \pm 2.3)$. Using the secondary ENA model with coupled MHD-kinetic neutral H simulations, Heerikhuisen et al. (2014) compared the circularity of the ribbon with four simulations (VLISM magnetic field strengths of 1, 2, 3, and 4 μG) and found that the 3- μG model was very similar. The close similarity of the simulation results and observed ribbon flux suggest that the true LISM magnetic field direction is near the center of the observed ribbon. Circularity fits from the simulations show that the ribbon center is

offset from the LISM magnetic field direction by approximately 10° and 5° for the 2- and 3- μG cases, respectively. Because the simulated ribbon shape and width are closely related to how the magnetic field drapes around the HP, the simulations of Heerikhuisen et al. (2014) can be used to deduce the most likely field strength based on which simulation(s) best match the observed ribbon. The 3- μG case provides the best match, followed closely by the 2- μG case. Thus, the LISM magnetic field is likely $\sim 2.5\text{--}3 \mu\text{G}$ and directed either toward or away from the center of the ribbon near ecliptic J2000 coordinates (220,40), consistent with the Lyman- α absorption results of Zank et al. (2013).

A key assumption underpinning the secondary ENA model is that the newly born PUI ring is relatively stable with respect to wave generation, so that it can undergo charge exchange before becoming isotropized. Using linear kinetic theory and hybrid simulations, Florinski et al. (2010) investigated the stability of a low-density PUI ring created in the VLISM. A broadband spectrum of waves is excited by the cyclotron instability, which then scatters the ring ions efficiently toward an isotropic shell-like distribution. From these simulations, it appears that the secondary ENA mechanism cannot possibly work in the VLISM. Nonetheless, several variants of the model of Heerikhuisen et al. (2010) may address the drawback of rapid PUI scattering (Chalov et al. 2010, Liu et al. 2012, Möbius et al. 2013, Schwadron & McComas 2013, Isenberg 2014), which include rapid scattering in dominant turbulence and the spatial retention of PUIs in regions satisfying $\mathbf{B} \cdot \mathbf{r} \simeq 0$.

Using a modeled initial ENA distribution (Heerikhuisen et al. 2014), Burlaga et al. (2014) presented 1D hybrid simulations of the relaxation of a PUI ringlike distribution. The wavenumber range of the V1 48-s data overlaps the range of waves that would be generated by the simulated relaxation of a PUI ring. Burlaga et al. (2014) found that the amplitude of the simulated fluctuations was more than three orders of magnitude above the V1 magnetometer-measured wave intensity. Clearly, the observations and simulations are incompatible. This result rules out large excesses of turbulent power in the PUI resonance range, implying that the instability is not a prolific source of waves, at least for the current value of the pickup angle given by $\cos^{-1}(\cos \lambda \cos \delta) = 70^\circ$ using the values of λ and δ from Burlaga & Ness (2014) and estimating the interstellar field as being directed toward the center of the ribbon.

The VLISM just past the HP should be the most favorable location for wave generation (Liu et al. 2012). However, Gamayunov et al. (2010) have argued that the ring could be marginally stabilized by a combination of ambient and locally generated turbulence. The very low level of turbulence in the range of PUI self-generated waves may explain why a ribbon model that relies on low levels of PUI scattering appears to reproduce so many of the quantitative aspects of the IBEX ribbon (Heerikhuisen et al. 2014). The V1 observations of quiescent turbulence suggest that spatial confinement of PUIs through high rates of scattering by self-generated waves (Schwadron & McComas 2013, Isenberg 2014) is unlikely to be viable candidate to explain the ribbon. However, why the VLISM fluctuations are so quiescent remains an open question. This may have been answered in part by Zank et al. (2014), who used linear wave analysis of the multicomponent nonequibrated plasma equations to show that PUIs damp all the waves in the VLISM. The interpretation of the *Voyager* data as an upper limit on magnetic fluctuations is compatible with the VLISM turbulence estimates. The rapid disappearance and large anisotropies of ACRs past the heliocliff (Krimigis et al. 2013, Stone et al. 2013) indicate that the scattering rates in the VLISM must be extremely low, which is consistent with the very weak turbulence observed by V1.

3.4.2. Stability of the heliopause. Simulations of Zank et al. (1996b) and Liewer et al. (1996) showed that the HP exhibited a form of instability. Zank (1999b) identified this instability: They showed that frictional drag between the plasma and neutral H in the vicinity of the HP would

drive a Rayleigh–Taylor-like instability. Subsequent simulations confirmed the existence of a Rayleigh–Taylor-like instability caused by charge exchange between the primary neutrals from the VLISM and SW ions (Florinski et al. 2005, Borovikov et al. 2008). The linear stability analysis of Zank (1999b) and Florinski et al. (2005) was extended by Avinash et al. (2014), who included a number of effects that are important in the heliosphere: resonant charge exchange between primary interstellar neutrals atoms and the SW plasma, interstellar, and heliosheath magnetic fields; plasma flows in the vicinity of the HP; and the effects of ENAs or secondary hot neutrals from the IHS. Numerical simulations show that the ENAs play a significant role in destabilizing the flanks of the HP. Consistent with high-resolution simulations (Borovikov et al. 2008), the linear dispersion relation (Avinash et al. 2014) shows that, in the relevant parameter space, the HP nose region where plasma flows are weak is unstable to Rayleigh–Taylor-like modes, the shoulder region is unstable to mixed Rayleigh–Taylor–KH (Kelvin–Helmholtz)-like modes, and flank regions (with strong flow and flow shear) are unstable to a KH-like instability.

Three-dimensional MHD–neutral simulations show that the instabilities discussed above are considerably suppressed near the HP nose by the heliospheric magnetic field but reassert themselves in the presence of solar-cycle effects. Borovikov & Pogorelov (2014) found that the nose of the HP is subject to Rayleigh–Taylor-type instabilities when a solar-cycle time-dependent 3D MHD–neutral model is used. They also found that the HP flanks are always subject to a KH instability, in agreement with the theoretical analysis of Avinash et al. (2014).

Avinash et al. (2014) considered the effect of an HP instability dragging a loop of the ISMF into the IHS. They showed that sections of the VLISM and IHS magnetic fields could experience reconnection. Islandlike structures are not likely to form; instead, the IHS magnetic field connects to the VLISM magnetic field, yielding a relatively simple final configuration (Washimi et al. 2014). The reconnected field lines connect the IHS to the VLISM and thus allow direct access of energetic particles into and out of the ISM (ACRs and GCRs). A signature of such reconnection could also be the observation of solar periodicities and fluctuations beyond the HP in either the magnetic field or energetic particles.

3.4.3. Modeling Lyman- α backscatter. Since their respective launches, Pioneer 10 (P10), V1, and V2 have made UV radiation measurements within the heliosphere at increasing heliocentric distances. Despite the availability of UV observations, related simulations have not been considered in much detail, in part because a complex heliospheric model as well as an accurate radiative transfer model are needed. Past attempts to match the observed Lyman- α backscatter observations (Hall 1992; Hall et al. 1993; Gangopadhyay et al. 2002, 2005, 2006; Quémerais et al. 2003, 2009) have not been especially successful, indicating that either a more sophisticated model of neutral H or a better reduction method for the observational data is needed.

Fayock et al. (2013) used 3D MHD–kinetic neutral H models and a new 3D Monte Carlo radiative transfer code (Fayock 2013) to simulate Lyman- α backscatter throughout the heliosphere for solar minimum conditions. The relative density of Lyman- α backscatter is directly related to UV observations made by P10, V1, and V2. Fayock et al. (2013) found that the backscatter intensity falls off with increasing radius in all directions. Fayock et al. (2013) predicted a modest intensity increase in the upwind direction, but revised simulations (B. Fayock, private communication) indicate that the intensity should continue to decrease despite the presence of the H wall. The downwind direction decreases uniformly and exhibits no significant features.

Fayock et al. (2013) normalized the UV backscatter intensity at ~ 15 AU for both observations and simulations along each spacecraft flight path and evaluated the evolution in intensity with increasing heliocentric distance. The V1 and V2 observational data until 1992 (Hall 1992, Hall et al. 1993) are compared with the results of Fayock et al. (2013) (**Figure 21**). Good agreement

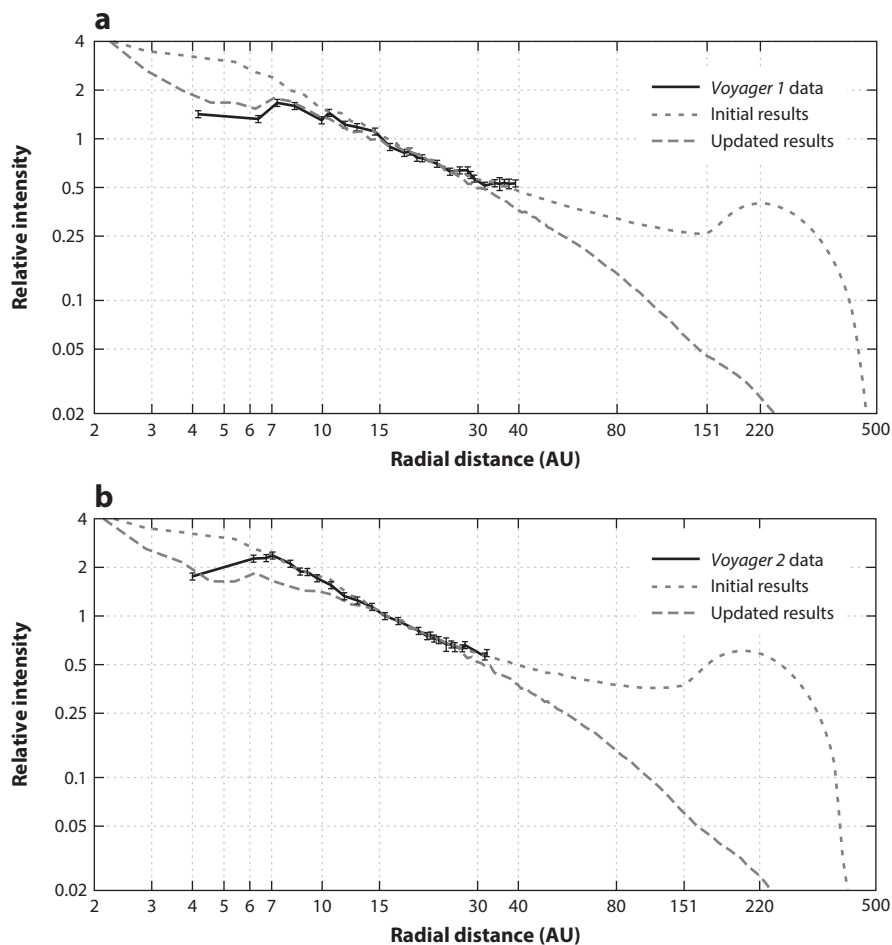


Figure 21

(a) *Voyager 1* comparison of Lyman- α backscatter observations and simulations. Fayock et al. (2013) introduced an artificial ionization cavity within ~ 7 AU, as this region is not sufficiently well resolved in current models. Beyond ~ 7 AU, the simulated slope closely matches observations. Note that there is very little predicted difference in the backscatter intensities beyond ~ 7 AU with and without the ionization cavity. (b) *Voyager 2* comparison of the Lyman- α backscatter between observations and simulations. Two theoretical curves are illustrated; the short-dashed curves correspond to the Fayock et al. (2013) simulations, and the long-dashed curves correspond to revised simulations (B. Fayock, private communication). Adapted from Fayock et al. (2013) with permission.

from ~ 7 AU to ~ 35 AU, the extent of the reduced observations, has been found. The P10 results do not agree with the predicted intensity (Fayock et al. 2013) within ~ 15 AU, which is much higher than observed. Several factors may be responsible for the discrepancy with the P10 data, including uncertain knowledge of the look direction of the P10 Lyman- α instrument during the period and its sensitivity to other sources (Wu et al. 1981, 1988; Gangopadhyay & Judge 1989; Gangopadhyay et al. 1989; Hall et al. 1993).

Although Fayock et al. (2013) predicted that the H wall should be observed in the V1 and V2 Lyman- α instruments near and beyond the HP, revised simulations suggest this is not so

(Figure 21). One conclusion that emerges from Fayock et al. (2013) is that the essential physics underlying the interaction of the SW with the LISM is well captured by the 3D MHD-kinetic model as interpreted on the basis of Lyman- α backscatter modeling. Radiative transfer modeling is an underutilized approach for validating and constraining large-scale models of the heliosphere.

4. CONCLUSIONS

The wealth of the combined in situ data from V1 and V2, IBEX observations of ENAs created in the remote reaches of the heliosphere and VLISM, and Lyman- α absorption and backscatter observations have yielded a golden age for the study of the interaction of the SW with the LISM. The extent and detail of the data have enabled impressive advances in our theoretical understanding and modeling of the coupled heliosphere-LISM system. It is remarkable, for example, that we can probe the detailed microphysics of the HTS remotely at 1 AU using ENA measurements in concert with a single brief suite of V2 in situ observations. We are beginning to achieve a fairly detailed understanding of the basic plasma physics of the boundary regions and the VLISM, recognizing that the physics is determined in large part by the complex coupling of neutral H and PUIs from multiple sources with the thermal plasma, i.e., a multicomponent nonequibrated partially ionized plasma. Just as the past decade has revealed that the coupling of plasma and interstellar neutral H in large part determine outer heliospheric physics, so too are we beginning to recognize that heliospheric neutral material and processes mediate the VLISM. The coming decade promises to be very exciting as we begin to explore the VLISM in situ and remotely. Discovery science always provides more surprises and questions than answers, ensuring the attention of space physicists and astrophysicists for years to come.

It is fitting to conclude this review by looking forward to extending and developing many of the ideas discussed here to the interaction of stellar winds with the ISM. For example, Cox et al. (2012) have presented an extraordinary variation of possible structures that reflect a variety of stellar winds interacting with their local ISM. With the many observational techniques that exist for investigating astrospheres across multiple wavelengths, the physics learned from the heliosphere will carry over to the new field of astrospherical astrophysics.

DISCLOSURE STATEMENT

The author is not aware of any affiliations, memberships, funding, or financial holdings that might be perceived as affecting the objectivity of this review.

ACKNOWLEDGMENTS

This work was supported by IBEX NASA/SwRI award NNG05EC85C, subcontract A99132BT, and NASA grant NNX10AC17G. G.P.Z. appreciates discussions at the team meeting “Heliosheath Processes and Structure of the Heliopause: Modeling Energetic Particles, Cosmic Rays, and Magnetic Fields” supported by the International Space Science Institute in Bern, Switzerland.

LITERATURE CITED

- Avinash K, Cox SM, Shaikh D, Zank GP. 2009. *Ap. J.* 695:420
Avinash K, Zank GP. 2007. *Geophys. Res. Lett.* 34:5106
Avinash K, Zank GP, Dasgupta B, Bhadoria S. 2014. *Ap. J.* 791:102
Axford WI, Leer E, McKenzie JF. 1982. *Astron. Astrophys.* 111:317

- Baranov VB, Krasnobaev KV, Kulikovskii AG. 1971. *Sov. Phys. Dokl.* 15:791
- Baranov VB, Malama YG. 1993. *J. Geophys. Res.* 98:15157
- Ben-Jaffel L, Ratkiewicz R. 2012. *Astron. Astrophys.* 546:A78
- Ben-Jaffel L, Strumik M, Ratkiewicz R, Grygorczuk J. 2013. *Ap. J.* 779:130
- Bertaux J-L, Blamont JE. 1971. *Astron. Astrophys.* 11:200
- Bertaux J-L, Lallement R. 2015. *J. Phys. Conf. Ser.* 577:012004
- Bertaux J-L, Lallement R, Kurt VG, Mironova EN. 1985. *Astron. Astrophys.* 150:1
- Bochsler P, Petersen L, Möbius E, et al. 2012. *Ap. J. Suppl.* 198:13
- Borovikov SN, Pogorelov NV. 2014. *Ap. J. Lett.* 783:L16
- Borovikov SN, Pogorelov NV, Zank GP, Kryukov IA. 2008. *Ap. J.* 682:1404
- Burlaga LF. 1968. *Sol. Phys.* 4:67
- Burlaga LF, Ness NF. 1968. *Can. J. Phys. Suppl.* 46:962
- Burlaga LF, Ness NF. 2009. *Ap. J.* 703:311
- Burlaga LF, Ness NF. 2010. *Ap. J.* 725:1306
- Burlaga LF, Ness NF. 2011. *Ap. J.* 737:35
- Burlaga LF, Ness NF. 2014. *Ap. J.* 784:146
- Burlaga LF, Ness NF, Acuña MH. 2006. *Ap. J.* 642:584
- Burlaga LF, Ness NF, Acuña MH. 2009a. *Ap. J. Lett.* 691:L82
- Burlaga LF, Ness NF, Acuña MH, et al. 2005. *Science* 309:2027
- Burlaga LF, Ness NF, Acuña MH, et al. 2008. *Nature* 454:75
- Burlaga LF, Ness NF, Acuña MH, et al. 2009b. *Ap. J.* 692:1125
- Burlaga LF, Ness NF, Florinski V, Heerikhuisen J. 2014. *Ap. J.* 792:134
- Burlaga LF, Ness NF, Gurnett DA, Kurth WS. 2013a. *Ap. J. Lett.* 778:L3
- Burlaga LF, Ness NF, Stone EC. 2013b. *Science* 341:147
- Burrows RH, Zank GP, Webb GM, Burlaga LF, Ness NF. 2010. *Ap. J.* 715:1109
- Bzowski M, Kubiak MA, Möbius E, et al. 2012. *Ap. J. Suppl.* 198:12
- Chalov SV, Alexashov DB, McComas D, et al. 2010. *Ap. J. Lett.* 716:L99
- Chalov SV, Fahr HJ. 2000. *Astron. Astrophys.* 360:381-90
- Clarke JT, Lallement R, Bertaux J-L, Quemerais E. 1995. *Ap. J.* 448:893
- Cox NLJ, Kerschbaum F, van Marie A-J, et al. 2012. *Astron. Astrophys.* 537:A35
- Dayeh MA, McComas DJ, Allegrini F, et al. 2012. *Ap. J.* 749:50
- Decker RB, Krimigis SM, Roelof EC, Hill ME. 2010. See le Roux et al. 2010, p. 51
- Decker RB, Krimigis SM, Roelof EC, Hill ME. 2012. *Nature* 489:124
- Decker RB, Krimigis SM, Roelof EC, Hill ME. 2015. *J. Phys. Conf. Ser.* 577:012006
- Decker RB, Krimigis SM, Roelof EC, et al. 2005. *Science* 309:2020
- Decker RB, Krimigis SM, Roelof EC, et al. 2008. *Nature* 454:67
- Decker RB, Roelof EC, Krimigis SM, Hill ME. 2006. See Heerikhuisen et al. 2006, p. 73
- Desai MI, Allegrini FA, Bzowski M, et al. 2014. *Ap. J.* 780:98
- Desai MI, Allegrini FA, Dayeh MA, et al. 2012. *Ap. J. Lett.* 749:L30
- Donohue DJ, Zank GP. 1993. *J. Geophys. Res.* 98:19005
- Drake JF, Opher M, Swisdak M, Chamoun JN. 2010. *Ap. J.* 709:963
- Drury LO, Völk JH. 1981. *Ap. J.* 248:344
- Fahr HJ, Grzedzielski S, Ratkiewicz R. 1988. *Ann. Geophys.* 6:337
- Fayock B. 2013. *Analysis of solar Lyman- α scattering in the heliosphere*. PhD Thesis, Univ. Alabama, Huntsville
- Fayock B, Zank GP, Heerikhuisen J. 2013. *Ap. J. Lett.* 775:L4
- Fisk LA, Gloeckler G. 2006. *Ap. J. Lett.* 640:L79
- Fisk LA, Gloeckler G. 2012. *Ap. J.* 744:127
- Fisk LA, Gloeckler G. 2013. *Ap. J.* 776:79
- Fisk LA, Gloeckler G. 2014. *Ap. J.* 789:41
- Florinski V, Decker RB, le Roux JA, Zank GP. 2009. *Geophys. Res. Lett.* 36:12101
- Florinski V, Pogorelov NV, Zank GP, Wood BE, Cox DP. 2004. *Ap. J.* 604:700
- Florinski V, Zank GP. 2003. *J. Geophys. Res.* 108:1438
- Florinski V, Zank GP, Heerikhuisen J, Hu Q, Khazanov I. 2010. *Ap. J.* 719:1097

- Florinski V, Zank GP, Pogorelov NV. 2005. *J. Geophys. Res.* 110:7104
- Frisch PC, Bzowski M, Livadiotis G, et al. 2013. *Science* 341:1080
- Funsten HO, Allegrini F, Bochsler P, et al. 2009a. *Space Sci. Rev.* 146:75
- Funsten HO, Allegrini F, Crew GB, et al. 2009b. *Science* 326:964
- Funsten HO, DeMajistre R, Frisch PC, et al. 2013. *Ap. J.* 776:30
- Fuselier SA, Allegrini F, Bzowski M, et al. 2012. *Ap. J.* 754:14
- Fuselier SA, Allegrini F, Funsten HO, et al. 2009a. *Science* 326:962
- Fuselier SA, Bochsler P, Chornay D, et al. 2009b. *Space Sci. Rev.* 146:117
- Gamayunov K, Zhang M, Rassoul H. 2010. *Ap. J.* 725:2251
- Gangopadhyay P, Izmodenov V, Gruntman M, Judge DL. 2002. *J. Geophys. Res.* 107:1387
- Gangopadhyay P, Izmodenov VV, Gruntman M, Judge DL. 2006. *Ap. J.* 637:786
- Gangopadhyay P, Izmodenov VV, Shemansky DE, Gruntman M, Judge DL. 2005. *Ap. J.* 628:514
- Gangopadhyay P, Judge DL. 1989. *Ap. J.* 336:999
- Gangopadhyay P, Ogawa HS, Judge DL. 1989. *Ap. J.* 336:1012
- Gayley KG, Zank GP, Pauls HL, Frisch PC, Welty DE. 1997. *Ap. J.* 487:259
- Gleeson LJ, Axford WI. 1968. *Ap. Space Sci.* 2:431
- Gloeckler G, Fisk LA. 2010. See le Roux 2010, p. 110
- Gloeckler G, Fisk LA. 2015. *J. Phys. Conf. Ser.* 577:012011
- Goodrich CC. 1985. *Washington DC Am. Geophys. Union Geophys. Monogr. Ser.* 35:153
- Grygorczuk J, Ratkiewicz R, Strumik M, Grzedzielski S. 2011. *Ap. J. Lett.* 727:L48
- Gurnett DA, Kurth WS. 2005. *Science* 309:2025
- Gurnett DA, Kurth WS. 2008. *Nature* 454:78
- Gurnett DA, Kurth WS, Allendorf SC, Poynter RL. 1993. *Science* 262:199
- Gurnett DA, Kurth WS, Burlaga LF, Ness NF. 2013. *Science* 2025:150
- Gutynska O, Safránková J, Nemecek Z, Richardson JD. 2010. *Ap. J. Lett.* 722:L228
- Hall DT. 1992. *Ultraviolet resonance line radiation and the structure of the heliosphere*. PhD Thesis, Ariz. Univ., Tucson
- Hall DT, Shemansky DE, Judge DL, Gangopadhyay P, Gruntman MA. 1993. *J. Geophys. Res.* 98:15185
- Heerikhuisen J, Florinski V, Zank GP. 2006. *J. Geophys. Res.* 111:6110
- Heerikhuisen J, Florinski V, Zank GP, Pogorelov NV, eds. 2006. *Physics of the Inner Heliosphere: Voyager Observations, Theory, and Future Prospects: 5th Annu. IGPP Int. Astrophys. Conf. AIP Conf. Ser.*, Vol. 858. Melville, NY: AIP
- Heerikhuisen J, Pogorelov NV. 2011. *Ap. J.* 738:29
- Heerikhuisen J, Pogorelov NV, Florinski V, Zank GP, le Roux JA. 2008. *Ap. J.* 682:679
- Heerikhuisen J, Pogorelov NV, Zank GP, Florinski V. 2007. *Ap. J. Lett.* 655:L53
- Heerikhuisen J, Pogorelov NV, Zank GP, et al. 2010. *Ap. J. Lett.* 708:L126
- Heerikhuisen J, Zirnstein EJ, Funsten HO, Pogorelov NV, Zank GP. 2014. *Ap. J.* 784:73
- Herbst K, Heber B, Kopp A, Sternal O, Steinhilber F. 2012. *Ap. J.* 761:17
- Holzer TE. 1972. *J. Geophys. Res.* 77:5407
- Holzer TE. 1989. *Annu. Rev. Astron. Astrophys.* 27:199
- Ip W-H, Axford WI. 1985. *Astron. Astrophys.* 149:7
- Isenberg PA. 1986. *J. Geophys. Res.* 91:9965
- Isenberg PA. 2014. *Ap. J.* 787:76
- Izmodenov V, Alexashov D, Myasnikov A. 2005. *Astron. Astrophys.* 437:L35
- Izmodenov VV, Alexashov DB. 2006. See Heerikhuisen et al. 2006, p. 14
- Izmodenov VV, Geiss J, Lallement R, et al. 1999. *J. Geophys. Res.* 104:4731
- Izmodenov VV, Malama YG, Ruderman MS, et al. 2009. *Space Sci. Rev.* 146:329
- Jokipii JR, Thomas B. 1981. *Ap. J.* 243:1115
- Katushkina OA, Izmodenov VV, Wood BE, McMullin DR. 2014. *Ap. J.* 789:80
- Krimigis SM, Decker RB, Hill ME, et al. 2003. *Nature* 426:45
- Krimigis SM, Decker RB, Roelof EC, et al. 2013. *Science* 341:144
- Krimigis SM, Mitchell DG, Roelof EC, Hsieh KC, McComas DJ. 2009. *Science* 326:971
- Krimigis SM, Roelof EC, Decker RB, Hill ME. 2011. *Nature* 474:359

- Kubiak MA, Bzowski M, Sokół JM, et al. 2014. *Ap. J. Suppl.* 213:29
- Lallement R, Bertaux J-L. 2014. *Astron. Astrophys.* 565:A41
- Lallement R, Bertaux J-L, Clarke JT. 1993. *Science* 260:1095
- Lallement R, Quémerais E, Bertaux JL, et al. 2005. *Science* 307:1447
- Lazarian A, Opher M. 2009. *Ap. J.* 703:8
- le Roux J, Zank GP, Coates AJ, Florinski V, eds. 2010. *Pickup Ions Throughout the Heliosphere and Beyond: Proc. 9th Annu. Int. Astrophys. Conf. AIP Conf. Ser.*, Vol. 1302. Melville, NY: AIP
- Lee MA, Ip W-H. 1987. *J. Geophys. Res.* 92:11041
- Lee MA, Kucharek H, Möbius E, et al. 2012. *Ap. J. Suppl.* 198:10
- Lembège B, Savoini P, Hellinger P, Trávníček PM. 2009. *J. Geophys. Res.* 114:3217
- Liewer PC, Karmesin SR, Brackbill JU. 1996. *J. Geophys. Res.* 101:17119
- Linde TJ, Gombosi TI, Roe PL, Powell KG, Dezeeuw DL. 1998. *J. Geophys. Res.* 103:1889
- Linsky JL, Wood BE. 1996. *Ap. J.* 463:254
- Liu K, Möbius E, Gary SP, Winske D. 2012. *J. Geophys. Res.* 117:10102
- Liu Y, Richardson JD, Belcher JW, Kasper JC. 2007. *Ap. J. Lett.* 659:L65
- Livadiotis G, McComas DJ. 2009. *J. Geophys. Res.* 114:11105
- Livadiotis G, McComas DJ. 2013. *Space Sci. Rev.* 175:183
- McComas DJ, Alexashov D, Bzowski M, et al. 2012a. *Science* 336:1291
- McComas D, Allegrini F, Bochsler P, et al. 2004. In *Physics of the Outer Heliosphere*, ed. V Florinski, NV Pogorelov, GP Zank. *AIP Conf. Ser.* 719:162. Melville, NY: AIP
- McComas DJ, Allegrini F, Bochsler P, et al. 2009a. *Science* 326:959
- McComas DJ, Allegrini F, Bochsler P, et al. 2009b. *Space Sci. Rev.* 146:11
- McComas DJ, Allegrini F, Bzowski M, et al. 2014a. *Ap. J. Suppl.* 213:20
- McComas DJ, Angold N, Elliott HA, et al. 2013. *Ap. J.* 779:2
- McComas DJ, Bzowski M, Frisch P, et al. 2010. *J. Geophys. Res.* 115:9113
- McComas DJ, Dayeh MA, Allegrini F, et al. 2012b. *Ap. J. Suppl.* 203:1
- McComas DJ, Funsten HO, Fuselier SA, et al. 2011. *Geophys. Res. Lett.* 38:18101
- McComas DJ, Lewis WS, Schwadron NA. 2014b. *Rev. Geophys.* 52:118
- McDonald FB, Stone EC, Cummings AC, et al. 2003. *Nature* 426:48
- Möbius E, Bochsler P, Bzowski M, et al. 2012. *Ap. J. Suppl.* 198:11
- Möbius E, Bzowski M, Chalov S, et al. 2004. *Astron. Astrophys.* 426:897
- Möbius E, Liu K, Funsten H, Gary SP, Winske D. 2013. *Ap. J.* 766:129
- Moskalenko IV, Strong AW, Ormes JF, Potgieter MS. 2002. *Ap. J.* 565:280
- Müller H-R, Florinski V, Heerikhuisen J, et al. 2008. *Astron. Astrophys.* 491:43
- Müller H-R, Zank GP, Lipatov AS. 2000. *J. Geophys. Res.* 105:27419
- Müller H-R, Zank GP, Wood BE. 2001. *Ap. J.* 551:495
- Ness NF, Wilcox JM. 1965. *Science* 148:1592
- Opher M. 2012. *Astron. Rev.* 7:68
- Opher M, Drake JF. 2013. *Ap. J. Lett.* 778:L26
- Opher M, Prested C, McComas DJ, Schwadron NA, Drake JF. 2013. *Ap. J. Lett.* 776:L32
- Opher M, Stone EC, Liewer PC. 2006. *Ap. J. Lett.* 640:L71
- Parker EN. 1961. *Ap. J.* 134:20
- Pauls HL, Zank GP. 1996. *J. Geophys. Res.* 101:17081
- Pauls HL, Zank GP. 1997. *J. Geophys. Res.* 102:19779
- Pauls HL, Zank GP, Williams LL. 1995. *J. Geophys. Res.* 100:21595
- Pogorelov NV, Borovikov SN, Zank GP, et al. 2012. *Ap. J. Lett.* 750:L4
- Pogorelov NV, Borovikov SN, Zank GP, Ogino T. 2009a. *Ap. J.* 696:1478
- Pogorelov NV, Heerikhuisen J, Mitchell JJ, Cairns IH, Zank GP. 2009b. *Ap. J. Lett.* 695:L31
- Pogorelov NV, Heerikhuisen J, Zank GP. 2008. *Ap. J. Lett.* 675:L41
- Pogorelov NV, Heerikhuisen J, Zank GP, Borovikov SN. 2009c. *Space Sci. Rev.* 143:31
- Pogorelov NV, Heerikhuisen J, Zank GP, et al. 2011. *Ap. J.* 742:104
- Pogorelov NV, Matsuda T. 1998. *J. Geophys. Res.* 103:237
- Pogorelov NV, Stone EC, Florinski V, Zank GP. 2007. *Ap. J.* 668:611

- Pogorelov NV, Suess ST, Borovikov SN, et al. 2013. *Ap. J.* 772:2
- Pogorelov NV, Zank GP, Ogino T. 2004. *Ap. J.* 614:1007
- Pogorelov NV, Zank GP, Ogino T. 2006. *Ap. J.* 644:1299
- Prested C, Schwadron N, Passuite J, et al. 2008. *J. Geophys. Res.* 113:6102
- Quémerais E, Bertaux J-L, Lallement R, Sandel BR, Izmodenov V. 2003. *J. Geophys. Res.* 108:8029
- Quémerais E, Lallement R, Sandel BR, Clarke JT. 2009. *Space Sci. Rev.* 143:151
- Ratkiewicz R, Barnes A, Molvik GA, et al. 1998. *Astron. Astrophys.* 335:363
- Ratkiewicz R, Ben-Jaffel L, Grygorczuk J. 2008. In *Numerical Modeling of Space Plasma Flows*, ed. NV Pogorelov, E Audit, GP Zank. *ASP Conf. Ser.* 385:189. San Francisco: ASP
- Reisenfeld DB, Allegrini F, Bzowski M, et al. 2012. *Ap. J.* 747:110
- Richardson JD. 2008. *Geophys. Res. Lett.* 35:23104
- Richardson JD. 2009. In *Sock Waves in Space and Astrophysical Environments: 18th Annu. Int. Astrophys. Conf.*, ed. X Ao, GZR Burrows. *AIP Conf. Ser.* 1183:147. Melville, NY: AIP
- Richardson JD. 2010. *Geophys. Res. Lett.* 37:12105
- Richardson JD, Burlaga LF, Decker RB, et al. 2013. *Ap. J. Lett.* 762:L14
- Richardson JD, Decker RB. 2014. *Ap. J.* 792:126
- Richardson JD, Kasper JC, Wang C, Belcher JW, Lazarus AJ. 2008. *Nature* 454:63
- Richardson JD, Liu Y, Wang C, et al. 2006. *Geophys. Res. Lett.* 33:23107
- Richardson JD, Stone EC, Kasper JC, Belcher JW, Decker RB. 2009. *Geophys. Res. Lett.* 36:10102
- Richardson JD, Wang C. 2012. *Ap. J. Lett.* 759:L19
- Roelof EC, Krimigis SM, Mitchell DG, et al. 2010. See le Roux et al. 2010, p. 133
- Saul L, Wurz D, Rodriguez J, et al. 2012. *Ap. J. Suppl.* 198:14
- Scherer K, Fichtner H. 2014. *Ap. J.* 782:25
- Scherer K, Fichtner H, Strauss RD, et al. 2011. *Ap. J.* 735:128
- Schwadron NA, Allegrini F, Bzowski M, et al. 2011. *Ap. J.* 731:56
- Schwadron NA, Bzowski M, Crew GB, et al. 2009. *Science* 326:966
- Schwadron NA, McComas DJ. 2013. *Ap. J. Lett.* 778:L33
- Stone EC, Cummings AC. 2012. *Proc. 32nd Int. Cosmic Ray Conf.* 12:29
- Stone EC, Cummings AC, McDonald FB, et al. 2005. *Science* 309:2017
- Stone EC, Cummings AC, McDonald FB, et al. 2008. *Nature* 454:71
- Stone EC, Cummings AC, McDonald FB, et al. 2013. *Science* 341:150
- Story TR, Zank GP. 1997. *J. Geophys. Res.* 102:17381
- Strauss RD, Potgieter MS, Ferreira SES, Fichtner H, Scherer K. 2013. *Ap. J. Lett.* 765:L18
- Strumik M, Ben-Jaffel L, Ratkiewicz R, Grygorczuk J. 2011. *Ap. J. Lett.* 741:L6
- Strumik M, Czechowski A, Grzedzielski S, Macek WM, Ratkiewicz R. 2013. *Ap. J. Lett.* 773:L23
- Swisdak M, Drake JF, Opher M. 2013. *Ap. J. Lett.* 774:L8
- Thomas GE, Krassa RF. 1971. *Astron. Astrophys.* 11:218
- Washimi H, Tanaka T. 1996. *Space Sci. Rev.* 78:85
- Washimi H, Tanaka T. 2001. *Adv. Space Res.* 27:509
- Washimi H, Webber W, Zank GP, et al. 2012. *Ap. J. Lett.* 757:L2
- Washimi H, Zank GP, Hu Q, Tanaka T, Munakata K. 2007. *Ap. J. Lett.* 670:L139
- Washimi H, Zank GP, Hu Q, Tanaka T, Munakata K. 2014. *Ap. J.* In press
- Washimi H, Zank GP, Hu Q, et al. 2011. *MNRAS* 416:1475
- Webber WR, Higbie PR. 2009. *J. Geophys. Res.* 114:2103
- Webber WR, McDonald FB. 2013. *Geophys. Res. Lett.* 40:1665
- Williams LL, Hall DT, Pauls HL, Zank GP. 1997. *Ap. J.* 476:366
- Williams LL, Zank GP. 1994. *J. Geophys. Res.* 99:19229
- Witte M. 2004. *Astron. Astrophys.* 426:835
- Wood BE, Izmodenov VV, Linsky JL, Alexashov D. 2007a. *Ap. J.* 659:1784
- Wood BE, Izmodenov VV, Linsky JL, Malama YG. 2007b. *Ap. J.* 657:609
- Wood BE, Linsky JL, Müller H-R, Zank GP. 2001. *Ap. J. Lett.* 547:L49
- Wood BE, Müller H-R, Zank GP. 2000. *Ap. J.* 542:493
- Wood BE, Müller H-R, Zank GP, Linsky JL. 2002. *Ap. J.* 574:412

- Wood BE, Müller H-R, Zank GP, Linsky JL, Redfield S. 2005a. *Ap. J. Lett.* 628:L143
- Wood BE, Redfield S, Linsky JL, Müller H-R, Zank GP. 2005b. *Ap. J. Suppl.* 159:118
- Wu FM, Gangopadhyay P, Ogawa HS, Judge DL. 1988. *Ap. J.* 331:1004
- Wu FM, Judge DL, Suzuki K, Carlson RW. 1981. *Ap. J.* 245:1145
- Wu P, Winske D, Gary SP, Schwadron NA, Lee MA. 2009. *J. Geophys. Res.: Space Phys.* 114(A8):A08103
- Zank GP. 1999a. *Space Sci. Rev.* 89:413
- Zank GP. 1999b. In *The Solar Wind Nine Conference*, ed. RL Mace. *AIP Conf. Ser.* 471:783. Melville, NY: AIP
- Zank GP, Heerikhuisen J, Pogorelov NV, Burrows R, McComas D. 2010. *Ap. J.* 708:1092
- Zank GP, Heerikhuisen J, Wood BE, et al. 2013. *Ap. J.* 763:20
- Zank GP, Hunana P, Mostafavi P, Goldstein ML. 2014. *Ap. J.* 797:87
- Zank GP, Müller H-R. 2003. *J. Geophys. Res.* 108:1240
- Zank GP, Müller H-R, Wood BE. 2001. *Phys. Plasmas* 8:2385
- Zank GP, Pauls HL, Cairns IH, Webb GM. 1996a. *J. Geophys. Res.* 101:457
- Zank GP, Pauls HL, Williams LL, Hall DT. 1996b. *J. Geophys. Res.* 101:21639
- Zank GP, Pogorelov NV, Heerikhuisen J, et al. 2009. *Space Sci. Rev.* 146:295
- Zank GP, Webb GM, Donohue DJ. 1993. *Ap. J.* 406:67
- Zirnstein EJ, Heerikhuisen J, Zank GP, et al. 2014. *Ap. J.* 783:129



Contents

Exploring the Universe <i>Maarten Schmidt</i>	1
Hypervelocity Stars <i>Warren R. Brown</i>	15
Physical Models of Galaxy Formation in a Cosmological Framework <i>Rachel S. Somerville and Romeel Davé</i>	51
Powerful Outflows and Feedback from Active Galactic Nuclei <i>Andrew King and Ken Pounds</i>	115
Visible/Infrared Imaging Spectroscopy and Energy-Resolving Detectors <i>Frank Eisenbauer and Walfried Raab</i>	155
The Nine Lives of Cosmic Rays in Galaxies <i>Isabelle A. Grenier, John H. Black, and Andrew W. Strong</i>	199
Ideas for Citizen Science in Astronomy <i>Philip J. Marshall, Chris J. Lintott, and Leigh N. Fletcher</i>	247
On the Cool Side: Modeling the Atmospheres of Brown Dwarfs and Giant Planets <i>M.S. Marley and T.D. Robinson</i>	279
Grid-Based Hydrodynamics in Astrophysical Fluid Flows <i>Romain Teyssier</i>	325
Revisiting the Unified Model of Active Galactic Nuclei <i>Hagai Netzer</i>	365
The Occurrence and Architecture of Exoplanetary Systems <i>Joshua N. Winn and Daniel C. Fabrycky</i>	409

Faltering Steps Into the Galaxy: The Boundary Regions of the Heliosphere <i>G.P. Zank</i>	449
Interstellar Dust Grain Alignment <i>B-G Andersson, A. Lazarian, and John E. Vaillancourt</i>	501
Observations of the Icy Universe <i>A.C. Adwin Boogert, Perry A. Gerakines, and Douglas C.B. Whittet</i>	541
Molecular Clouds in the Milky Way <i>Mark Heyer and T.M. Dame</i>	583
Near-Field Cosmology with Extremely Metal-Poor Stars <i>Anna Frebel and John E. Norris</i>	631

Indexes

Cumulative Index of Contributing Authors, Volumes 42–53	689
Cumulative Index of Article Titles, Volumes 42–53	692

Errata

An online log of corrections to *Annual Review of Astronomy and Astrophysics* articles may be found at <http://www.annualreviews.org/errata/astro>